Ionic Thermophoresis and Its Application in Living Cells

Maren Reichl

Dissertation

München, 2014

Ionic Thermophoresis and Its Application in Living Cells

Maren Reichl

Dissertation
zur Erlangung des Grades
Doktor der Naturwissenschaft (Dr. rer. nat.)

an der Fakultät für Physik
der Ludwig-Maximilians-Universität
München

vorgelegt von
Maren Reichl
aus Stuttgart

München, den 10. Juni 2014

Erstgutachter: Prof. Dr. Dieter Braun
Zweitgutachter: Prof. Dr. Hermann Gaub
Eingereicht am: 10. Juni 2014
Mündliche Prüfung am: 28. Juli 2014

Zusammenfassung

Obwohl Thermophorese, das heißt die gerichtete Bewegung von Molekülen in einem Temperaturgradienten, schon vor mehr als 150 Jahren entdeckt wurde, ist ihre molekulare Ursache noch nicht restlos geklärt. Nichtsdestotrotz wird das Prinzip Thermophorese bereits in biomolekularen Bindungsmessungen eingesetzt. Beide Themengebiete sind spannend und wert, wissenschaftlich behandelt zu werden. In dieser Arbeit werden Experimente präsentiert, die einen großen Parameterraum abdecken. Durch diese Messungen konnte eine Kombination von Theorien zur molekularen Ursache überprüft und bestätigt werden. Damit lautet das erste Ergebnis dieser Arbeit, dass sich das Phänomen Thermophorese aus verschiedenen, additiven Beiträgen zusammensetzt. Einige davon können der ionischen Natur der Moleküle zugeordnet werden und sind wirkungslos bei elektrisch neutralen Molekülen. Der mikroskopische Mechanismus dieser ionischen Thermophoresebeiträge wird im ersten Teil behandelt. Dabei werden Arbeiten über das Kondensatormodell weitergeführt und ein zusätzlicher Beitrag diskutiert, den wir in Analogie zur Festkörperphysik Seebeck-Effekt nennen. Durch die verschiedenen Beiträge ist es gelungen, Theorien zu vereinen, die einerseits von einem lokalen, thermischen Gleichgewicht ausgehen, oder andererseits ein Nicht-Gleichgewichts-Phänomen beschreiben. Das physikalische Verständnis der Thermophorese auf molekularer Basis kommt auch ihrer Anwendung zugute. In der Pharmazie werden "Rasterfahndungen" durchgeführt, in denen die Bindungsaffinität einer ganzen Molekülbibliothek an ein Zielmolekül gemessen wird, um so die besten Kandidaten für einen neuen Wirkstoff heraus zu filtern. Diese profitieren, wenn Thermophorese vorhergesagt und zum Beispiel der Einfluss des Puffers bestimmt werden kann. Bindungskurven von Biomolekülen können heute schon in Zelllysat gemessen werden. Im zweiten Teil der Arbeit werden zum ersten Mal Thermophoresemessungen in lebenden Zellen vorgestellt. Dies bereitet den Weg für Bindungsmessungen *in vivo*. Um Thermophoresemessungen kompatibel zu Zellkulturen zu gestalten, wurde der Aufbau in entscheidenden Teilen angepasst, unter Benutzung von interner Totalreflexionsfluoreszenzmikroskopie (TIRF).

Abstract

Although thermophoresis, i.e. the directed movement of molecules in a temperature gradient, was discovered more than 150 years ago, its molecular origin is not jet fully understood. Nonetheless thermophoresis is used as a principle in biomolecular binding measurements. Both topics are interesting and worth a scientific discussion. In this thesis, systematic experiments over a large parameter space were conducted. From these measurements a combination of different theories about its molecular origin could be verified. Thus, the first result of this thesis is that the phenomenon thermophoresis consists of different additive contributions. Some of them relate to the ionic nature of the molecule and are non-existent when the molecule is electrically neutral. The microscopic mechanism of these ionic contributions to thermophoresis is discussed in the first part. It continues the work on the capacitor model and explains a further contribution, which we call Seebeck effect in analogy to solid state physics. Through the different contributions we bridge the gap between local thermodynamic equilibrium approaches and non-equilibrium theories. Several applications will greatly benefit from understanding the molecular physics of thermophoresis. Pharmacological screens are conducted to determine the binding affinity of a whole molecular library to a target molecule and thus to identify the best candidates for a new drug. These screens will be improved when thermophoresis can be predicted and for example the influence of the buffer can be determined. Binding measurements of biomolecules can already be conducted in cell lysate. The second part of this thesis will show thermophoresis measurements inside living cells for the first time. This paves the way for *in vivo* binding measurements inside cells. To make thermophoresis measurements compatible to cell culture, the setup was changed in great parts, now using total internal reflection fluorescence (TIRF) microscopy.

Contents

1 Motivation **1**

I Ionic Thermophoresis **3**

2 Theoretical Foundation **4**

3 Ideal Gas Contribution **5**

4 Capacitor Model **5**
4.1 Spherical Capacitor 5
4.2 Divalent Ions 8
4.3 Expansion of Water 8
4.4 Charge Condensation 10

5 Non-Spherical Geometry **11**
5.1 Theory 11
5.2 Low Salt Limit 13
5.3 High Salt Limit 13
5.4 Experiments 15

6 Seebeck Effect **17**
6.1 Calculation of the Seebeck Effect 17
6.2 Verification of the Seebeck Effect 19
6.3 Influence on the Capacitor Model 20
6.4 Container Walls 21

7 Non-Ionic Contribution **24**

8 Concentration Dependence **26**
8.1 Simulations 26
8.2 TRIS Buffer 27
8.3 Concentration Measurements 28
8.4 PEG Crowding Agent 29

9 Materials and Methods **32**
9.1 Setup 32
9.2 Probes 32
9.3 Analysis 33

10 Conclusion **35**

II Thermophoresis Inside Living Cells **36**

11 Introduction **37**

12 Materials and Methods **38**
12.1 Setup . . . 38
12.2 Chamber . . . 38
12.3 Optics . . . 38
12.4 Bead Measurements . . . 39
12.5 Temperature Profile . . . 39
12.6 DNA Measurements . . . 40
12.7 Cell Culture . . . 40
12.8 Cell Transfection and Measurements . . . 40

13 Finite Element Calculations **42**
13.1 Temperature Field Model . . . 42
13.2 Bead Thermophoresis Model . . . 42
13.3 DNA Thermophoresis Model . . . 42
13.4 Intracellular Thermophoresis Model . . . 44

14 Setup Verification **46**
14.1 Chromium Layer . . . 46
14.2 Bead Measurements . . . 46
14.3 DNA Measurements . . . 50

15 Cell Experiments **52**
15.1 Cell Measurements . . . 52
15.2 Repeated Heating . . . 55
15.3 Intracellular Thermophoresis . . . 55
15.4 Size Dependence . . . 56

16 Conclusion **59**

III Appendix **60**

17 Abbreviations **61**
17.1 Mathematical Symbols . . . 61

17.2 Abbreviations 63

18 References **64**

19 Publications **70**

1 Motivation

Most molecules are too small to be moved with mechanical, optical, or magnetic tweezers [1]. Besides chemical linking to surfaces, only two methods are known to move molecules in a fluid: electrophoresis and thermophoresis. Electrophoresis has been known since 1937 [2] with a sound theoretically foundation. Thermophoresis is less widely known and the underlying mechanism is poorly understood. It was discovered more than 150 years ago [3, 4] for salt solutions, which had a higher concentration in the cold part of a tubing than in the hot part. Later, thermophoresis was discovered for colloidal systems, but already for an aqueous setting different theories are still discussed.

Up to now, thermophoresis could be measured, but could not yet be predicted quantitatively. A variety of methods to measure thermophoresis have been explored. In a parallel plate geometry, measurements are save from convection, but can take hours [5, 6]. Experiments in a micron sized setup are much faster. Here two gold lines, 25 µm apart, are alternatingly heated, and a concentration gradient establishes [7]. A concentration gradient corresponds to a gradient of refractive index, in which a laser beam is deflected and measured. Such a beam deflection method often requires sample concentrations on the order of weight percent, which is hard to achieve with biological probes [8–10]. The same applies for the thermal lensing method [11] and the thermal diffusion forced Rayleigh scattering [12, 13]. With the thermal lensing method a partly absorbed beam locally heats the fluid and drives thermophoresis. The expansion of water and the concentration gradient act as lenses, and the transmitted part of the beam is analyzed for this lensing effect. With the thermal diffusion forced Rayleigh scattering method, a temperature grid is established by absorbing an interference pattern with a molecule. This grid scatters a beam. In a confocal microscope geometry short distances and fast measurements are achieved [14]. There, 3D concentration information can be obtained, as the detection volume is restricted by a pinhole. With a fluorescent label, small molecule concentrations down to picomolar concentrations can be measured [15]. Braun and coworkers have shown that the thermal gradient for thermophoresis can be applied optically by absorption of an infrared (IR) laser in a column of water within the thin sheet of solution [16, 17]. Matching the speed of axial thermophoresis was used to probe strong thermal gradients [14].

The strength of thermophoresis depends on the buffer, molecule size, shape, electric charge, and hydration. Systematic experiments over a large parameter space are required to evaluate the different theories – as presented in this thesis.

Although thermophoresis could not be predicted yet, it is used as a principle in biomolecular binding measurements. To understand the complexity of biology, measurements of biomolecular reactions are increasingly transferred from the test tube into living cells. Recent success in the life science industry (Nanotemper Technologies) demonstrate the demand of such methods in the life science community. They commercialized thermophoresis measurements for biomolecular studies to measure binding affinities. This represents the step from measurements with surface fixation, like surface plasmon resonance measurements (SPR) [18] or enzyme-linked immunosorbent assay (ELISA) [19], to measurements in free solution and in the molecules native environment, e.g. cell lysate.

Thermophoresis among other parameters is sensitive to the molecule's size, charge, and conformation. Size will influence the mass diffusion. Charge will be discussed in the first part of this thesis and the conformation influences the hydrophobicity and thus the non-ionic part of the Soret coefficient. At least, one of these properties will change in a binding event, thus the binding event can be detected. In a measurement, however, care must be applied not to change the buffer, since this will also influence thermophoresis. Thus, thermophoresis measurements can be used to measure binding affinities of DNA [20], proteins [21], pharmaceutical components [22], and even membrane receptors [23]. Recently, protein binding at the picomolar level was reported [15]. Not only binding to large partners can be detected, but also the binding of, for example, the small ion Ca^{2+}[21]. Thermophoresis became the basis for 140 publications in leading biology journals, including tubulin binding to transport proteins [24] and binding studies of avian influenza to cell surface receptors [25]. When the fluorescent amino acid tryptophan is present, additional labeling of the probe can be omitted [26]. In contrast to ELISA, thermophoresis measurements can be conducted without surface fixation and in the molecule's natural environment, such as blood serum [27] or cell lysate [28].

The next step is transferring these measurements into living cells. The first steps to achieve this are shown in the second part of this thesis. The measurement chamber needs to be adapted, since large adherent eucaryotic cells are difficult to grow in very small capillaries. Additionally, it will be favorable to measure more cells simultaneously to obtain good statistics, so the measurement with heating at a single spot by an IR laser is changed as well. Since we change the core of thermophoresis measurements, the new setup needs to be verified and first single thermophoresis measurements are performed. In the future this will enable the combination of multiple thermophoresis measurements into binding measurements.

Part I

Ionic Thermophoresis

2 Theoretical Foundation

This chapter will pursue a theory introduced by Dhont [29] and Herzog [30] and and it will introduce additional terms. As to start with some basic definitions, the thermophoretic velocity $\vec{v}_T$ of a particle in a temperature gradient ∇T is described by the thermo-diffusion coefficient D_T:

$$\vec{v}_T = -D_T \cdot \nabla T \tag{1}$$

So a movement toward the cold is defined with a positive thermo-diffusion coefficient. Often we will find this direction, but thermophilic molecules and conditions also exist. Thermophoretic movement will lead to an accumulation or depletion (concentration c) in cold and warm spots (concentration gradient ∇c) and trigger mass diffusion (diffusion coefficient D). The particle flux $\vec{j}$ then is

$$\vec{j} = -\nabla c \cdot D - c \cdot D_T \cdot \nabla T \tag{2}$$

In a stable temperature distribution T eventually the steady state is reached, in which diffusion and thermodiffusion exactly counterbalance each other and the particle flux vanishes. If connected to a reservoir with concentration c_0 and temperature T_0 the concentration distribution can be calculated by

$$c(T) = c_0 \cdot \exp\left[-\frac{D_T}{D} \cdot (T - T_0)\right] \tag{3}$$

The ratio $D_T/D \equiv S_T$ is called Soret coefficient. The first part of this thesis will give a molecular explanation on the phenomenon of ionic thermophoresis. We propose that the Soret coefficient is composed of different, additive parts which we call the capacitor model S_T^{CM}, the Seebeck effect S_T^{SE}, a non-ionic contribution S_T^{NI} and an ideal gas contribution $1/T$:

$$S_T = S_T^{CM} + S_T^{SE} + S_T^{NI} + 1/T \tag{4}$$

To test the model thoroughly with all contributions mentioned in Eq. 4 implies measuring the Soret coefficient in a broad, multidimensional parameter space. DNA was chosen as a model system because of its excellent purity, the possibility of a fluorescent label, and generally well-known molecular parameters of DNA. Due to the fluorescent label, very small concentrations can be measured. For the non-ionic contribution the temperature is varied, and for the capacitor model the salt concentration is varied. Therefore, the single stranded DNA length was chosen to be oligomeric (2 to 80 bases), so its hydrodynamic radius is comparable to the Debye length. The range of Debye lengths was limited, since for short lengths the DNA started to stick to the capillary walls (borosilicate glass) and long Debye lengths conflicted with the ion input from the buffer. For the Seebeck effect, DNA was measured in many different, mostly monovalent salt electrolytes.

3 Ideal Gas Contribution

Even an ideal gas shows thermophoresis if it is exposed to a temperature gradient. If one side of the gas is hotter than the other side, then the gas molecules on the hot side have a higher mean velocity compared to those on the cold side. Thus, the probability to change sides is larger for a fast moving, hot particle than for a cold and slow molecule. This results in a net particle flow from the hot to the cold part. These considerations can be also applied to fluids, although many more additional factors play a role. The contribution stemming from the explicit temperature dependence of the diffusion coefficient is called ideal gas contribution in Eq. 4. It is the one also occurring in an ideal gas, as is explained above. The full theoretical derivation of it can be found in [29].

4 Capacitor Model

4.1 Spherical Capacitor

Moving from the ideal gas to thermophoresis in an aqueous surrounding, there will be more contributions to the Soret coefficient (Eq. 4). In an electrolyte any charged particle will be screened by counter charges on a screening length called Debye-Hückel length. This can be viewed as a spherical capacitor (see Fig. 1).

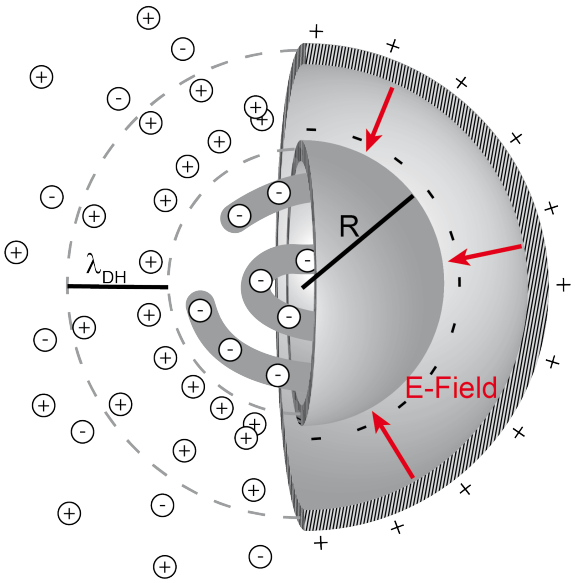

Figure 1: The screening of the charge of a spherical particle by counter ions in solution can be seen as a capacitor. The particle with radius R is the inner sphere, the counter ions represent the outer sphere. The two spheres are spaced by the Debye-Hückel screening length λ_{DH}. The local electric field in this capacitor can be used to calculate thermophoresis. Image courtesy of Herzog [30], electric field added.

As described in [29, 30] the capacitor model contribution to the Soret coefficient S_T^{CM} can be derived from the electric energy W stored in this spherical capacitor

$$S_T^{CM} = \frac{1}{kT}\frac{\partial W}{\partial T} \tag{5}$$

where

$$W = \frac{Q^2}{8\pi\varepsilon R(R/\lambda_{DH}+1)} \tag{6}$$

with the Boltzmann constant k, the absolute temperature T, the permittivity of water $\varepsilon(T) = \varepsilon_r(T) + \varepsilon_0$ with the relative permittivity $\varepsilon_r(T)$ and the vacuum permittivity ε_0, and the hydrodynamic radius of the sample R. In the case of DNA in an aqueous salt solution the charge $Q = Z_{eff} \cdot e$ (with the effective charge number Z_{eff} and the elementary charge e) is independent of the temperature. The Debye-Hückel screening length λ_{DH} resembles the distance of the plates in the spherical capacitor. It is also called Debye length for short or screening length. Herzog found the radius R of our model system DNA to be independent of temperature[30], but Lipfert found a small temperature dependence [31]. Next to the explicit temperature dependence of the Debye length, the permittivity of water depends on the temperature [32]. Later on we will also need to model a temperature dependence of the concentration c_i of all (salt) ion species i with charge number z_i present in the fluid. The Debye length and its temperature derivation are

$$\lambda_{DH}(T) = \sqrt{\frac{\varepsilon kT}{N_A e^2 \sum_i c_i z_i^2}} \tag{7}$$

$$\frac{\partial \lambda_{DH}}{\partial T} = \frac{\lambda_{DH}}{2}\left(\frac{1}{T} + \frac{1}{\varepsilon}\frac{\partial \varepsilon}{\partial T} - \frac{1}{\sum_i c_i z_i^2}\frac{\partial \sum_i c_i z_i^2}{\partial T}\right) \tag{8}$$

with the Avogadro constant N_A. The Debye length increases with decreasing salt concentration and decreases with temperature. With this information the Soret coefficient can be calculated as

$$\begin{aligned} S_T^{CM} &= \frac{Q^2}{kT^2 16\pi\varepsilon\lambda_{DH}(R/\lambda_{DH}+1)^2}\left[1 - \left(1 + \frac{2\lambda_{DH}}{R}\right)\frac{T}{\varepsilon}\frac{\partial \varepsilon}{\partial T} - \frac{T}{\sum_i c_i z_i^2}\frac{\partial \sum_i c_i z_i^2}{\partial T}\right] \\ &= \frac{Q^2}{kT^2 16\pi\varepsilon\lambda_{DH}(R/\lambda_{DH}+1)^2}\left[1 - \left(1 + \frac{2\lambda_{DH}}{R}\right)\frac{\partial \ln \varepsilon}{\partial \ln T} - \frac{\partial \ln \sum_i c_i z_i^2}{\partial \ln T}\right] \end{aligned} \tag{9}$$

This equation can be verified by measuring different sized single stranded DNA in salt solutions of various concentrations. As explained by Herzog [30] two limiting cases can be examined for $\lambda_{DH} \ll R$ and $\lambda_{DH} \gg R$. In the first case the screening length is small enough so the bending becomes negligible

and the system behaves like a parallel plate capacitor with S_T^{CM} linearly depending on the λ_{DH}, as was experimentally verified by Duhr et al. [17, 33]. In the latter case the model resembles a point charge and S_T^{CM}over λ_{DH} is a plateau (see dashed lines in Fig. 3). As shown in this thesis, the other contributions of Eq. 4 do not depend on the salt concentration. Thus, the capacitor model can be verified if the size of the particles and the titrated Debye length are approximately the same size. By measuring S_T over λ_{DH} the capacitor model can be compared to Eq. 9 with an additional offset from the other contributions.

We thus verified the capacitor model by measuring the Soret coefficient of single stranded DNA in KCl solutions of various concentrations. We used DNA as a model system due to its well known properties, high purity, high charge, and availability in many sizes. The solution was filled into a rectangular glass capillary with only 50 µm height in order to suppress convection. The temperature of the capillary and the solution was controlled, and a spot in the aqueous solution was heated with an infra-red (IR) laser. A camera recorded the diffusion through a fluorescence microscope. For details about the setup and the measurements see section 9.

The measurements are shown in Fig. 2. Eq. 9 was fitted to our data with two fee parameters: the offset from the other contributions, and the effective charge number Z_{eff} of the molecule. However, these are no real fitting parameters, because the values of Z_{eff} reflect the known effective charge of DNA in electrophoresis (see section 4.4) and the offset could be explained from the other Soret contributions. As seen in Fig. 2, the data of the 80mer deviates for large λ_{DH}, marking the breakdown of the internal shielding approximation.

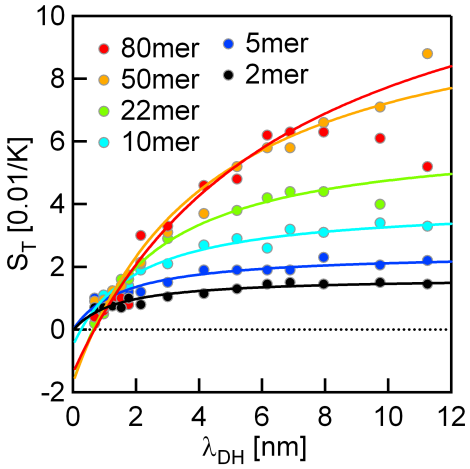

Figure 2: Thermophoresis measurements (dots) of different single stranded DNA lengths (colors) plotted across the Debye length λ_{DH}. The theoretical predictions are shown as solid lines.

By rescaling Eq. 9 with the effective charge number of the particle and its size, S_T^{CM} only depends on the rescaled Debye length λ_{DH}/R and all data should fall onto this master curve (Eq. 10):

$$S_T^{CM} \cdot \frac{R}{Z_{eff}^2} = \frac{e^2 \cdot (R/\lambda_{DH})}{kT^2 16\pi\varepsilon(R/\lambda_{DH}+1)^2} \left[1 - \left(1 + \frac{2\lambda_{DH}}{R}\right) \frac{\partial \ln \varepsilon}{\partial \ln T} - \frac{\partial \sum_i c_i z_i^2}{\partial \ln T}\right] \tag{10}$$

The data of Fig. 2 was replotted in this way in Fig. 3.

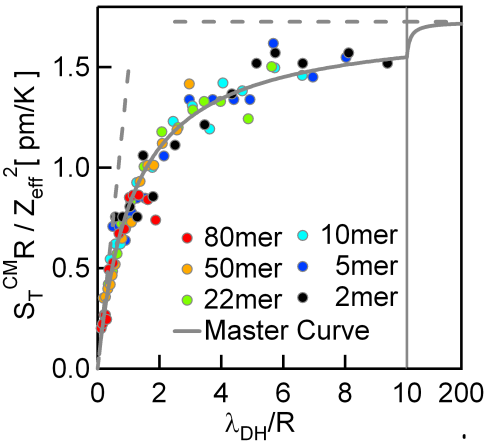

Figure 3: The data of Fig. 2 was rescaled to fall onto one single master curve.

4.2 Divalent Ions

The capacitor model still holds for divalent ions (see. Fig. 4). Here the conversion from salt concentration to Debye length is different, according to Eq. 7. Thus, we could only measure up to about $\lambda_{DH} =$ 8 nm, before the buffer concentration affected the measurements. Also, the effective charge of the DNA dropped to about 0.2 e per base and was only about half of the amount compared to the same DNA in a monovalent electrolyte. This can be readily explained by the work of Lipfert [34], according to which divalent ions screen the DNA charge much better than monovalent ions. Or it can be explained by the work of O'Brien [35], where a decrease in the electric mobility is shown for higher-valent salts. There a factor of 1/2 is mentioned for the electric mobility of divalent salts, which can be adopted, since the electric mobility is directly proportional to the effective charge.

4.3 Expansion of Water

In addition to Eq. 9 one could include the thermal expansion of water. By heating, the sample concentration c is diluted [32] by

$$\frac{\partial \rho(T)}{\partial T} \Delta T$$

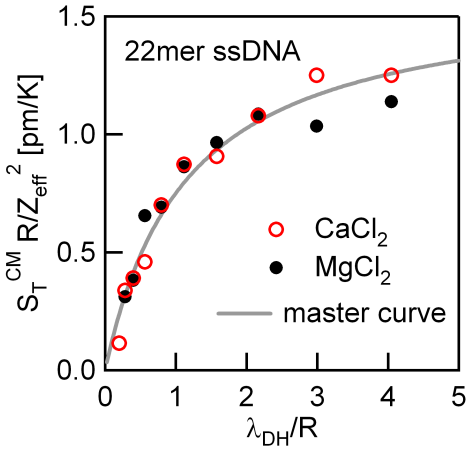

Figure 4: The capacitor model holds for electrolytes with divalent ions, but the effective charge of the DNA is reduced to about $0.2e$ as compared to the DNA in monovalent electrolytes with about $0.4e$.

with the density of water $\rho(T)$. This factor was already included in the work of Herzog [30]. The last term of Eq. 9,

$$\frac{\partial \ln \sum_i c_i z_i^2}{\partial \ln T}$$

can thus be rewritten in terms of ρ.

$$S_T^{CM} = \frac{Q^2}{kT^2 16\pi\varepsilon\lambda_{DH}(R/\lambda_{DH}+1)^2}\left[1-\left(1+\frac{2\lambda_{DH}}{R}\right)\frac{\partial \ln \varepsilon}{\partial \ln T}-\frac{\partial \ln \rho}{\partial \ln T}\right] \tag{11}$$

In our case the temperature expansion of water can be omitted, since its influence on S_T^{CM} in our temperature range (5 - 75 °C) is small. The influence is largest with 8.3% at $\lambda_{DH} = 0$ (infinitely high salt concentration) and 75 °C with $\partial \ln \rho / \partial \ln T = -0.21$ and $\partial \ln \varepsilon / \partial \ln T = -1.6$ (see Fig. 5).

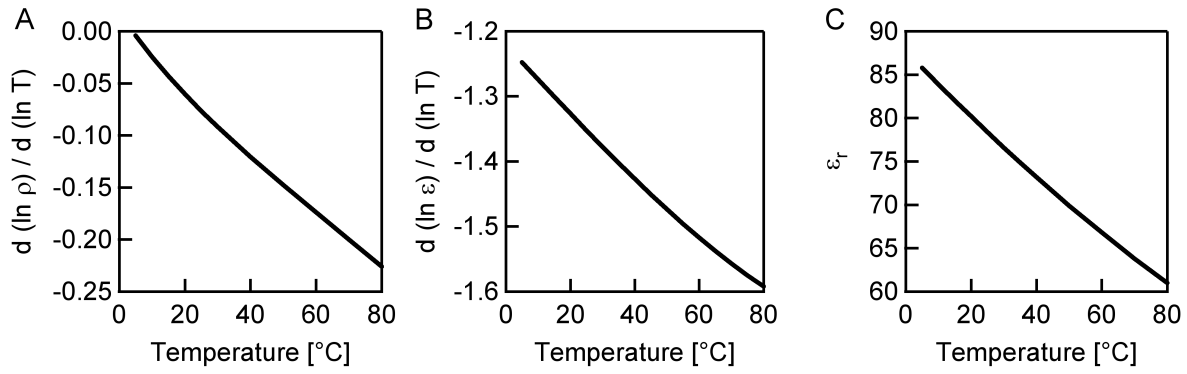

Figure 5: (A) Water expansion with temperature (B, C) Dielectric constant of water with temperature [32]

4.4 Charge Condensation

The amplitude of the Soret coefficient of the capacitor model measured over the Debye length scales with the square of the effective charge (see Eq. 9). Thus, the effective charge can be fitted from those measurements. In section 4.1 the effective charge was a fitting parameter, but actually it is known already from electrophoresis as

$$Z_{eff} = \frac{\mu \cdot k \cdot T}{e \cdot D} \tag{12}$$

with the electric mobility μ. In a multi-particle collision dynamics simulation the concept of the Manning condensation was implemented [36]. There charges condense onto the DNA or RNA if the electric potential is large enough, and an effective charge per base or a charge per base pair can be calculated. The charge per base or per base pair (in units of the negative elementary charge e) decreases with increasing length of the DNA. Interestingly, the values for the charge per base and per base pair, depending on whether the DNA is single or double stranded, are almost identical. The reason for this is that the spacing of the charges is very similar. This supports the hypothesis that this effective charge can be used in the capacitor model. Herzog also measured only little difference when he calculated the effective charge (also in units of the negative elementary charge e) from his Soret measurements. I extended his measurements on both sides for the short 2mer and a long 80mer single stranded DNA (see. Fig. 6). Our measurements confirm the simulations mentioned above [36] when the two negative charges of the fluorescent label are added with similar spacing as in the DNA [30]. The pKa value of the fluorescent 6-Hex label is ~3 [37], so within the pH range of our experiments (5–9) it is always charged. With these charges values for the charge per base higher than one can be achieved.

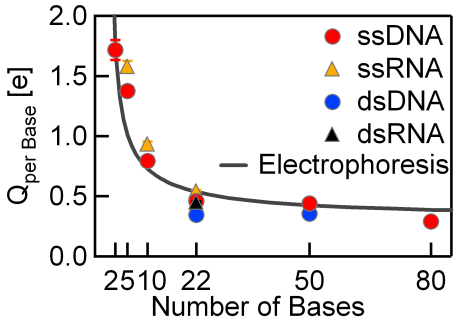

Figure 6: Charge per base in units of e (here negative) as yielded by the capacitor model. Data and image of Herzog [30] with the 2mer and 80mer ssDNA added.

5 Non-Spherical Geometry

Short single stranded DNA of various sizes and Debye lengths is used as a model system to test the spherical capacitor model experimentally (section 4). The main contribution is explained with a spherical capacitor model. Interestingly, double and single stranded oligomers show very similar thermophoresis, although the persistence length of double stranded DNA (dsDNA) and RNA (dsRNA) is much longer than the sequences used by Herzog [30]. Although the persistence length of single stranded DNA is 10 Å to 32 Å, i.e. 2 to 7 bases short [31], and a spherical form of the molecule is likely, the shape of double stranded oligomers might be better modeled as a rod, since their persistence length is about 170 base pairs [38]. Here we will explain in more detail, why such a spherical capacitor nevertheless can be used as a good approximation. Previously, the effect of molecule geometry in thermophoresis was studied for solid virus particles, with a contour length of 880 nm, a radius of 3.4 nm, and a persistence length of 2.2 µm assuming a constant surface charge density and using modified Bessel functions to describe the geometry [39]. Such an approach does not fit measurements for short DNA or RNA, since in this approximation the particle is a long, thin cylinder and end effects are assumed to be negligible. Alternatively an approximation of the shape as a string of spheres was proposed.

In this chapter, we follow a direct analytical method with a full geometrical description, valid for all Debye lengths. We insert a cylindrical condensator into the previously studied spherical capacitor. As usual with shielding capacitors we assume that the condensators are acting in parallel. A cylinder capped with hemispheroids was also used in modeling of electrophoresis [40]. There it was found that for a length-to-diameter ratio greater than about 3, the end caps of the cylinder have a negligible effect, provided the length is chosen to yield a structure with the same volume. So, having proven with the Manning theory and in experiments that single and double stranded oligomers have the same charge (section 4.4), we will prove here that also differences in geometry are negligible. We find that single and double stranded oligomers behave surprisingly similar.

Here, we will adapt the spherical capacitor model, which was first proposed by Dhont (3), to elongated rods. The shape is modeled as a sphere, which is cut in halves, with an inserted cylinder of the same radius R (compare Fig. 1 and Fig. 7). Thus, also the end effects can be included in the model.

5.1 Theory

For comparison we will calculate all three models: the sphere, the cylinder without end caps, and the combined structure, which we call rod. The rod capacitor (capacitance C_{rod}) is composed of two parallel capacitors: a spherical capacitor (C_{sphere}) and a cylindrical capacitor ($C_{cylinder}$ with the overall length L reduced by $2R$, i.e. the length of the end caps):

$$\begin{aligned} C_{sphere} &= 4\pi\varepsilon R(R/\lambda_{DH}+1) \\ C_{cylinder} &= \frac{2\pi\varepsilon L}{\ln(\lambda_{DH}/R+1)} \\ C_{rod} &= C_{sphere}+C_{cylinder} \end{aligned} \tag{13}$$

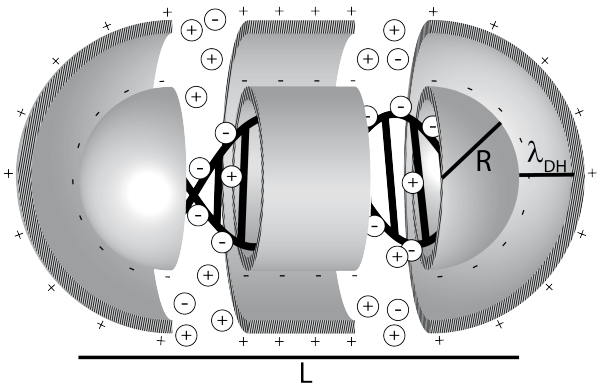

Figure 7: Molecular model to explain the Debye length dependence of thermophoresis. The spherical capacitor model can be extended to rod shaped molecules such as short double stranded DNA. The shape is modeled as a sphere, which is cut in halves with an inserted cylinder. The radius of the sphere and the cylinder is R, the overall length is L. The charge of the elongated particle is screened by counter ions in solution within the Debye length λ_{DH}. The combined capacitor is treated as a spherical and a cylindrical capacitor in parallel. Image style according to Herzog [30].

with R the radius of the sphere and of the cylinder, and L the overall length, see Fig. 7. The energy stored in a capacitor is $W = Q^2/(2C)$, cf. Eq. 6, with $Q = Z_{eff}\,e$ being the effective charge of the particle and Z_{eff} the effective charge number in multiples of the elementary charge:

$$\begin{aligned} W_{sphere} &= \frac{Q^2}{8\pi\varepsilon R\,(R/\lambda_{DH}+1)} \\ W_{cylinder} &= \frac{Q^2 \ln(\lambda_{DH}/R+1)}{4\pi\varepsilon L} \\ W_{rod} &= \frac{Q^2}{4\pi\varepsilon\left[2R\,(R/\lambda_{DH}+1)+(L-2R)/\ln\left(\lambda_{DH}/R+1\right)\right]} \end{aligned} \tag{14}$$

Analogously to the Soret coefficient of a sphere $S_{T\,sphere}$ (Eq. 9) and the Soret coefficient of the cylinder $S_{T\,cylinder}$ can be calculated as the temperature derivative of the electric energy (Eq. 5):

$$\begin{aligned} S_T &= \frac{1}{kT}\frac{\partial W}{\partial T} \\ S_{T\,sphere} &= \frac{Q^2}{kT^2 16\pi\varepsilon\lambda_{DH}\left(R/\lambda_{DH}+1\right)^2}\left[1-\frac{\partial \ln\varepsilon}{\partial \ln T}\left(1+\frac{2\lambda_{DH}}{R}\right)\right] \\ S_{T\,cylinder} &= \frac{Q^2}{kT^2 4\pi\varepsilon L}\cdot\left[\frac{\lambda_{DH}\left(1+\frac{\partial \ln\varepsilon}{\partial \ln T}\right)}{2R\left(\frac{\lambda_{DH}}{R}+1\right)}-\ln\left(\frac{\lambda_{DH}}{R}+1\right)\cdot\frac{\partial \ln\varepsilon}{\partial \ln T}\right] \end{aligned} \tag{15}$$

The Soret coefficient of the rod $S_{T\,rod}$ is

$$S_{T\,rod} = \frac{Q^2}{kT^2 4\pi\varepsilon \left[2R(\frac{R}{\lambda_{DH}}+1)+(L-2R)/\ln(\frac{\lambda_{DH}}{R}+1)\right]^2}$$
$$\times \left\{ \frac{R^2}{\lambda} + \frac{(L-2R)\frac{\lambda_{DH}}{R}}{2\ln^2(\frac{\lambda_{DH}}{R}+1)\cdot(\frac{\lambda_{DH}}{R}+1)} + \frac{\partial \ln \varepsilon}{\partial \ln T}\left[\frac{(L-2R)\frac{\lambda_{DH}}{R}}{2\ln^2(\frac{\lambda_{DH}}{R}+1)\cdot(\frac{\lambda_{DH}}{R}+1)} - \frac{R^2}{\lambda_{DH}} - 2R - \frac{L-2R}{\ln(\frac{\lambda_{DH}}{R}+1)} \right] \right\} \quad (16)$$

In case the length of the rod is exactly the diameter of the sphere ($L = 2R$), i.e. no cylinder is inserted, the equation for the rod equals the spherical equation. The three equations are calculated in Fig. 8a resembling a 22mer. Single stranded DNA with no secondary structure is a random coil roughly in the shape of a sphere since the persistence length is about 2 to 7 bases [31]. The hydrodynamic radius of the sphere depends on the DNA length, i.e. 2 nm and 3.7 nm for a 22mer and a 50mer, respectively. However, the radius of the rod or the cylinder is that of the DNA strand: 1 nm and the length of double stranded DNA is $L = \textit{base pairs} \cdot 0.34\,\text{nm/base pair}$, i.e. 7.5 nm and 17 nm for the 22mer and the 50mer, respectively.

5.2 Low Salt Limit

For the limit of high Debye lengths or low salt concentrations, the change in geometry from a spherical to a rod structure should not affect the Soret coefficient. In the case of an infinite Debye length, a particle can be considered a point charge, regardless of its shape. Formally, $S_{T\,cylinder}$ goes towards infinity for low salt concentrations. However, for the rod the end effects become much more important: The surface of the outer sphere (i.e. of the end caps) grows with λ_{DH}^2, whereas the surface of the outer cylinder only grows with λ_{DH}:

$$\lim_{\lambda_{DH}/R\to\infty} S_{T\,sphere} = \lim_{\lambda_{DH}/R\to\infty} S_{T\,rod} = \frac{-Q^2 \frac{\partial \ln \varepsilon}{\partial \ln T}}{kT^2 8\pi\varepsilon R} \quad (17)$$

So the Soret coefficient becomes constant for very large λ_{DH}, but for the rod this value is approached very slowly as can be seen in Fig. 8). For the rod the final value, equal to a sphere with the same radius, is approached only for Debye lengths far too long to be achievable for real electrolytes. Thus, the Soret coefficient of an elongated particle is considerably lower than the Soret coefficient of a sphere with same diameter and charge. It is about as large as the Soret coefficient of a particle with the same surface.

5.3 High Salt Limit

For the limit of high salt concentrations, i.e. small Debye lengths, the capacitance changes with surface area similar to a plate capacitor, since the area of the two plates hardly differs. The Soret coefficient of a plate capacitor is linear in Debye length. Here, the spherical part and the cylindrical parts are separated, because the shielding of both parts does not overlap for such small screening lengths. The area for a spherical and a rod like molecule of the same radius will differ, and thus the slope of the Soret coefficient will differ. However, the capacitor part of the Soret coefficient will in both cases vanish for the limit of

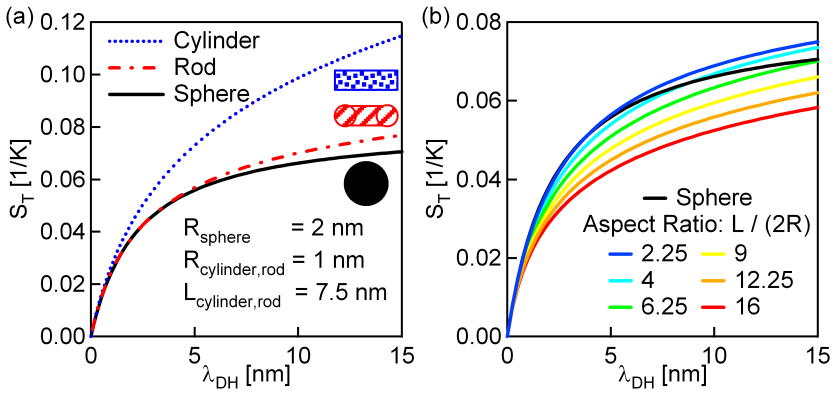

Figure 8: Calculation of the cylinder, rod and sphere models for a 22mer DNA. (a) The single strand is modeled as a sphere with radius $R = 2$ nm and the double strand is modelled as a cylinder and a rod with $R = 1$ nm and length $L = 7.5$ nm. Between rod and sphere there are only small differences. (b) In comparison to the sphere of (a), we plot rods with different aspect ratios $L/(2R)$, but with the same surface area as the sphere. For experimentally accessible Debye lengths, the rods behave similarly to the sphere up to about an aspect ratio of 9. A 22mer and a 50mer dsDNA have aspect ratios of 3.75 and 8.5, respectively. The Soret coefficients were calculated at temperature $T = 25$ °C with an effective charge of $Q = -10e$.

very high salt concentrations. The surface of the two capping half spheres at the end of the rod (together $4R^2\pi$) is exactly as large as the surface of the additional cylinder, if the cylinder was extended all the way to the end ($2\pi RL$ with $L = 2R$). Thus, for the limit of high salt concentration the Soret coefficient of the rod is equal to the Soret coefficient of a cylinder without end effects.

$$\begin{aligned}
\lim_{\lambda_{DH}\to 0} S_{T\,sphere} &= \frac{Q^2}{16\pi kT^2\varepsilon R^2}\left(1-\frac{\partial \ln \varepsilon}{\partial \ln T}\right)\lambda_{DH} \\
\lim_{\lambda_{DH}\to 0} S_{T\,cylinder} &= \frac{Q^2}{8\pi kT^2\varepsilon LR}\left(1-\frac{\partial \ln \varepsilon}{\partial \ln T}\right)\lambda_{DH} = \frac{2R}{L}\cdot\lim_{\lambda_{DH}\to 0} S_{T\,sphere} \\
\lim_{\lambda_{DH}\to 0} S_{T\,rod} &= \frac{Q^2}{8\pi kT^2\varepsilon LR}\left(1-\frac{\partial \ln \varepsilon}{\partial \ln T}\right)\lambda_{DH} = \lim_{\lambda_{DH}\to 0} S_{T\,cylinder}
\end{aligned} \tag{18}$$

This agrees with the approximations by Wang et al. [39]. They calculated and compared the Soret coefficient of a particle with constant surface charge. We, in contrast, calculate and compare the Soret coefficient for a particle with constant charge. In our experiments we know the effective charge of the molecule, given by a constant charge per length. In addition, this charge is approximately the same for single and double stranded DNA, as discussed further in section 4.4. If a constant surface charge is maintained, then the charge Q scales with the aspect ratio $L/(2R)$. Since the Soret coefficient is proportional to the square of the charge Q, our equation matches the one of Wang [39] for the limit of high salt concentrations.

The sphere in Fig. 8b again models a 22mer ssDNA. Additionally rods of different aspect ratios but with the same surface areas are shown. The aspect ratios for the 22mer and the 50mer are 3.75 and 8.5,

respectively. Deviations from the spherical model kick in for dsDNA longer than about 50 bases, i.e. an aspect ratio L /(2R) = 9. For comparison, the persistence length of dsDNA is at about 170 bases [38]. Considering this, the theoretical Soret coefficients are similar for single and double stranded oligomers in the range of experimentally accessible Debye lengths. The effects of the elongated shape and the smaller radius approximately cancel each other.

5.4 Experiments

Since the theoretical curves are alike, measurements of double stranded DNA can be fitted equally well with a spherical and a rod like model (Fig. 9). As free fitting parameters we choose the effective charge number and a molecule specific offset, which includes other contributions to the Soret effect from Eq. 4. Both the spherical and the rod model yield very similar effective charge numbers as fitting parameter (Table 1). Since the charge of a particle enters Eq. 16 quadratically, one could expect a factor 4 difference between single stranded and double stranded DNA and RNA. However, their Soret coefficients are quite similar (see Fig. 9) with a similar effective charge. According to the Manning theory [36] and electrophoresis measurements [41] single stranded and double stranded oligomers have approximately the same effective charge and electric mobility. As we discuss and see here, this similarity also translates to thermophoresis.

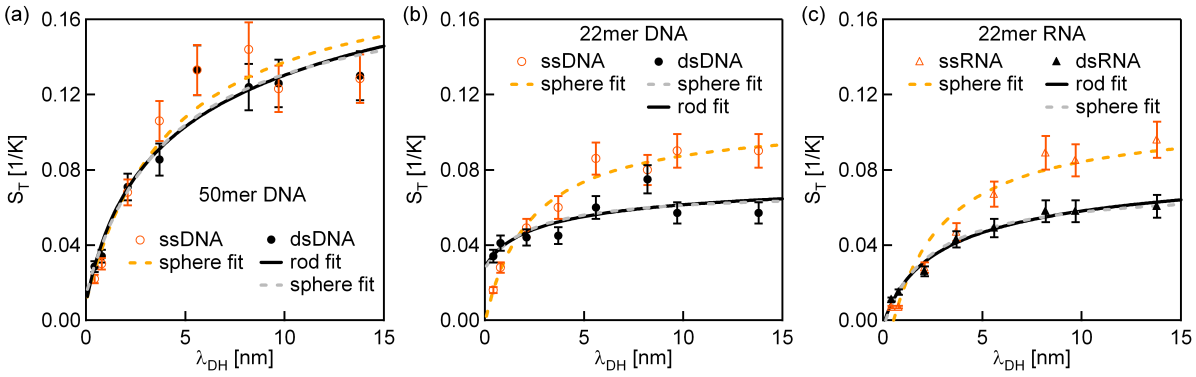

Figure 9: The thermophoresis of double stranded DNA and RNA can be fitted as a rod with radius $R = 1$ nm and a length of $L = 7.5$ nm and 17 nm for 22mer and 50mer, respectively. Single stranded oligonucleotides can be seen as spheres with a hydrodynamic radius of 2 nm and 3.7 nm for the 22mer and the 50mer, respectively. However, the respectively other model geometry can be similarly fitted to the thermophoresis measurements. The sphere and the rod fit and yield very similar effective charges Z_{eff} for the double stranded measurement data (see Table 1). The Debye length was titrated using KCl including the 1 mM TRIS buffer at pH 7.8. The measurements were conducted at 25 °C. Data courtesy of Herzog [30].

We have shown that single and double stranded DNA of the same length behave surprisingly similar in a temperature gradient. We derived an analytical capacitor model for elongated rods with arbitrary Debye lengths. The cylindrical capacitor without end caps diverges for large Debye lengths, but the

Table 1: Parameters for the different fitting models in Fig. 9. We fitted Z_{eff} and assumed the radius to be $R = 2.0$ nm and $R = 3.7$ nm based on PEG-free measurements of the diffusion coefficient. Temperature was 25 °C, relative permittivity of water $\varepsilon_r = 78$ and its temperature derivative $\partial \ln \varepsilon / \partial \ln T = -1.35$. There was a free offset parameter to account for other contributions to the Soret coefficient.

Fig. 9	Z_{eff}
50mer ssDNA sphere	20.3 ± 1.3
50mer dsDNA sphere	19.5 ± 1.0
50mer dsDNA rod	18.6 ± 1.0
22mer ssDNA sphere	11.6 ± 0.4
22mer dsDNA sphere	7.1 ± 1.0
22mer dsDNA rod	6.9 ± 1.0
22mer ssRNA sphere	12.9 ± 0.6
22mer dsRNA sphere	9.7 ± 0.3
22mer dsRNA rod	9.3 ± 0.3

spherical and the rod shaped capacitor behave alike for all possible Debye lengths – theoretically and in the experiments.

6 Seebeck Effect

Not only the probe particles, in our case the DNA, will move in a temperature gradient due to thermophoresis, but also the salt ions in the electrolyte. This was how thermophoresis was discovered in the first place [3, 4]. The different ion species can have different Soret coefficients, which are known from thermo-electric measurements and can be seen in Table 2. The cations and anions will accumulate at the hot and cold sides to different extents, as visualized in Fig. 10. This charge separation will result in an electric field, in which charged probe particles, like the DNA in our case, and all other ions will exhibit common electrophoresis. This effect is macroscopically indistinguishable from thermophoresis and thus discussed here. It is called Seebeck effect in analogy to the thermo-voltages in solid state physics. Alternatively, a more descriptive name is thermo-electrophoresis. Since the pioneering salt species dependent Soret measurement of Putnam and Cahill [42] a contribution to thermophoresis from the Seebeck effect has been suspected, but not demonstrated without fitting parameters.

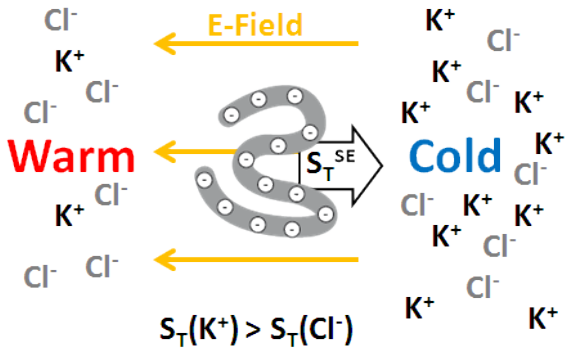

Figure 10: Differential thermophoresis of the salt ions themselves (here: potassium chloride) will lead to an electric field. In this, the charged particle (here: DNA) will experience electrophoresis. This is called the Seebeck effect and it is considered part of thermophoresis, since it it indistinguishable from it.

6.1 Calculation of the Seebeck Effect

To calculate the Seebeck effect we follow the argumentation of Guthrie and Würger [43, 44] who treated the case with monovalent salts. Eq. 2 on page 4 is expanded by electrophoresis (electric mobility μ and electric field $\vec{E}$) to

$$\vec{j} = -\nabla c \cdot D - c \cdot \nabla T \cdot D_T + c \cdot \mu \cdot \vec{E} \tag{19}$$

For the salt ions we use the approximation [41]

$$\mu_i = \frac{z_i \cdot e \cdot D_i}{k \cdot T} \tag{20}$$

with the charge number z_i of the i-th ion species, the elementary charge e, and the Boltzmann constant k. For the highly charged DNA this definition of the electric mobility can be used to define an effective

charge number Z_{eff}. Eq. 19 is valid for every ion species i, in solution. Thus, we can sum over all ion species i and after considering the neutrality condition

$$\sum_i z_i \nabla c_i = 0 \tag{21}$$

we can solve for the electric field

$$\vec{E} = \frac{k \cdot T \cdot \nabla T}{e} \cdot \frac{\sum_i z_i c_i S_{Ti}}{\sum_i z_i^2 c_i} \tag{22}$$

This electric field is proportional to the concentration weighted average of Soret coefficients of the ions present in solution, and thus the highly concentrated salts dominate the sums. In our experiments we used 1 µm DNA in several mM salt and TRIS buffer. So although the DNA is highly charged, its influence on $\vec{E}$ is only marginal because of its small concentration. The same argument holds for H_3O^+ and OH^-, although their Soret coefficients is higher than for the salts by a factor of ten to twenty (see Table 2). Their concentration is too small if the pH is at physiological values; e.g. at pH 7 the concentration of H_3O^+ and OH^- ions is 0.1 µM.

Table 2: Soret coefficients and electrophoretic mobilities of different ion species. Values of the hydrodynamic radius R, mass diffusion coefficient D, electric mobility μ, and Soret coefficient S_T were used to calculate the Seebeck effect in Fig. 11 and Fig. 12. The Soret coefficients S_T were taken from [45] and [46]. The values of ion conductivities were taken from [32] and converted to mobilities μ. The diffusion coefficients D from [32] were converted to a hydrodynamic radius using the Einstein-Stokes relation [47].

Ion	D [µm²/s]	R [Å]	μ [m²/Vs]	S_T [1/K]
Ca_2^+	792	2.76	6.16E-8	1.33E-2
K^+	1957	1.12	7.62E-8	3.51E-3
Li^+	1029	2.12	4.01E-8	7.18E-4
Mg^{2+}	706	3.09	5.49E-8	1.22E-2
Na^+	1334	1.64	5.19E-8	4.69E-3
Ni^{2+}	661	3.30	5.14E-8	1.26E-2
Br^-	2080	1.05	8.09E-8	8.13E-4
Cl^-	2032	1.07	7.91E-8	7.18E-4
F^-	1475	1.48	5.74E-8	5.32E-3
I^-	2045	1.07	7.96E-8	-2.10E-3
OH^-	5273	0.414	2.05E-7	2.33E-2
H_3O^+	9311	0.234	3.62E-7	1.80E-2

The charge of the DNA is stable between pH 5 and 9, and in this range the Soret coefficient does not change significantly [30]. At extreme pH values these ions will have an effect [10] so we always included a small amount of TRIS buffer. Due to the temperature dependence of the TRIS dissociation constant pKa, the pH changes with a rate of -0.03 1/K. The pKa value of the fluorescent 6-Hex label is ~3 [37], so

within the pH range of our experiments it is always charged. The kinetics of pH equilibration are known to be much faster than the diffusive kinetics of thermophoresis.

By inserting the calculated electric field (Eq. 22) into Eq. 19 we get the Soret coefficient and the contribution of the Seebeck effect as

$$S_T^{SE} = -\frac{k \cdot T \cdot \mu_{DNA}}{e \cdot D_{DNA}} \cdot \frac{\sum_i z_i c_i S_{Ti}}{\sum_i z_i^2 c_i} \tag{23}$$

6.2 Verification of the Seebeck Effect

The question is how the Seebeck effect can be verified experimentally and distinguished from the other contributions? If we use a monovalent salt as the electrolyte, the concentration dependence cancels in Eq. 23, since there is an equal amount of anions an cations. As long as the electrolyte composition is not changed, all c_i are reduced to the constant stochiometric ratio, and the ionic strength (or Debye length) can be varied without varying the Seebeck effect. Thus, we have a salt concentration independent, but salt species dependent factor. If we measure S_T in various salt concentrations and various salt species, we can fit the capacitor model to the data for each species with an offset coming from the other contributions in Eq. 4. This data and the capacitor model fits are shown in Fig. 11. We extrapolate the capacitor model fits to the limit of zero Debye length and thus S_T^{CM} vanishes, since for small Debye lengths S_T^{CM} is proportional to the Debye length (Eq. 9). We know the temperature and can subtract the ideal gas contribution from this offset. The remaining non-ionic part does not depend on the salt species (see section 7). Thus, it can be separated as a constant by varying the salt species. The theory from Eq. 23 with the values from Table 2 can then be compared to the experimental results of the Seebeck contribution, i.e. to the Soret coefficient as shown in Fig. 12. Here the electric mobility was a fitting parameter and we found $\mu_{DNA} = -1.2 \pm 0.13$, -2.6 ± 0.24, and $-1.2 \pm 0.13 \cdot 10^{-8}$m²/Vs for the 2mer, 22mer, and 80mer, respectively.

Next to the DNA measurements we also measured the positively charged fluorescent dye Rhodamine 6G in the different salt species. Since it has only one positive charge, the amplitude of the capacitor model measured over the Debye length is small. Furthermore, the molecule is very small compared to the DNA, and thus the transition region from the plate capacitor regime ($\lambda_{DH} \ll R$) to the point charge regime ($\lambda_{DH} \gg R$) is at very high salt concentrations. Since Rhodamine 6G is prone to sticking to the capillary walls especially at high salt concentrations, we coated the walls with the positively charged poly-L-lysine before the measurement and kept the salt concentration at 10 mM. In Fig. 12 the measurements with lithium salts seem to deviate from the theoretical expectations. Lithium is the smallest of the positively charged ions and is suspected to interact with DNA [49], possibly perturbing hydrogen bonds [50]. Also Lipfert et al. measured that lithium screens the macromolecule's charge better than the larger potassium or sodium [34]. This results in a different effective charge of the DNA in lithium electrolytes, which was not considered in the theory.

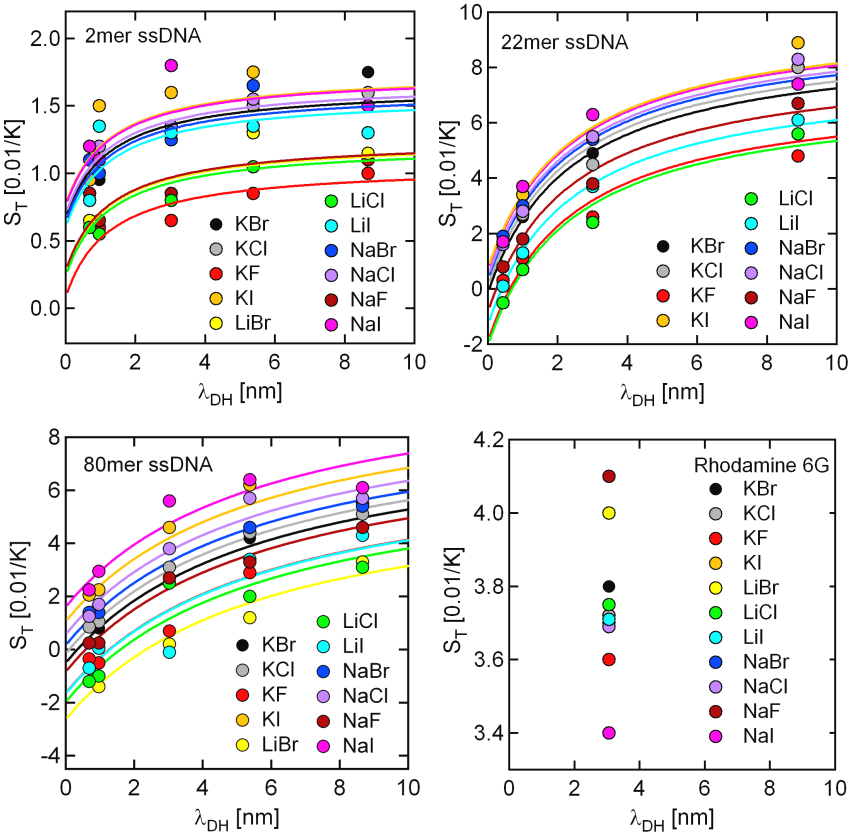

Figure 11: Soret coefficient of DNA with different lengths in the first three panels. For the Rhodamine 6G no dependence over the Debye length was measured, and thus S_T^{CM} cannot be subtracted. All measurements were done in different salt concentrations (x-axis) of different salt species (colors). For each salt species we fitted the capacitor model to the data and extrapolated it to $\lambda_{DH} = 0$, so we could separate the Seebeck effect from this offset. Most data for 22mer from Götz [48].

6.3 Influence on the Capacitor Model

The contribution of the capacitor model to thermophoresis as described in section 4.1 depends on the salt concentration. We just derived that the salt concentration also depends on the temperature field. The last term in Eq. 9 on page 6 already considers a temperature dependent distribution of the salt ions in the electrolyte around a particle. This is given by the Soret coefficient S_{Ti} of the i-th ion species.

$$\frac{\partial c_i}{\partial T} = -S_{Ti} \cdot c_i \tag{24}$$

With this Eq. 9 becomes

$$S_T^{CM} = \frac{Q^2}{kT^2 16\pi\varepsilon\lambda_{DH}(R/\lambda_{DH}+1)^2}\left[1-\left(1+\frac{2\lambda_{DH}}{R}\right)\frac{T}{\varepsilon}\frac{\partial\varepsilon}{\partial T}+\frac{T\sum_i S_{Ti}c_i z_i^2}{\sum_i c_i z_i^2}\right] \tag{25}$$

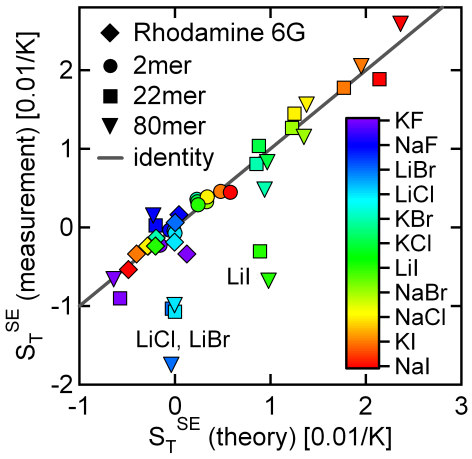

Figure 12: If all other contributions are subtracted from the Soret coefficient ($S_T^{SE} = S_T - S_T^{NI} - 1/T - S_T^{CM}$), the Seebeck contribution is obtained and can be compared to the theoretical value from Eq. 23 with the molecule's parameter and the values of Table 2.

The difference between this effect and the Seebeck effect is that the capacitor model always depends on the charge squared, and with the Seebeck effect also the sign of the charge can be tested. Here and in Eq. 25 the valency of the ions is squared both times. In the case of only one monovalent salt in the electrolyte we have as many cations as anions and Eq. 25 can be further simplified to

$$S_T^{CM} = \frac{Q^2}{kT^2 16\pi\varepsilon\lambda_{DH}(R/\lambda_{DH}+1)^2}\left[1-\left(1+\frac{2\lambda_{DH}}{R}\right)\frac{T}{\varepsilon}\frac{\partial\varepsilon}{\partial T}+T\cdot<S_T>\right] \tag{26}$$

with $< S_T >$ the average Soret coefficient of the anion and cation. This changes the Soret coefficient, as can be seen in Fig. 13. To evaluate the relevance of this deviation we can compare the figure directly to the measurements in Fig. 3 on page 8. There also for a homogeneous salt concentration the theoretical curve is shown, which is identical to the one in Fig. 13 Here, for the limit of low salt concentration, no change is detected. For the limit of high salt concentration we get a different slope, but the master curve still vanishes. The temperature dependence of this contribution is small, as $\frac{\partial \ln\varepsilon}{\partial \ln T}$ decreases with increasing temperature. At 15 °C and with potassium chloride at $S_T(\mathrm{K}^+) = 3.63\cdot10^{-3}$ 1/K, $S_T(\mathrm{Cl}^-) = 7.43\cdot 10^{-4}$ 1/K, $\partial\ln\varepsilon/\partial\ln T = -1.3$, $\lambda_{DH}/R = 1$ this contribution is 12.1% and at 75 °C with $\partial\ln\varepsilon/\partial\ln T = -1.58$ it is 12.4% of S_T^{CM} (see Fig. 5 on page 9).

6.4 Container Walls

To evaluate whether the glass container walls influence the electric field we implemented a 1D FEMLAB simulation. We compared a linear temperature gradient, which presses the salt ions against the chamber walls, with an artificial temperature gradient of the same strength, which peaks in the free fluid center. The chamber size was 10 µm and the electrolyte consisted only of 10 µM KCl. The boundary conditions were set as following: In the upper graphs in Fig. 14 the potential and ion concentrations were fixed in

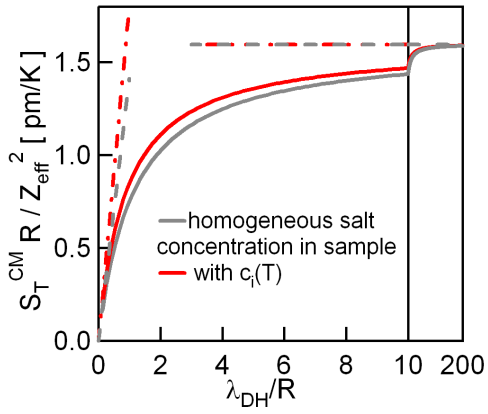

Figure 13: The Soret coefficient of the salt ions will change the salt concentration, and thus the Debye length, in a temperature dependent way. This influences the master curve.

the center of the chamber to 0 V and bulk concentrations, and the boundaries were put to insulation and symmetry. In the lower graphs we applied continuity in the center and at the boundaries the potential was fixed to zero, and the ion concentrations were fixed to bulk concentrations. By setting the chamber walls to a fixed potential, we imitate the changed potential due to the OH^- groups of the glass surface.

As shown on the left sides of Fig. 14, the temperature gradient was $\nabla T = 10^6$ K/m with the sign depending on the sign of the temperature gradient. The analytical solution (right side, red lines) for the electric field according to Eq. 22 with the Soret coefficients of the ions of Table 2 on page 18 would be E =36.1 V/m (sign depending on the sign of the temperature gradient) and the Debye length according to Eq. 7 λ_{DH} =0.137 µm. The result of this simulation is that the electric field can not change faster than on the scale of the Debye length. The potential of the wall will be screened, which is not accounted for in the analytical equation. However, an electric field can build up to the same extent also in the free solution.

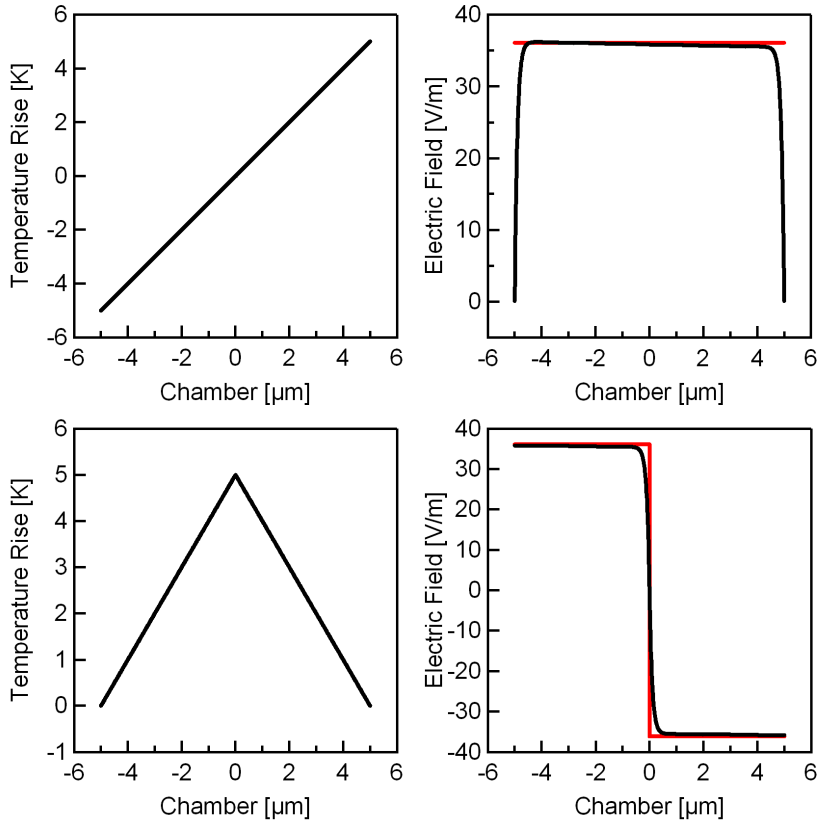

Figure 14: Analytical solution (red) and finite element simulations (black) of the Seebeck field of KCl (right side) in a given temperature field (left side). In the upper panels the glass walls at -5 µm and 5 µm distort the electric field, in the lower panels there are no glass walls and the salt ions accumulate in the free fluid at 0 µm. The electric field cannot change faster than at the scale of the Debye length.

7 Non-Ionic Contribution

While the capacitor model only gives positive S_T^{CM}, the Soret coefficient from the Seebeck effect S_T^{SE} can have both positive and negative signs. Herzog found negative Soret coefficients mainly for low base temperatures and high salt concentrations [30]. So we need a temperature dependent effect and use the empiric equation for DNA and other charged particles [11]

$$S_T^{NI} = S_T^{\infty} \cdot \left[1 - \exp\left(\frac{T^* - T}{T_0}\right)\right] \tag{27}$$

which can nicely be fitted to our experimental data (Fig. 15). Besides the temperature T there are the fitting parameters S_T^{∞}, T^* and T_0 in Eq. 27. For Fig. 15 Herzog's data was revised by subtracting the Seebeck contribution (cf. section 6) and refitting.

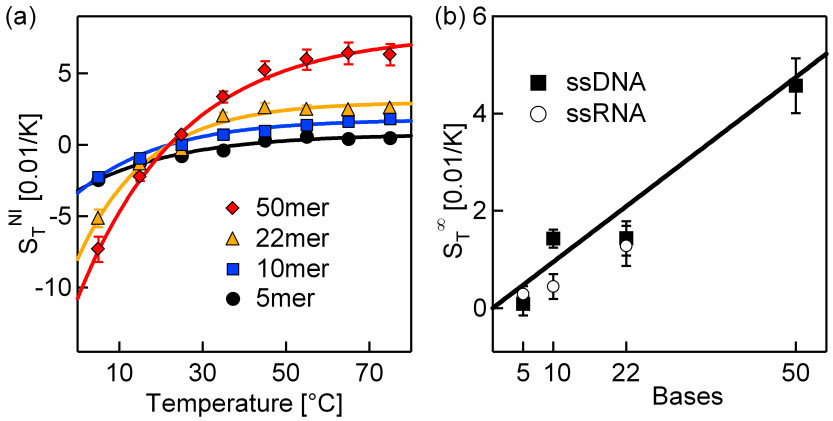

Figure 15: (a) Non-ionic contribution to the Soret coefficient is temperature dependent. Data and image from Herzog [30] modulated by subtracting S_T^{SE} and refitting. (b) S_T^{∞} is the amplitude of the non-ionic contribution and scales with the number of bases (one strand counted). This indicates that the non-ionic contribution could stem from a short ranged molecule-water interaction located in a thin tube around and along the molecule.

The magnitude of the change in Soret coefficient S_T^{∞} scales with the DNA length (see Fig. 15b). The reason for this is that S_T^{NI} is attributed to the molecule-water interaction. This is a short-range interaction and thus also takes place inside the random coil of DNA all along its length, rather than interacting with the whole particle at once. We suspect that the basis of Eq. 27 is the energy in the hydration layer. Hydrogen bonds typically show a pronounced temperature dependence. A future starting point for a molecular understanding of this equation might be the joint density functional theory, developed in the chair of Tomas Arias [51], who calculated exactly the energy of the hydration shell around an ion. When studying uncharged molecules Eq. 27 might not apply and the temperature dependence might be different. Wienken showed that the binding of a single calcium ion can be detected with thermophoresis measurements [21]. Here the confirmation of the molecule changed, also changing the hydration energy.

Otherwise, if no specific binding is present, the non-ionic contribution to the Soret coefficient does not depend on the salt concentration and in Fig. 12 we kept S_T^{NI} constant per molecule.

The next question is whether we can attribute all temperature dependence of the Soret coefficient to S_T^{NI}. Assuming a constant heat of transport Q_i^* [45] the Soret coefficients of the salt ions varies with $S_{Ti} = Q_i^*/kT^2$. Thus, S_T^{SE} also depends on the temperature. We measured the temperature dependence of 22mer ssDNA in different salt solutions LiBr, KI, KF, KCl (see Fig. 16). The measurements over salt concentrations were extrapolated to $\lambda_{DH} = 0$ to subtract S_T^{CM}.

In Fig. 12 we measured S_T^{SE} at 25°C as -0.0070, 0.211, -0.0057, and 0.0137 1/K for LiBr, KI, KF, and KCl, respectively. These values were subtracted as constants in Fig. 16 to bring the curves to approximately the same height. The remaining temperature increase does not depend on the salt species and is identical for all salts. This means that either there is no temperature dependence of S_T^{SE}, or it is common to all salts.

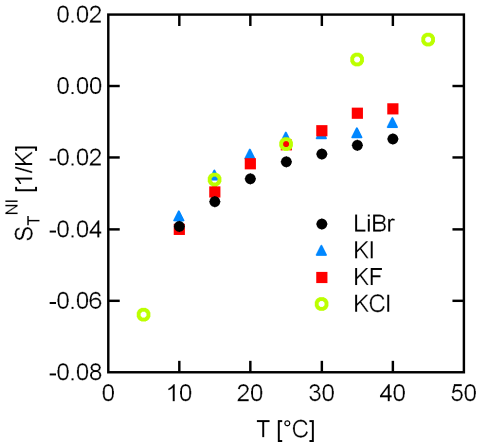

Figure 16: S_T^{NI} over temperature. We deducted S_T^{CM} from the Soret coefficient by extrapolating to $\lambda_{DH} = 0$ and subtracted a constant S_T^{SE}, which we measured in Fig. 12 as -0.0070, 0.211, -0.0057, and 0.0137 1/K for LiBr, KI, KF, and KCl, respectively, to bring them to the same height. The remaining temperature increase does not depend on the salt species. Thus, there is no temperature dependence of S_T^{SE}, besides the constant number, which we subtracted. The measurements in KCl buffer are from [30].

8 Concentration Dependence

8.1 Simulations

In our experiments we used a sample concentration of 1 µM. This is sufficient, since we use a fluorescence microscope for concentration measurements. Particle-particle interactions [8, 52, 53] are not expected to contribute at this concentration level, and thus they were not considered. Typically, non-fluorescent measurements of thermophoresis are performed in 100-1000 fold higher concentrations, where an empiric concentration correction has to be applied [7, 8]. Other methods use a beam deflection method, where the concentration is detected via the refractive index [8–10]. Further methods are thermal lensing [11] or the thermal diffusion forced Rayleigh scattering [12, 13]. These methods need up to a weight percent of concentration. Our concentration of 1 µm is also far below the overlap concentration, as defined as the concentration, where the macromolecules start to overlap due to their spacial extension. For the larges molecule in our experiments, the 80mer with a hydrodynamic radius of 6 nm, the overlap concentration is about 1mM.

Due to the low sample concentration we could neglect its influence on the Debye length and on the electric field. However, DNA is a poly-ion and will have some influence on the Debye length and on the electric field. To better understand this influence we implemented a 1D radial finite element method FEMLAB 3.1 (COMSOL AB). We used the Nernst-Planck chemical engineering module, but we substituted the first differential equation for the electric potential with a Poisson equation. In addition to mass diffusion and electrophoresis, which are provided as a FEMLAB module ready to use, thermo-diffusion was implemented for the salt cation and anion. The 80mer ssDNA was included as an ion with 1 µM concentration and with the charge number $Z_{eff} = -7$ as determined in our measurements. Corresponding to the charged DNA we included the counter ions by increasing the cation concentration to ensure overall charge neutrality. This poly-ion now contributed to the Debye length. The DNA also contributed to the electric field with its full Soret coefficient $S_T^{NI} + 1/T + S_T^{CM}$. We keep the DNA concentration constant in our experiments in order to have constant intensity by constant fluorophore concentration. This changed the composition of the electrolyte. The effect of the DNA is small in principle, but noticeable for low salt concentrations, i.e. larger Debye lengths, as can be seen in Fig. 17a. The simulation closely matched the analytical solution for S_T^{SE} (Eq. 23) of the different salt species.

There are other ions in the electrolyte, which we also need to consider: H_3O^+ and OH^-. Their concentrations depends on the pH and with their large Soret coefficients (see Table 2) they will contribute to the electric field. Their influence can be seen in Fig. 17b. When the pH is between 5 and 9, the charge of the DNA is constant [54], so we kept the pH in this region. Longer DNA has a higher Soret coefficient and higher charge and thus more influence on the Seebeck effect than short DNA, as can be seen in Fig. 17c.

To summarize, the contribution to the electric field of the H_3O^+ and OH^- ions and the probe particle itself are negligible, as long as their concentration is small compared to the salt, although they have a large Soret coefficient and are highly charged, respectively.

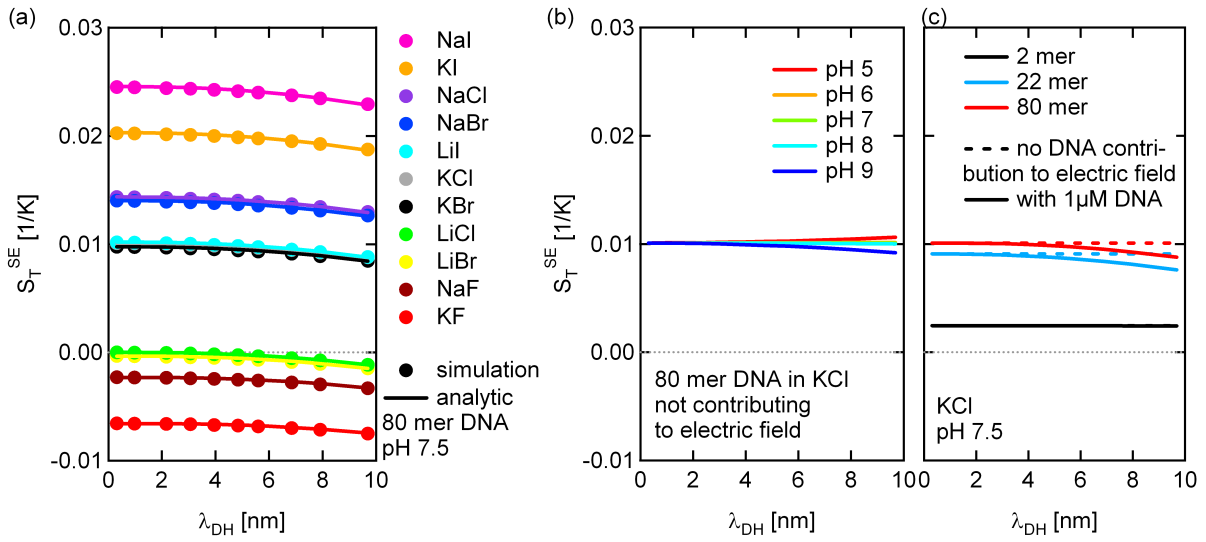

Figure 17: (a) In a finite element method simulation with FEMLAB we confirmed the analytical result of Eq. 23 that S_T^{SE} is mainly independent of the Debye length, but changes with the salt species. Shown for an 80mer DNA at pH 7 in different salts. Both DNA and H_3O^+, OH^- ions contribute to the electric field. (b) Close to pH 7 the influence of the H_3O^+ and OH^- ion concentration is negligible compared to the salt concentration in the mM range, despite their large Soret coefficients. Here shown for an 80mer DNA which reacts to the electric field but does not contribute to it. (c) Also, the influence of 1 µM DNA is minor, although it is highly charged. The cases shown are when the DNA does not contribute to the electric field (broken line) and when it contributes with its charge and a Soret coefficient of $S_T^{NI} + 1/T + S_T^{CM}$, with the latter depending on the salt concentration.

8.2 TRIS Buffer

There are still other ions in the solution: The buffer TRIS-HCl will be partly protonated corresponding to its buffer capacity. At pH 7.5 most of the molecules will be protonated.

$$[\mathrm{TRIS{-}H^+}] = \frac{[\mathrm{TRIS}] + [\mathrm{TRIS{-}H^+}]}{10^{pH - \mathrm{pKa}(T)}} \tag{28}$$

with pKa the acid dissociation constant and the brackets indicating the concentration. Although we only added 0.5 mM to 1 mM of total TRIS, it is considerably higher concentrated than the DNA, the influence of which we calculated in the last paragraph. The Soret coefficient of the protonated TRIS molecule was not found in literature and it is difficult to measure, since a fluorescent label would change the small molecule considerably. Thus, we assumed its Soret coefficient to be zero. Its counter ion is the chloride ion from the hydrochloric acid, with which the pH was titrated. The electrically neutral TRIS molecules don't contribute to Eq. 22. Now we can calculate and simulate the influence of TRIS on the Soret coefficient (see Fig. 18). As probe particle we used 80mer ssDNA with $Z_{eff} = 7$. The Debye length was titrated with KCl plus a constant 1 mM TRIS pH 7.5.

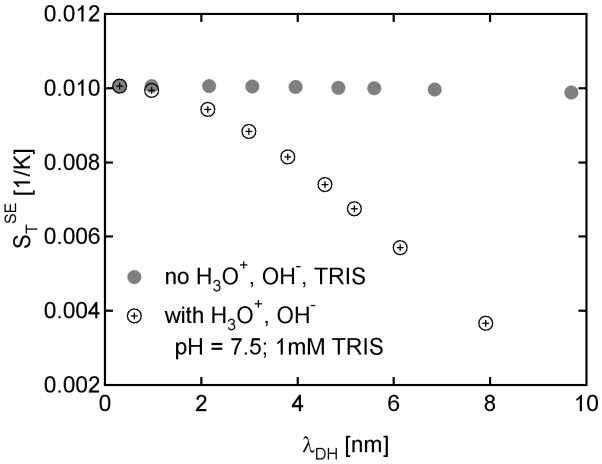

Figure 18: Influence of the TRIS molecule on the Seebeck effect.

We did not find the decrease in the Soret coefficient with increasing Debye length to be as strong as the theoretical prediction in Fig. 18. In the experiments in Fig. 2 only for the 80mer and the 22mer a slight reduction can be found, but not for the 50mer. If the Soret coefficient of the protonated TRIS molecule is not zero, but closer to the potassium ion, the theoretical effect also vanishes. Thus, within experimental error we could not find an effect of the TRIS ion.

8.3 Concentration Measurements

The small influence of the DNA on the Soret coefficient, as discussed in section 8.1, might be just measurable. Thus, we measured differently concentrated DNA from 0.2 to 26 µM of 50mer ssDNA in 10 mM KCl, 1 mM TRIS pH 7.8, 0.05% vol. of Tween. The results are shown as dots in Fig. 19. The LED intensity was adapted to reach the same fluorescence for all sample concentrations. As in all experiments, differential bleaching was corrected for, especially for the lower concentration samples. To describe the concentration dependence analytically, we considered the influence of the DNA concentration and its additional K^+ counter ions on the Debye length in the capacitor model part S_T^{CM} of the Soret coefficient. In addition, the DNA contributes to the electric field (Eq. 22) with $S_{T,DNA} = 1/T + S_T^{NI} + S_T^{CM}$. In order to calculate the Seebeck contribution S_T^{SE}, we assumed the following constants for the 50mer interpolated from the measured values for the 22mer and the 80mer: the hydrodynamical radius $R = 4$ nm, the effective charge number for the capacitor model $Z_{eff} = -16.5$, the temperature $T = 25$ °C, the electric mobility $\mu = 1.44 \cdot 10^{-8}$ m²/Vs, and the non-ionic part of the Soret coefficient $S_T^{NI} = -0.016$ 1/K. The theoretical prediction using these values can be seen as a line in Fig. 19. The measured DNA concentration dependence of thermophoresis can be fully explained by the Seebeck effect and the capacitor model.

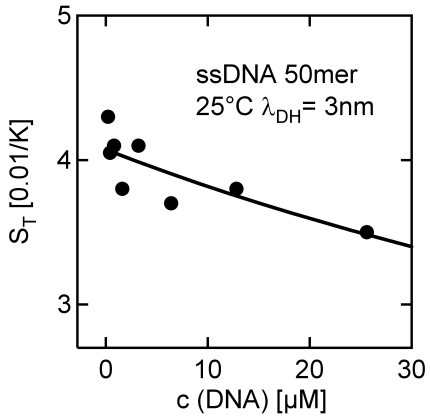

Figure 19: The dependence of the Soret coefficient on the concentration of the sample molecule, here 50mer single stranded DNA, was measured (dots) and calculated (line).

8.4 PEG Crowding Agent

Here we shortly recapitulate the theoretical influence of a crowding agent on thermophoresis through depletion forces. If the sample concentration is on the order of weight percent, or if a crowding agent is present in the solution e.g. PEG (polyethylenglycol), an additional excluded volume effect can be noticed in thermophoresis measurements and should be added to Eq. 4 on page 4. It can be calculated according to [55–57]. The change in Soret coefficient for the molecule of interest, here DNA, is then

$$\Delta S_T = -2\pi(S_T^{PEG} - 1/T)R_{DNA} \cdot R_{PEG}^2 \cdot c_{PEG} \tag{29}$$

with S_T^{PEG} the infinite dilution Soret coefficient of the crowding agent, e.g. PEG, and R_{PEG} its hydrodynamic radius, R_{DNA} the hydrodynamic radius of the particle of interest, e.g. DNA, and c_{PEG} the concentration of the crowding agent.

The Soret coefficient of the molecule of interest, which has a low concentration, depends on the Soret coefficient of the crowding agent, which is added, as well as on its concentration: If the Soret coefficient of the crowding agent has the same sign as the one of the probed molecule, the crowding agent will accumulate on the cold side and displace the molecule of interest. As an example, Jiang et al. measured the Soret coefficient of beads in a solution of the crowding agent PEG without salt [55].

We conducted salt-dependent experiments of 22mer ssDNA and dsDNA and 50mer ssDNA in 3 %wt. and 6 %wt. We used PEG at a molecular weight of 10000 Da, like Maeda et al. [57]. Since pure PEG is a solid with a density of 1.2 g/cm³, we convert the reported 5 %vol. in solution to 6 %wt in our experiments.

Maeda et al. argue that they do not observe accumulation for single stranded molecules. We cannot confirm this and find accumulation for both single and double stranded DNA in PEG. In Fig. 20a both ssDNA and dsDNA of 22mer length show accumulation at 25 °C, in 3 % and 6 % wt. PEG. Accumulation is found when the Soret coefficient becomes negative, i.e. the molecules wander towards the hot side.

As expected from Eq. 29, we find a higher accumulation, i.e. lower Soret coefficients, for higher PEG concentrations.

The reduction in the Soret coefficient caused by PEG is stronger for larger molecules, since the DNA radius enters Eq. 29 (Fig. 20a and b). The difference is even larger, if we consider that without PEG the larger 50mer DNA has a higher Soret coefficient than the smaller 22mer (Fig. 2). As in Maeda et al. [57], we do find higher accumulation for the 50mer than for the 22mer.

In contrast to the study of Maeda et al. we find an increase in the Soret coefficient toward small salt concentration (Fig. 20a and b). This most likely is a result of the capacitor model discussed earlier. For high salt concentrations we see an increase in the Soret coefficient, similar to Maeda et al. [57], which cannot easily be explained and could be the result of DNA-PEG interactions, or artifacts from sticking to the capillary walls. We marked these data points with a circle in Fig. 20 and only fit the spherical capacitor model to the data with longer Debye lengths (for fit parameters see Table 3). If we assume that the hydrodynamic radius does not depend significantly on the PEG and salt concentration, the fit yields about half of the effective charge which is found in aqueous solutions. Alternatively, if we assume the DNA charge to be independent of PEG, a larger radius of the DNA would have to be assumed, in contradiction to the crowding effect. Probably the influence responsible for the strong increase of the Soret coefficient towards very small Debye lengths continues on to longer Debye lengths, but is weaker there. Thus, the shape of this influence is contrary to the shape of the capacitor model and apparently decreases the amplitude from the capacitor model. In the capacitor model a larger charge increases the amplitude with a higher plateau.

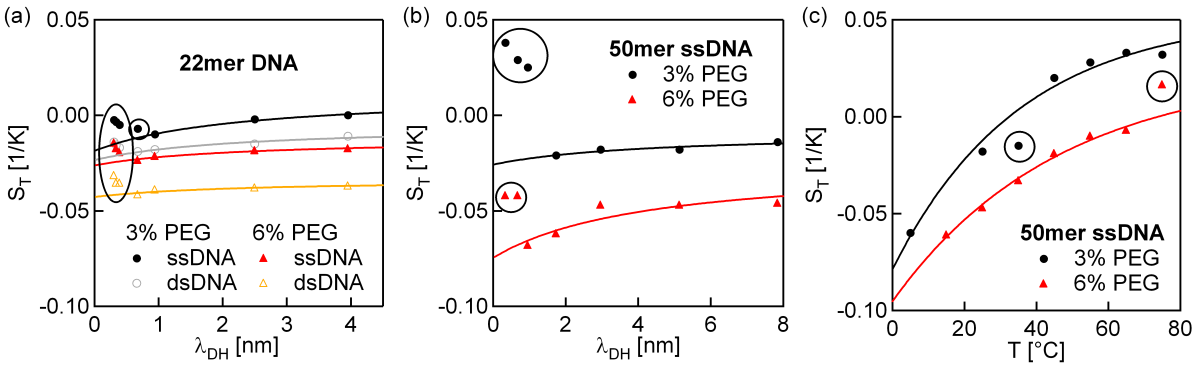

Figure 20: Measurement of ssDNA and dsDNA in aqueous NaCl solutions in the presence of the crowding agent PEG 10000. (a,b) In contrast to the study of Maeda et al. [57] we find negative Soret coefficients, i.e. accumulation also for ssDNA. (c) The sign change is no fundamental difference between ssDNA and dsDNA, but merely the result of different contributions to the Soret coefficient as is shown by a temperature variation. Higher PEG concentration leads to more negative Soret coefficients.

One should not discriminate too strictly between positive and negative Soret coefficients, as the sign is merely a result of which of the components of the Soret coefficient are stronger in the actual conditions. For example, the base temperature of the experiment is varied in Fig. 20c without varying the infra-red laser power and the temperature increase. This will cause a change in the sign, here shown for 50mer

Table 3: Parameters for the fits in Fig. 20. We fitted Z_{eff} and assumed the radius to be $R = 2.0$ nm and $R = 3.7$ nm based on PEG-free measurements of the diffusion coefficient. Temperature was 25 °C, relative permittivity of water $\varepsilon_r = 78$ and its temperature derivative $\partial \ln \varepsilon / \partial \ln T = -1.35$. There was a free offset parameter to account for other contributions to the Soret coefficient

Fig. 20	Z_{eff}
50mer ssDNA 3% PEG	6.2 ± 0.9
50mer ssDNA 6% PEG	10.6 ± 1.4
22mer ssDNA 3% PEG	6.1 ± 0.4
22mer ssDNA 6% PEG	4.2 ± 0.3
22mer dsDNA 3% PEG	4.7 ± 0.4
22mer dsDNA 6% PEG	3.4 ± 0.5

ssDNA in PEG, but a similar dependence is measured in section 7. We fitted the empiric Eq. 27 on page 24 to the data, which was shown to fit DNA for diluted solutions without a crowding agent. This fit yielded $S_T^\infty = 0.052 \pm 0.013$ and 0.024 ± 0.017, $T^* = 32.4 \pm 2.7$ and 73.8 ± 6, and $T_0 = 35.4 \pm 9.8$ and 46.0 ± 15.2 for the 3% and 6% PEG solutions, respectively.

We reassessed the thermophoresis in the crowding agent PEG for single and double stranded DNA [57], but now with covalent markers and cannot confirm a sign change between single and double stranded DNA. Even for 3% and 6% PEG we can fit the salt dependence of DNA thermophoresis with the capacitor model. With PEG both single and double stranded DNA accumulate and deplete to comparable extents.

9 Materials and Methods

9.1 Setup

Measurements were performed with an upright fluorescence microscope (Zeiss Vario Scope.A1) using an air objective (Partec 40x/0.80 NA), a CCD camera (Andor Luca DL-658M-TIL), and heating from an infrared laser (Fibotec, wavelength 1480 nm absorbed in water, typical emission power 28 mW) [17, 21], coupled into the optical path right above the objective. To keep the sample volume low and convection artifacts below experimental error, measurements were performed in thin borosilicate capillaries with an inner rectangular cross section of 50 x 500 µm² (VitroCom Vitrotubes #5005-050). The thin sample and low numerical aperture ensured fluorescence intensity, which was recorded by the camera, was integrated over the capillary height. For a sketch of the setup with its capillary, see Fig. 21.

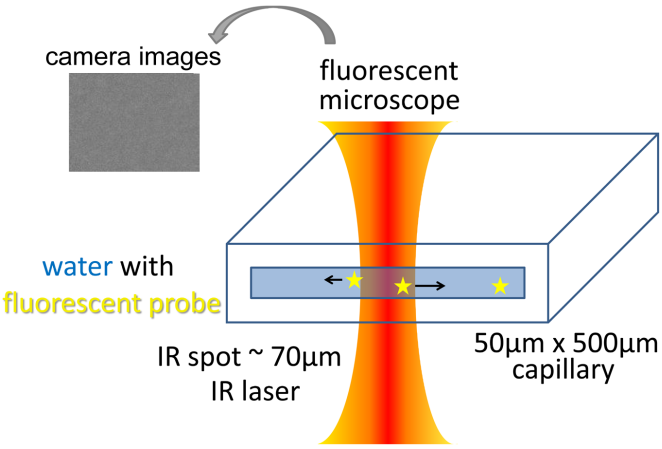

Figure 21: Experimental setup and capillary

9.2 Probes

Single stranded DNA in lengths 2, 5, 10, 22, 50, and 80 bases, covalently labeled at the 5' end with the fluorescent dye HEX (6-carboxy-2',4,4',5',7,7'-hexachlorofluorescein) (Biomers, Germany) was diluted to 1 µM. The DNA sequences can be seen in Table 4. They were designed to form a random coil and exhibit no secondary structure like hair pins. Their Soret coefficients were measured in various electrolytes at 15 °C, except when stated differently.

The electrolyte contained one of the following salts KBr, KCl, KF, KI, NaBr, NaCl, NaF, NaI, LiBr, LiCl, LiI, $CaCl_2$, $MgCl_2$, and was buffered with 1 mM TRIS (2-amino-2-hydroxymethyl-propane-1,3-diol) to a pH of 7.8 at 25 °C. To avoid sticking of the DNA to the capillary walls we added up to 0.1% vol. of Tween 20 in some measurements. Test measurements using 0.02%, 0.05% or 0.1% vol. of Tween 20 revealed no measurable difference in the Soret coefficient. In measurements for the Seebeck effect, the concentration of TRIS was generally reduced to 0.5 mM and titrated to pH 7.5 at 25 °C.

Table 4: DNA sequences

2mer	5'–Hex–TA–3'
5mer	5'–Hex–TAG GT–3'
10mer	5'–Hex–TAG GTC TAA T–3'
22mer	5'–Hex–ATT GAG ATA CAC ATT AGA ACT A–3'
50mer	5'–Hex–ATA ATC TGT AGT ACT GCA GAA AAC TTG TGG GTT ACT GTT TAC TAT GGG GT–3'
80mer	5'–Hex–CCT AAA GTC ATT GCT CCG AAT ATC TAC ACC GAA CCT AGA AAG TTG CTG ATA CCC GAT GTT TGT TTG ATT GTG AGT TGA GG–3'

The profile of the heating spot was measured using the pH dependent fluorescence of the dye BCECF (acid form, Invitrogen B-1151) at a concentration of 50 µM in the temperature dependent pH of 10 mM TRIS-HCl (pH 7.8. at 25 °C). The temperature profile above base temperature was fitted in two dimensions with a Lorentzian $\Delta T\,(r) = \Delta T_{max}/\left(1 + r^2/w^2\right)$. This revealed the heat center, width w, and peak temperature rise ΔT_{max}. The width varied between 30 and 70 $\pm$ 5 µm, well smaller than the field of view, depending on the experiment with a peak temperature increase ΔT_{max} between 1.4 and 4.0 $\pm$ 0.1 K.

The temperature of the surrounding bulk sample, also called the chamber base temperature, was controlled with Peltier elements (Telemeter Electronic GmbH, PC-128-10-05) and a heat bath to fix the temperature on the back side of the Peltier elements. The thin chamber height of 50 µm and the moderate temperature rise of less than 4 K kept thermal convection negligible. The measurement was automated with LabVIEW (National Instruments) controlling LED, IR, motorized stage, temperature, and camera trigger. The concentration of the fluorescently labeled DNA was recorded in space and time with the camera, imaging at 5 Hz [17, 58]. The initial fluorescence of the equilibrated sample was imaged for 5 s, followed by 120 s of thermophoresis under infrared heating, and 120 s of back-diffusion with the laser switched off again.

9.3 Analysis

Since I continued Herzog's experiments [30] and used a similar if not identical setup, the measurements and analysis were the same. The experiment was designed to measure both the Soret coefficient S_T and the diffusion coefficient D. Including pipetting errors and camera noise, the systematic error for the Soret coefficient was estimated to be about 12% [30]. The diffusion coefficients $D(T)$ of single stranded DNA of length 2, 5, 10, 22, 50, and 80 bases at 15°C were 180, 153, 126, 107, 55, and 35 µm²/s, respectively, confirming the values found by Herzog [30]. From these values, the hydrodynamic radii could be calculated with the Einstein-Stokes equation [47] to 1.2, 1.4, 1.7, 2.0, 3.8, and 6.0 nm. These hydrodynamic radii were used for fitting in Eq. 9 on page 6. For analysis, the sequence of measured images, i.e. the fluorescence for all times over the whole field of view of the camera was loaded into a LabVIEW program. After background correction, the measured fluorescence data was circularly averaged around the heating center, which was determined in the temperature profile. As result, even small concentration changes at

large radii could still be detected, since many pixels could be used for averaging. The LabVIEW program triggered a radial symmetrical 1D FEMLAB simulation, which can be obtained from the authors. Width and peak temperature rise of the determined heating profile were fed into the simulation. The program then determined the concentration along the radius for all times, and with this the fluorescence, which was compared to the measured data. The fitting parameters were the Soret coefficient S_T, the mass diffusion coefficient D, the temperature dependence of fluorescence, and the bleaching time scale. Temperature, diffusion and bleaching have time scales of approximately 100 ms, 10 s and 1000 s, so they could be separated and fitted independently. After fitting, the simulation followed the experimental fluorescence data in the full radius-time evolution. Thus, the parameters could be precisely fitted, and experimental artifacts could be detected and excluded, such as empty capillaries, flow drift in in the capillary, inhomogeneous illumination, or a possibly unstable heating profile. With this fitting procedure particularly the Soret coefficient S_T and the diffusion coefficient D could be determined independently.

10 Conclusion

In the first part of this thesis we have shown that the effect thermophoresis is composed of different contributions. Therefore, in different conditions different parts dominate the effect, and we observe different behavior. Our model has been developed for charged particles, highly diluted in aqueous solutions, and at moderate temperature gradients. Our results bridge the gap between phoretic and the diffusive theories. On the one hand the Seebeck effect supports a non-equilibrium model, where global electric field from the Seebeck effect is completely shielded and motion is the result of surface effects only. Here the analogy between thermophoresis and electrophoresis can be drawn [59] and it can be called a thermo-electrophoretic approach. On the other hand, the capacitor model is based on a local equilibrium, where the particles diffuse and distribute according to the Boltzmann law. Here the total energy of the local electric field around a particle changes in the temperature gradient. Our experiments strongly indicate that this thermodynamic approach is also valid for thermophoresis. In the moderate temperature gradients, only moderate concentration gradients establish and the concentration never changes by more than 50% of the initial concentration, and a local equilibrium on the size of the particle exists. The Péclet number (*Pe*) of the molecules is well below one even for the largest DNA (80mer) used in these experiments. We can conservatively estimate the Péclet number with the particle radius $R = 10$ nm, $S_T = 0.1\,\mathrm{K}^{-1}$, and 5 K temperature difference over 10 µm as

$$Pe = R \cdot S_T \nabla T = 10\mathrm{nm} \cdot 0.1\mathrm{K}^{-1} \cdot 5\mathrm{K}/10\mu\mathrm{m} = 5 \cdot 10^{-4} \tag{30}$$

Thus, the particle motion is better described by a diffusion than by a directed, ballistic motion. During the experiment the molecule can diffusively explore all regions and thermodynamic fluctuations are larger than thermodynamic forces. Our theoretical approach correctly predicts a complex, nonlinear size transition, a salt-species dependent offset, and the dependence of thermophoresis on the molecule concentration. We validate the model internally by comparing the charge of the capacitor model (Fig. 6 on page 10) with the electric mobility derived from the Seebeck effect (section 6.2). They can be converted to effective charges by

$$Z_{eff} = \mu \frac{kT}{eD} \tag{31}$$

which results in -1.7 ± 0.2 and -6.3 ± 0.6 for the 2mer and the 22mer, respectively, slightly smaller than the theoretical values of -3.4 and 11.9 from molecular dynamic simulations [36]. On the other hand, the fit with the capacitor model resulted in effective charges $Z_{eff} = -2.5 \pm 0.5$ and -11.0 ± 0.3 for the 2mer and 22mer, respectively. Considering the experimental errors, we find the match between the charge from the Seebeck effect and the charge from the capacitor model convincing. Thus, we have a parameter free model to quantitatively predict thermophoresis, if the molecular parameters from electrophoretic measurements are known. Alternatively, it is possible to measure the effective charge with the proposed thermophoretic measurement. Where the capacitor model accurately yields the absolute value of the molecule's charge, the Seebeck effect allows to directly infer the sign and magnitude of the charge.

Part II

Thermophoresis Inside Living Cells

11 Introduction

The complexity of biology requires that measurements of biomolecular interactions have to be transferred from the test tube to the living cell – "the test tube of the 21st century" [60]. In the first part of this thesis, the molecular origin of thermophoresis has been examined. We have shown that thermophoresis is sensitive to a variety of parameters. Recently, Microscale Thermophoresis has been successful to measure binding affinities in cell lysate [28], but it is not possible to measure inside a living cell with this device from Nanotemper Technologies. Besides *in vitro* applications of thermophoresis, thermal gradients are unique, since they transcend material boundaries and, similar to light fields, are therefore capable of probing molecules even inside living cells. For example, electrical fields are shielded by the cell membrane and electrophoresis inside cells cannot be achieved. The second part of this thesis will bridge the gap and show thermophoresis measurements inside living cells for the first time. For this, a fluorescent microscope setup was used with the central parts modified compared to the commercialized system. We establish an imaging paradigm where the thermal gradient is along the optical axis.

The adherent cells grow on a standard cover slip, and are then inserted into the measurement setup on the cold side opposing an optically heated plate on the bottom. Fluorescence detection is restricted by using TIRF microscopy to the top side, imaging the upward thermophoretic movement towards the cold. Therefore, as the thermophoretic movement is directed perpendicular to the camera plane, thermophoresis can be recorded in parallel for every pixel of the image. With this approach full 3D information of thermophoresis is obtained. These changes allow measuring inside adherent, eucaryotic cells and *in vivo* binding measurements become a realistic goal.

12 Materials and Methods

12.1 Setup

The experiments were conducted with the following setup: An upright fluorescence microscope (Zeiss Axiotech) was equipped with an IR laser (Fibotec, wavelength 1480 nm, max. 300 mW) for heating, and a 488 nm laser (single mode coupled laser, < 50 mW, Visitron Systems GmbH) for TIRF illumination (Fig. 22a). The TIRF laser was focused on the side of the back focal plane of the objective (Nikon, Apo TIRF 100x 1.49 NA oil) and coupled into the light path right above the objective with a dichroic beam splitter (dual line beam splitter z491/561 or dual line notch beam splitter 555/646, AHF Analysentechnik). The excitation filter had enough bandwidth (480/80 and 620/60) to allow the LED illumination light to pass to a good extent the narrow dichroic beam splitter, with which the TIRF excitation was coupled into the light path. As a result, epi-illumination with the LED and TIRF illumination were both possible within the same setup.

12.2 Chamber

Listed from bottom to top, the sample chamber consisted of a 2 mm thick glass slide coated on the top side with 300 nm chromium and a protective 60 nm silicon oxide to prevent a toxic influence on the cells. The aqueous solution was placed on top of the coated glass slide, supplemented with a paraffin oil ring to prevent evaporation. The top of the sandwich structure was formed by a 130 µm thick borosilicate glass cover slip held in place with 12.5 µm thick mylar foil spacers. For cell measurements the cover slip had cells adhering to it upside down.

A spot at the lower interface to the sample was heated by absorbing IR light in the chromium layer. The spot size could be varied with the IR focus. The top cover slip, connected to the immersion oil, acted as heat sink. A camera (PCO sensicam uv) recorded the fluorescence images over time. The images were corrected by subtracting the dark noise of the camera and then normalized by the initial fluorescence in absence of IR heating, in order to correct for inhomogeneous fluorescence and illumination.

12.3 Optics

For DNA measurements in Fig. 27 the IR laser was focused onto the chromium layer (HWHM = 65 µm Fig. 22b). Here, both lateral and vertical thermophoresis could be imaged and compared. In the bead and cell measurements (Fig. 24 and 28) the IR laser was defocused (HWHM $\approx$ 300 µm Fig. 22c) to minimize lateral thermophoresis. Then the temperature gradient was mostly vertical and hardly varied over the field of view. The chamber height without cells was about 20 µm to suppress convection, and was measured optically by focusing the microscope to its boundaries and comparing to a similarly high reference step calibrated with an atomic force microscope. For TIRF illumination we focused on the upper cover slip-glass interface, for LED illumination (except in the bead measurements) to the middle of the chamber. A LabVIEW program automated the measurement. The camera recorded the fluorescence before, during

and after IR heating. Between measurements the sample was left for several minutes to fully equilibrate, or it was moved to measure an unaffected area.

12.4 Bead Measurements

For the high temperature gradient study in section 14.2 we used polystyrene particles (Invitrogen Fluorospheres carboxylate-modified microspheres yellow-green fluorescent, actual diameter 1.95 µm, and crimson fluorescent, actual diameter 1.1 µm), which were washed several times by centrifugation and resuspension in ultra-pure water before diluting them in the final solution. The final concentration of the beads was 5 pM. An air objective (Zeiss EC Plan-NEOFLUAR 40x 0.9 NA) was used with a 0.5x camera adapter (Carl Zeiss Microscopy GmbH, Video-Adapter 60 C ½") for a larger field of view to obtain better particle counting statistics. A sapphire cover slip (Sappro GWI; Grazyna Walawski Industriesaphire, 170 µm thick, 12 mm diameter) was used as a heat sink on the top, prohibiting TIRF illumination due to birefringence, but allowing the application of large temperature gradients at constant temperature, eventually triggering clustering from flow interactions [61]. Particles arriving at the top chamber boundary were counted by integrating the fluorescence pixels above a certain threshold. For this, the high numerical aperture objective was focused on the upper interface to the sample. The beads were classified as being at the upper lid, when they were in focus and their image was only a few pixels wide with the intensity above a defined threshold. To quantify the number of beads at the upper plate, the summed intensity of every pixel above this threshold was computed. An unfocused bead has its intensity smeared over many pixels, so the intensity per pixel was below the threshold and was not counted at all. The IR laser covered 5 times the field of view, and a pure vertical temperature gradient could be assumed. In order to achieve the even higher temperature gradients in Fig. 26 over a large area, a more powerful IR laser was used (IPG Laser, Thulium Fiber Laser, max. 10W, 1940 nm).

12.5 Temperature Profile

The temperature profile was measured using the fluorescent dye BCECF (2',7'-Bis-(2-carboxyethyl)-5-(and-6)-carboxyfluorescein) in TRIS-HCl (Tris(hydroxymethyl)-aminomethan) buffer pH 7.6. BCECF has a pH dependent fluorescence, and TRIS has a temperature dependent acidity constant with roughly $\partial \mathrm{pKa}/\partial T = -0.031$ 1/K. Thus, the pH changes with temperature as visible through the dye's changed fluorescence. Higher temperature results in less fluorescence. Under LED illumination the lateral temperature distribution was imaged, averaging across the thickness of the chamber. A three-dimensional impression of the temperature distribution was subsequently gained from the finite element simulation (Fig. 22b, c). A two-dimensional Lorentzian $\Delta T = \Delta T_{max}/(1+(r/w)^2)$ was then fitted to the image, with r the distance from the heat center, and three free parameters: peak temperature rise ΔT_{max} above ambient temperature, center of the heat spot, and width w. These parameters were then used in the analysis of the measurements (section 13.1).

12.6 DNA Measurements

Thermophoretic imaging of DNA (section 14) was performed with lengths 0.6, 1, 3, and 20 kilo base pairs (kbp) from Fermentas (SM1461, SM1671, SM1711, SM1541) at 50 µM base pair concentration, labeled with 2 µm TOTO-1 iodide (Invitrogen) in 1 mM KCl pH 5 (Fig. 27A) or in 1mM TRIS buffer pH 7.4 (Fig. 27B). Thus, on average every 25 base pairs a dye molecule was bound. For the latter experiments, the cover slip was coated with bovine serum albumin (BSA, Roth, Albumin Fraktion V) to reduce adhesion of the DNA to the surfaces of the chamber. For this, the cover slips were cleaned with Hellmanex II (Hellma Optics), water, and isopropanol each for 10 min in the ultrasound bath, then dried with nitrogen and incubated for one hour at room temperature with 10 mg/ml BSA. As expected, the response time of the system strongly depends on the distance, which the molecules need to diffuse, i.e. here the chamber height versus the heating spot width. The chamber heights were individually measured for the different samples (see section 12.3).

12.7 Cell Culture

Adherent HeLa cells (ATCC CCL-2, LGC Standards) were grown in minimum essential medium (Eagle) with 2 mM L-glutamine and Earle's salts adjusted to contain 2.2 g/l sodium bicarbonate, 0.1 mM non-essential amino acids, 1.0 mM sodium pyruvate and supplemented with 10% fetal bovine serum (FCS). The cells were regularly split about 1:5 twice per week. The cover slips were cleaned in an ultrasonic bath with Hellmanex II (Hellma Optics), ultra-pure water, and isopropanol, dried with nitrogen, sterilized in an autoclave, and coated with approximately 5 µg/cm² poly-L-lysine (Biochrom AG) by incubating for 30 min at room temperature prior to seeding cells on them.

12.8 Cell Transfection and Measurements

The cells were grown on the cover slips overnight and stained before the measurement with BCECF-AM by incubating for 1 hour with 2 µM BCECF-AM ester (2',7'-Bis-(2-carboxyethyl)-5-(and-6)- carboxyfluorescein acetoxymethyl ester, VWR International GmbH Deutschland). Alternatively, they were stained by lipofection with 21mer double stranded DNA, which was covalently labeled with Cy 5 (sequence 5'-Cy 5-GTT GGA AGG TGG TCA AGG TGC-3' with the unlabeled complement, metabion international AG). The DNA was brought into the cell with the reagent Roti-Fect PLUS (Carl Roth) according to the instructions. BCECF-AM can diffuse through the cell membrane. Inside the cell, it is cleaved into BCECF, a form in which it fluoresces and diffuses out again only at a very small rate [62]. The cells were rinsed with phosphate buffered saline PBS (137 mM NaCl, 2.7 mM KCl, 10 mM $NaHPO_4$, and 2 mM KH_2PO_4, pH 7.4) and together with the cover slip they were assembled onto the chamber. Measurements at room temperature were possible for up to one hour in normal cell morphology. Cell viability was tested with the inherent BCECF-AM test [63]. We refrained from measuring very bright cells, since we suspected that these cells were under less physiological conditions with too much fluorophore inside.

Alternatively, we used HeLa cells with a green fluorescent ribosomal protein (obtained from Ina Poser from Max Planck Institute of Molecular Cell Biology and Genetics in Dresden, Germany). The human cell line HeLa-Kyoto was stably transfected with a GFP-tagged BAC expressing human RPL10 (BAC ID: CTD-2511C7 (human DNA) gene: RPL10 (ENSG00000147403) internal ID: MCP_ky_3296). The stop codon of RPL10 was replaced by a BAC-tagging cassette (LAP-tag). Correct integration was verified by PCR and sequencing. The culture conditions were DMEM (high glucose), and 10% FCS. To maintain selection the antibiotic G418 (Invitrogen) was added in 400 µg/ml. The cells in this cell pool were differently bright, since they had a different amount of GFP copies. As the GFP labeled ribosomal protein was not over-expressed, they were darker than the cells, which we had loaded with more BCECF.

13 Finite Element Calculations

A finite element simulation method (FEMLAB 3.1, COMSOL AB) was used to model the experiments both without and with cells.

13.1 Temperature Field Model

For the temperature model we used a two-dimensional radial simulation with a chamber height of 10 µm and a cover slip height of 130 µm. The chamber radius was 0.5 mm. As modules we used incompressible Navier-Stokes to model convection in water (viscosity $\eta = 1\text{mPas}(1+0.022\Delta T)$; density $\rho = 988\,\text{kg/}m^3(1-0.0003\,1/\text{K}\,\Delta T)$) and heat conduction in the water with 0.597 W/mK and in the glass cover slip with 0.8 W/mK, with the additional constants heat capacity of water 4187 J/(kgK) and of the cover slip 700 J/kgK with the glass density of 2480 kg/m³. The temperature rise was set in the lower boundary of the chamber to $\Delta T_{max}/\left(1+(r/w)^2\right)$ with r the radial coordinate, the peak temperature $\Delta T_{max} = 5$ K, and the width w = 15 µm or 150 µm.

13.2 Bead Thermophoresis Model

For the bead simulation a one-dimensional (non-radial) diffusion model was set up with chamber height h = 20 µm and the following parameters: bead radius R_{bead} = 1 µm, dynamic viscosity $\eta = 1$ mPas, gravity $g_0 = 9.81$ m²/s², Boltzmann constant $k = 1.38\ 10^{-23}$ J/K, base temperature T_0 = 300 K, temperature gradient $\nabla T = -0.07, -0.14, -0.21, -0.31, -0.4$ K/m, a mass density difference of the dye soaked beads to water of $\Delta\rho = 60$ kg/m³, the mass diffusion constant of the beads $D = kT_0/(6\pi\eta R_{bead})$, their thermodiffusion constant $D_T = 2.8$ µm²/(sK), sedimentation force and velocity $F_{sed} = 4/3R_{bead}^3\pi\Delta\rho g_0$ and $\vec{v}_{sed} = F_{sed}/(6\pi\eta R_{bead})$, respectively, the times $start = 10$ s and $end = 210$ s, the initial concentration distribution

$$c_0 = hF_{sed}/(kT)\exp\left(-F_{sed}x/(kT)\right) \tag{32}$$

and the temporal temperature gradient $\nabla T' = (t > start)\,(t < end)\,\nabla T$. The differential equation was set up with the particle flux $-D\nabla c - D_T\nabla T' c - \vec{v}_{sed}c$ and the fluorescence was integrated over 2 µm from the top.

13.3 DNA Thermophoresis Model

To analyze the DNA a two-dimensional, radial FEMLAB model was set up. We simulated the temperature increase, and with this temperature gradient we simulated the fluorophore concentration, determining the fluorescence intensity in the measurements. We used the FEMLAB modules heat transfer by conduction, incompressible Navier-Stokes, convection and diffusion with following parameters: heat conduction of water 0.597 W/mK and of the glass cover slip 0.8 W/mK, heat capacity of water 4187 J/kgK and of the cover slip 700 J/kgK with the glass density of 2480 kg/m³, the cover slip thickness = 130 µm, chamber radius = 1 mm. The measured chamber height h directly influenced the geometry of the model.

The mass diffusion coefficient D and thermo-diffusion coefficient D_T varied when the model was fitted to the data. The bleaching rate k_{off} and the TIRF penetration depth or LED focus height λ depend on the illumination.

We modeled the temperature increase in the chromium layer by setting the temperature rise in the lower boundary of the chamber to a Lorentzian modulated with a smoothed Heaviside function:

$$\Delta T = \Delta T_{max} / \left(1 + r^2/w^2\right) flc2hs\left(t - start, H\right) flc2hs\left(end - t, H\right) \tag{33}$$

with the time t and the radial coordinate r. The peak temperature rise ΔT_{max} and width w were taken from the heat spot measurement. The heat equilibration time was $H = 0.1$ s, and the IR switching times $start = 60$s and $end = 120$ s, which were later rescaled to 0 s and 60 s. We set the outer boundaries and the top of the cover slip to zero temperature increase.

For convection we used the density of water $\rho = 998$ kg/m³ and its viscosity $\eta = 1$ mPas. Thus, the buoyancy volume force is $F_z = \Delta T \cdot 3\,10^{-4} 1/\mathrm{K} \cdot \rho g_0 \approx 3\Delta T$ N/(m³K). The fluorescence distribution then is $F = c(1 - T\alpha)$, with the fluorophore concentration c and the known temperature dependence α fluorescence of the fluorophore.

The initial fluorophore concentration c_0 was set to 1 everywhere and the initial temperature rise to 0. The differential equation system was modified in the particle flux as $-r(D\nabla c + D_T \nabla T)$. In the source term we find the bleaching either for TIRF illumination

$$R = -c\, k_{off} \exp\left((z-h)/\lambda\right) \tag{34}$$

or for LED illumination

$$R = -c\, k_{off} / \left(1 + |z-h|^2/\lambda^2\right) \tag{35}$$

Thus, in TIRF illumination only the fluorophores close to the cover slip are subject to bleaching. The fluorescence was then inferred from the simulation by

$$F / \left(1 + |z-h|^2/\lambda^2\right) / h \tag{36}$$

for LED illumination, or by

$$F \cdot \exp\left((z-h)/\lambda\right) / \lambda \tag{37}$$

for TIRF illumination with z the height coordinate.

The solid lines in Fig. 27 are theoretical predictions, using the finite element simulation strategy discussed above. To fit these traces of different laser powers (Fig. 27a) and different DNA lengths (Fig. 27b) we used the parameters from Table 5.

Table 5: Parameters for the simulations in Fig. 27 on page 51

	Fig. 27a	Fig. 27b
DNA length	1 kbp	0.6, 3, and 20 kbp
w	65 µm	65 µm
ΔT_{max}	0, 4.5, 10, or 15 K	6 K
h	13 µm	16.4, 19.3, or 25.5 µm
D	10 µm²/s	14, 6.0, or 2.5 µm²/s
D_T	2.8 µm²/(sK)	2.2, 1.5, or 1.1 µm²/sK
α	1.2 %/K	1.7 %/K
k_{offLED}	0.035 %/s	0.06 %/s
$k_{offTIRF}$	5 %/s	0.06 %/s
λ	200 nm	100 nm

13.4 Intracellular Thermophoresis Model

We assumed that cells consist primarily of water [64]. Therefore, their presence hardly disturbs the vertical temperature gradient. As a result, the simulation could be reduced to one vertical dimension with constant temperature gradient. We estimate that the chamber height was higher than in non-cell measurements due to cell culture procedures, roughly about 30 µm, allowing an estimation of the applied thermal gradient. For the cell simulations we used a one-dimensional, purely diffusive model with parameters: mass diffusion coefficient $D = 3$ µm²/s for BCECF and $D = 0.1$ µm²/s for the 21mer DNA, TIRF penetration depth $\lambda = 200$ nm. Start and end times for the IR laser were set according to the experiments and later rescaled to 0 s and 30 s. Heat equilibration time was set to $H = 0.2$ s. With this the temperature gradient and thus the thermophoretic velocity $\vec{v}_T$ could be modulated with time t as

$$\vec{v}_T' = \vec{v}_T\left(1-\exp\left((start-t)/H\right)\right)(t > start) - \vec{v}_T\left(1-\exp\left((end-t)/H\right)\right)(t > end) \tag{38}$$

$\vec{v}_T'$ is required to model switching heating on and off in the simulation. It approaches $\vec{v}_T$ when the heating is switched on and approaches zero at other times.

Bleaching depends on the illumination and is found in the source term of the differential equation for TIRF illumination to be

$$R = -c\,k_{off}\exp\left((x-h)/\lambda\right) \tag{39}$$

or for LED illumination to be

$$R = -c\,k_{off}/\left(1+|x-h|^2/\lambda^2\right) \tag{40}$$

with x being the height coordinate. The particle flux was defined as $-D\nabla c + \vec{v}_T' c$. The initial concentration was set to 1 everywhere and the initial temperature rise to 0. The concentration was read from the simulation and weighted with the LED illumination $c/\left(1+|x-h|^2\lambda^2\right)/h$ or weighted with the TIRF illumination $c\exp\left((x-h)/\lambda\right)/\lambda$. Subsequently, the temperature dependence $T\,jump = \alpha\Delta T$ with α the

temperature dependence of the dye and D_T the temperature rise, was included by multiplication with

$$1 - T\,jump\,(\exp((end - t)/H) - \exp((start - t)/H)) \tag{41}$$

after the IR was turned off again, and by

$$1 - T\,jump\,(1 - \exp((start - t)/H)) \tag{42}$$

for the time after the IR was turned on and before it was turned off again. For the two-dimensional cell model, the model is identical, except that the height coordinate is called z. The readout is then $c/\left(1+|z|^2/\lambda^2\right)/h$ for LED illumination with h being the height in the center 10 µm and $c\exp(z/\lambda)/\lambda$ for TIRF illumination .

14 Setup Verification

In this section we test the setup. With it we can compare vertical and lateral thermophoresis. In vertical thermophoresis the molecules usually move upwards and are pressed against the cover slip. This can be obtained when the IR is defocused and the whole bottom is heated. In lateral or horizontal thermophoresis the molecules move outwards toward the unheated, surrounding bulk. Sometimes, however, when their Soret coefficient is negative, the molecules move exactly to the other direction. Horizontal or lateral movement was examined in detail in the first part of this thesis when we heated inside the water. If the heating is focused to a small spot in the chromium layer (Fig. 22b without cells), the molecules move in both directions, and thus those two directions can be compared.

We use a thin sheet of solution to suppress convection. Previous measurements [17] showed that convection is negligible when the measurement chamber is flat enough. We apply the temperature gradient with a cold top and a warm bottom. The latter was heated by an IR laser, which is absorbed in a chromium layer directly at the sampler border. Fluorescence detection is restricted to the top side by using TIRF microscopy, imaging the upward thermophoretic movement towards the cold. In this geometry every camera pixel can simultaneously and independently measure thermophoresis, since the image plane is normal to the thermophoretic movement. For details on the components used see section 12.1. The temperature profile was measured using the fluorescence of BCECF as described in section 12.5. Under LED illumination the lateral temperature distribution is imaged, averaging across the thickness of the chamber. The images and the known geometry were used to fit a three-dimensional finite element calculation (Fig. 22b and c).

14.1 Chromium Layer

We confirmed that the chromium layer absorbed all the infra-red (IR) light by measuring the transmission of the IR laser through the chromium coated glass slide with a power meter (PM100USB and S310C Thorlabs GmbH). As a result, the upward movement of the particles could not be influenced by photonic pressure. As additional check we performed experiments under TIRF detection without chromium. The resulting lack of a vertical temperature gradient coincided with an undetectable vertical net movement of the molecules.

14.2 Bead Measurements

We first used polystyrene beads to confirm the thermal transport approach. In a 20 µm high chamber comparably large polystyrene beads with Radius $R_{bead} = 1$ µm sediment and in the beginning of a measurement and sit on the bottom of the chamber in a Boltzmann distribution. During the measurement, particularly when the heating is turned on and a temperature gradient applies, the beads are transported to the top side where they are detected via fluorescence. At the top of the chamber the thermophoresis enforces an inverted exponential sedimentation distribution. In the steady state thermophoresis is balanced by sedimentation and diffusion. Fig. 23 shows their distribution for various times of the experiment. A

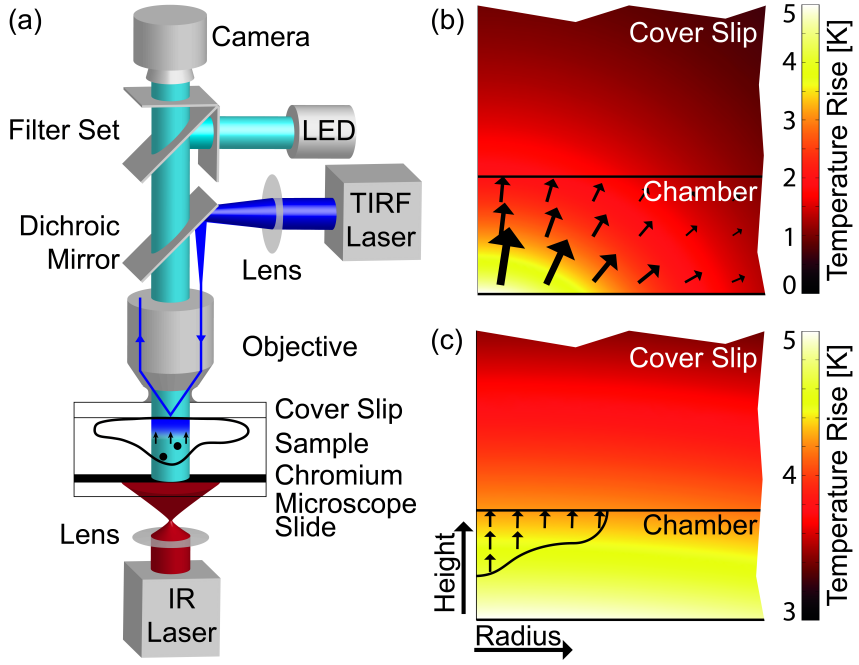

Figure 22: Setup. (a) Two illumination paths were implemented in an upright fluorescence microscope setup: normal epi-illumination with LED, and TIRF illumination. Heating is provided from below by an IR laser that was absorbed by a chromium layer at the lower sample interface. The temperature simulations are shown for a 10 µm thick chamber with variable IR spot in the shape of a Lorentzian and with variable focus width: (b) 15 µm and (c) 150 µm, and peak temperature 5 K. The molecules move along the temperature gradient, indicated by arrows.

one-dimensional finite element simulation was used to model the combined gravitational, diffusional, and thermophoretic movement of the beads. Details about the simulation can be found in section 13.2.

The bead concentration at the top was detected by fluorescence with a special mode specified in section 12.3. With increasing temperature gradient the beads travel across the chamber with increasing speed, and from their velocity the diffusion coefficient can be calculated according to Eq. 1 $\vec{v}_T = -D_T \nabla T$. For shallow thermal gradients they can barely overcome sedimentation, which was calculated from the weight difference to water of $\Delta\rho = 60$ kg/m³ (Fig. 24). With the known mass diffusion coefficient of the beads ($D = 0.20$ µm²/s) interfered from their radius, the only fitting parameter is the thermophoretic mobility D_T which was fitted to a constant value of 2.8 ± 0.5 µm²/(sK) for all measured thermal gradients. For further bead measurements see the Bachelor thesis of Passvogel [65].

The setup is also suitable to apply high temperature gradients, due to the complete absorption of the IR light at the chromium layer, the small chamber height, and the sapphire as heat sink. For large particles, e.g. µm sized polystyrene spheres, it is possible to reach Péclet numbers larger than one. The measurement setup allows to probe thermophoresis for Péclet numbers smaller and larger than one [61]. At the highest temperature gradient of 0.2 K/µm the Péclet number reaches $Pe = (R \cdot \nabla T \cdot D_T / D) = 2.7$, indicating that the comparably large beads and the considerable thermal gradient allow for a ballistic,

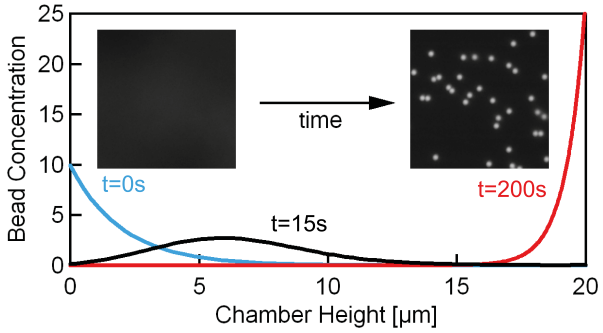

Figure 23: Imaging thermophoresis with beads. (a) Polystyrene particles with radius $R = 1$ µm initially sediment and during the measurement move upwards to be imaged at the top the top of the chamber. Simulation shown for a gradient of $\nabla T = 0.2$ K/µm.

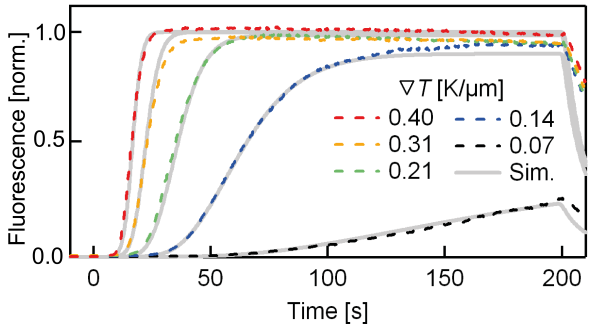

Figure 24: Imaging thermophoresis with beads. Fluorescence is used to image the concentration of the beads at the top of the chamber. With increasing thermal gradient the transit times of the beads become shorter. All measurements are described with a thermophoretic mobility of $D_T = 2.8 \pm 0.5$ µm²/sK and the mass diffusion coefficient $D = 0.20$ µm²/s known from the particle radius.

not a diffusional particle movement. At the lowest temperature gradient of 0.07 K/µm thermophoresis is barely able to overcome sedimentation and $Pe = 0.98$, and $Pe < 1$ can be reached for molecules and beads with smaller radius. This way the transition in thermophoresis between the diffusive and the ballistic regime of particle transport can be examined. In the limit of small temperature gradients a local equilibrium approach proved successful [29, 33]. The limit is given in [61] as $\nabla T < (R \cdot S_T)^{-1}$, i.e. for Péclet numbers $Pe > 1$. For these conditions the particles cluster at the upper glass surface (cf. Fig. 25) due to the Marangoni-like fluid flow around them [61]. This was observed in the measurements with high temperature gradients in Fig. 24.

Above this limit the theoretical foundation is unclear, since for example the Debye-Hückel shielding sphere might be distorted. The thermophoretic mobility D_T or the Soret coefficient S_T might change with the temperature gradient. Discrepancies have been measured into both directions: Here we measure an increase in D_T, and in [33] a decrease for high ∇T is indicated. Converting the laser current into an actual temperature gradient is difficult. The optical laser power was measured with a pyrometer, and it is approximately linear with the laser current (see Fig. 26). The absorption on the chromium

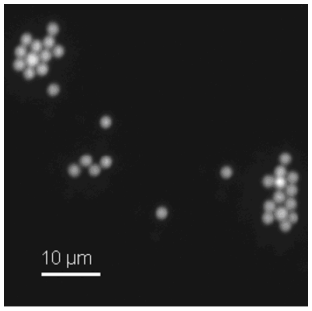

Figure 25: Clustering 2 µm beads on the upper surface. Fluorescent image of beads clustering when pressed against the glass cover slip and when the temperature gradient exceeds $\nabla T > (R \cdot S_T)^{-1}$.

layer (about 300 nm thick) was checked to be complete, so the temperature gradient can be assumed to be linear with the measured laser power. The beads at the top could be counted. In Fig. 26 the measurements of the velocity $\vec{v}_T$ of 1 µm red fluorescent polystyrene particles is shown in different buffers with 10 mM monovalent salt. If D_T was a constant, we would expect $\vec{v}_T$ to rise linearly with the temperature gradient or the IR laser power or the IR current, but our measurements deviate from this linearity. The measurements in Fig. 26 bend upwards at about 1.2 A and show a higher velocity than expected from the low temperature gradient regime.

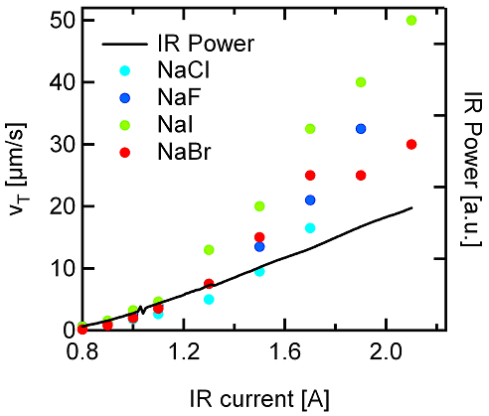

Figure 26: Thermophoretic drift velocity for different temperature gradients. The IR power is approximately linear with the IR current, but the thermophoretic velocity of 1 µm red fluorescent polystyrene particles bends upwards at about 1.2 A. The measurement was repeated in different electrolytes.

A higher D_T is actually expected: Since we need to heat the bottom glass plate more for higher temperature gradients, the average temperature of the sample is higher. In section 7 we also found a higher Soret coefficient for higher base temperatures. Additionally, the mass diffusion coefficient will increase with higher temperature, with the explicit temperature dependence, and with the decreasing viscosity of water η:

$$D = \frac{kT}{6\pi\eta R} \tag{43}$$

So even for a constant Soret coefficient, we expect higher D_T at higher temperatures.

14.3 DNA Measurements

Before performing measurements in cells, the imaging thermophoresis configuration using TIRF detection was first tested with DNA where sedimentation is not an issue (Fig. 27). We study the case where focused heating (Fig. 22b) combines vertical and lateral thermophoresis. With epi-illumination using an LED detection averages across the chamber height, and only the lateral outwards movement is detected. Under TIRF illumination both the coaxial upward and lateral outward component of thermophoresis is measured.

We used DNA of different length as a molecular test system due to their well-established parameters. Measurements were performed at different thermal gradients under both TIRF and LED detection (Fig. 27 dotted lines). Fluorescence at the heat spot center was recorded at 3 Hz. When heating is turned on ($t = 0$ s), fluorescence drops within < 1 s due to its inherent temperature dependence. Under TIRF illumination this drop is superimposed with the fluorescence rises due to the upward molecule movement. This is later decreased by the lateral outward thermophoresis due to the focused heating spot. The thermophoretic amplitude increases for an increasing temperature gradient (Fig. 27a). Under epi-fluorescent LED illumination only the temperature dependence and the lateral outward depletion of the molecules is visible. Measurements with longer DNA strands show slower diffusion, and the coaxial upward thermophoresis is detected, since the lateral thermophoresis does not yet equilibrate within the heating time of 60 s (Fig. 27b). After switching off the temperature gradient ($t = 60$ s) back-diffusion equilibrates the thermophoretic perturbation of DNA concentration.

We quantified the DNA measurements with the known molecular parameters in a two-dimensional, radial finite element simulation (section 13.3). We implemented heat conduction, diffusion, thermophoresis, bleaching under TIRF or LED illumination, temperature dependence of the fluorescent dye, and a possible thermal convection flow. The resulting fluorescence traces fit the experimental measurements in detail over a wide range of temperature gradients and DNA lengths (Fig. 27). The mass diffusion coefficient could be determined by the model to $D = 14, 10, 6.0, 2.5$ µm²/s for the lengths of 0.6, 1, 3, 20 kbp, respectively, which agreed with literature values [66]. The only unknown parameter was the thermophoretic mobility D_T. For the measured DNA lengths of 0.6, 1, 3, 20 kbp we found $D_T = 2.2, 2.8, 1.5, 1.1$ µm²/sK, confirming previous measurements of DNA thermophoresis [17]. Interestingly, we could fit both the coaxial and lateral thermophoresis traces with the same value for the thermophoretic mobility D_T. For details on the fits see section 13.3.

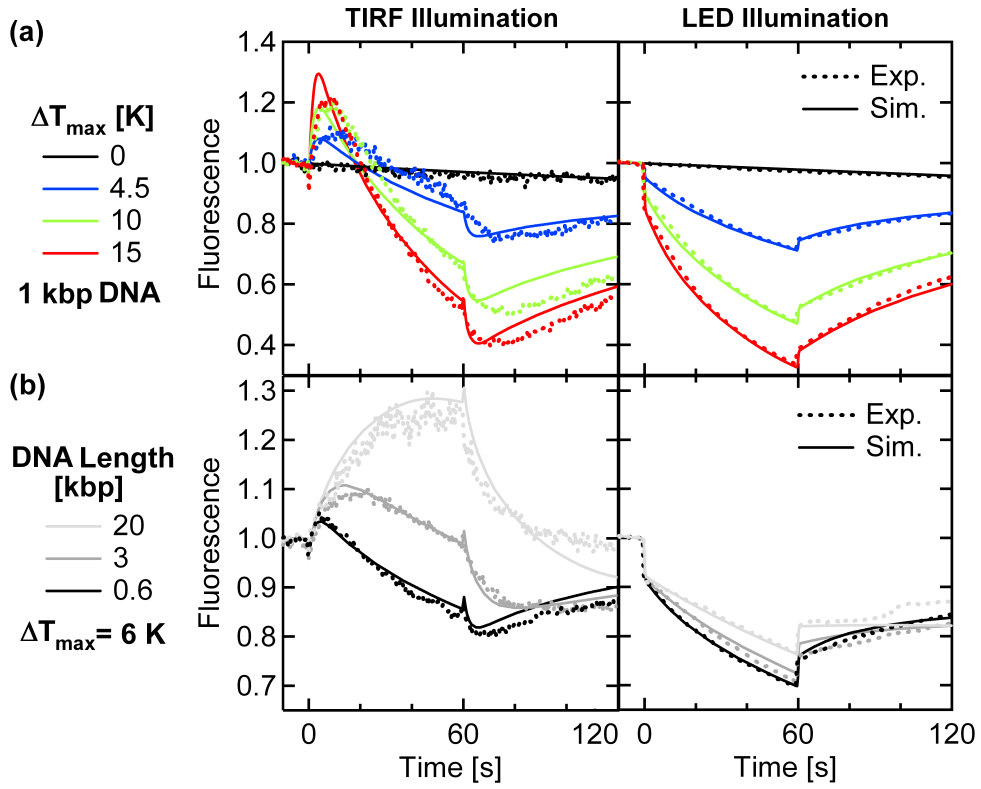

Figure 27: The IR laser was focused to a small spot (HWHM = 65 µm) and moved the molecules upwards coaxially and outwards laterally. The fluorescence above the heat spot center was detected with TIRF. Epi-fluorescence LED illumination did not discriminate across the chamber height. Measurements (dotted line) were conducted with (a) 1 kbp DNA in different temperature gradients and (b) different DNA lengths in the same temperature profile. Finite element simulations described the thermophoretic molecule movement in detail (solid lines).

15 Cell Experiments

We imaged thermophoresis inside living cells after fully understanding thermophoresis traces under the TIRF detection and coaxial heating. The measured fluorescence traces of thermophoresis inside living HeLa cells are shown in Fig. 28.

15.1 Cell Measurements

The IR heating laser was turned on between times 0 s and 30 s. As before, the temperature dependence of the fluorophore results in a sudden drop of the signal, after the IR is switched on, and a reverted increase after heating is switched off again. As before, control measurements under epi-fluorescence LED illumination were conducted. Here an axial, upward fluorophore motion cannot be resolved and only the temperature jump is visible (Fig. 28a). With LED illumination the temperature jump is slightly larger than under TIRF illumination, since the LED excites the fluorescence deeper in the chamber, where it is warmer (see Table 6). Lateral thermophoresis is also not expected due to the more defocused heating in the cell measurements (see Fig. 22c). Fig. 28b shows a measurement of 21 base pair DNA, while the other measurements report the movement of the pH sensitive dye BCECF. As before, the measurements were fitted with finite element simulations as detailed in the supplementary section. All parameters are listed in Table 6.

Interestingly, the diffusion of BCECF was found to be $D = 3$ µm²/s, considerably slower than the free buffer values from the cytoplasm of 100 µm²/s reported using FRAP analysis of the mobile fraction [67]. For the measurements with 21mer double stranded DNA we find a diffusion coefficient of 0.1 µm²/s, which is also reduced compared to the reported 20 µm²/s [68]. Since this method actively moves the molecules, it measures the average over all fractions mobile and possibly immobile. The main contribution in slowing down diffusion is thought to be the collision with other macromolecules, and the effect is stronger for larger molecules [68, 69]. Thus, a size dependent further reduction of these values is expected when thermophoresis of biomolecules bound to other molecules is considered. We also tried to measure larger molecules (ribosomes with GFP label section 6), but the reduction of diffusion made it impossible to detect sufficient (thermophoretic) movement. Thermophoresis, in contrast to all other techniques, actively moves the molecules and therefore probes their mobility on a global scale. As a result, interactions with the cytoplasm at a larger scale can be probed by thermophoresis.

Interestingly, for BCECF the thermophoretic mobility is unaffected by the cell. The measured value of $D_T = 4.4 \pm 2$ µm²/(sK) is well compatible with the reported *in vitro* value of $D_T = 7.5$µm²/(sK) [17]. In contrast, the DNA probe is reduced both in diffusion and thermophoretic mobility with a value of $D_T = 0.12$ µm²/(sK) as compared to $D_T = 1$µm²/(sK) [70]. These measurements suggest that molecular interactions inside a cell can be differentiated between affecting thermophoretic mobility or diffusivity.

In Fig. 28c and d the thermophoresis traces show a curved fluorescence decrease during thermophoresis which could not be readily explained even with TIRF bleaching dynamics in the one-dimensional simulations (broken line). We propose that this effect is due to the inhomogeneous thickness of the in-

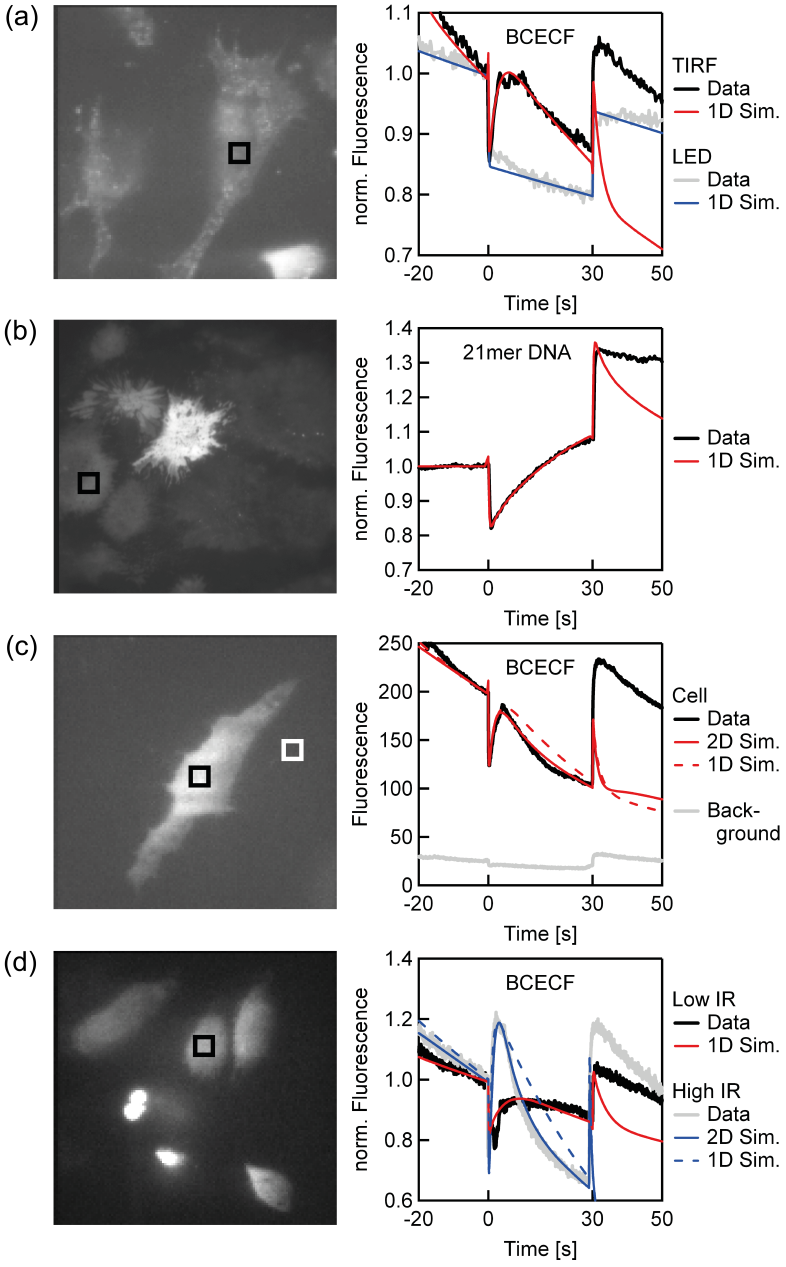

Figure 28: Thermophoresis measurements of DNA and BCECF in the cytoplasm of living cells. On the left sides, the fluorescence image of representative cells are shown. Thermophoresis of molecules was detected by TIRF fluorescence imaging over time. The time traces on the right correspond to the intensities in the black squares in the cell image.(a) The dye molecule BCECF is moved to the cold side after a fast fluorescence decrease due to its temperature dependence. Control measurements under epi-illumination with LED demonstrate that the fluorescence increase stems only from the vertical movement of the fluorophore. (b) Double stranded DNA with 21 bases showed slower thermophoresis with a larger accumulation magnitude than BCECF. (c) The extracellular background trace is darker, does not show the thermophoresis signature, and is not affecting the thermophoresis measurement significantly. The bending of the trace is understood with the cone-shaped cell geometry. (d) Measurements in higher temperature gradients show an expected increase in the thermophoretic amplitude.

dividual cell, leading to a temporarily build-up of lateral concentration inhomogeneities within the cells that subsequently equilibrate. We modeled such a cell in a two-dimensional radial geometry, as a cone with height 10 µm and radius 20 µm, the readout being above the center, but still with a purely vertical, constant temperature gradient. This two-dimensional model could explain the curved cell traces (section 13.4).

Background fluorescence could be measured next to a cell (Fig. 28c, white box). Even for this example of high background levels compared to the non-cell measurements, its minor dynamics upon heating did not significantly affect the thermophoretic analysis.

The setup geometry is capable of simultaneously measuring vertical thermophoresis in cells at various positions in the field of view of the camera. For the used molecule systems we did neither expect nor record significant deviations of D_T and D across the image of the cell. It is interesting to note that the reallocation of the molecules by thermophoresis resulted in a much reduced kinetics of the back-diffusion dynamics which could not be fully accounted for by the thermophoretic model for the cell measurements. They were perfectly understood for the measurements without the cells. This points to a yet to be understood cellular dynamics induced by the global application of a temperature field. One should note that the cells are located at the cold side of the chamber.

In Fig. 28d traces with different heating intensities are shown. At a 5-fold higher temperature gradient, a larger thermophoretic amplitude is found after the also increased temperature jump. The diffusion coefficient is not affected and traces are well fitted by the thermophoretic model. Thermophoretic mobility raises slightly more than expected from temperature dependent *in vitro* data [17, 70], indicating that intracellular binding inside the cell is reduced by the increased temperature.

Table 6: Parameters used for the simulations in Fig. 28. At varying laser powers different temperature gradients ∇T were applied. The temperature dependence α of the used fluorophore was fitted, but not calibrated due to an unknown pH dependence upon temperature changes inside the cell. The thermophoretic mobility of BCECF and DNA could be determined from the thermophoretic velocity $\vec{v}_T$ used to fit the fluorescence transients. We implemented bleaching for TIRF and LED illumination in the simulation with a bleaching rate k_{bleach}. TIRF illumination only bleached the fluorophores close to the cover slip with a penetration depth of $\lambda = 200$ nm. The chamber height is denoted with h. Grey columns denote fitting parameters, others are measured or derived values.

Fig. 28	Molecule	∇T [K/µm]	$\alpha \cdot \Delta T$ [%]	h [µm]	$\vec{v}_T$ [µm/s]	D_T [µm²/(sK)]	k_{bleach} [%/s]	D [µm²/s]
(a) TIRF	BCECF	0.076	20	8	0.24	3.2	15	3
(a) LED	BCECF	0.076	15	8	0.24	3.2	0.2	3
(c) 1D	BCECF	0.17	45	8	0.60	3.6	35	3
(c) 2D	BCECF	0.17	45	cone	0.66	4.0	15	3
(d) 1D	BCECF	0.034	21	10	0.15	4.4	13	3
(d) 2D, 5xIR	BCECF	0.17	47	cone	1.32	8.0	10	4
(b) DNA	22mer	0.17	22	5	0.021	0.12	0	0.1

15.2 Repeated Heating

In several experiments we heated the same cells twice. One such case can be seen in Fig. 28d. There the first heat pulse was for 30 s with only a moderate temperature increase of 5 K. The second pulse was after 210 s with a higher temperature gradient ($\Delta T_{max} \approx 24$ K) and did show thermophoresis. In another measurement we heated the cells twice with only 100 s in between and both with high laser power ($\Delta T_{max} \approx 24$ K). As can be seen in Fig. 29, very little vertical thermophoresis can be detected the second time.

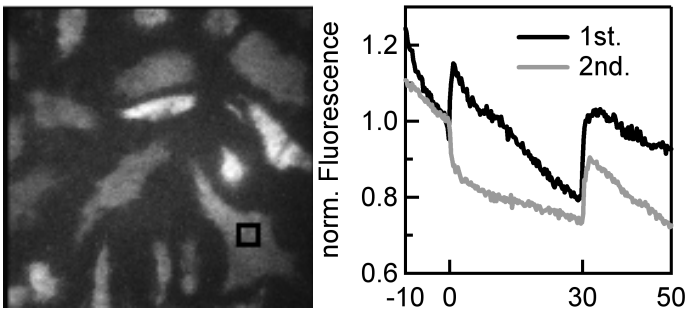

Figure 29: When the cell is repeatedly heated, it does not always show vertical thermophoresis.

The assumption is that the decrease of the second thermophoresis is due to a cell reaction, triggered by the high temperature increase. In the future, it would be interesting to perform more measurements and examine, whether there is a threshold for the temperature, and whether it reduces with more time between the measurements.

15.3 Intracellular Thermophoresis

It is important that the temperature spot is wide. Otherwise cells not directly above the heating center will experience a horizontal component of thermophoresis. After the initial fluorescence increase, traces on one side of these cells will show further increase, and traces from the other side will show a decrease (see Fig. 30). In a finite element simulation we simulated two cells, one directly above the temperature spot and one 50 µm to the side. We simulated the temperature distribution, the concentration distribution of the fluorophore in the cells and the time traces of the fluorophore concentration in different positions at the cover slip, which represents the brightness in the TIRF measurements (Fig. 30). The heat spot was moderately wide (HWHM=150 µm), so the temperature gradient is only slightly angled. The two-dimensional simulation included diffusion with the diffusion coefficient $D = 50$ µm²/s, thermophoresis with the thermodiffusion coefficient $D_T = 5$ µm²/(sK), heat conduction, and a Lorentzian temperature profile in the chromium layer with a peak temperature increase of $\Delta T_{max} = 5$ K and width $w = 150$ µm.

Furthermore, the analysis of the cell traces is not as straightforward as without cells. Extracellular traces from one spot can be evaluated in the steady state by the simple equation

$$\frac{c}{c_o} = \exp\left(-S_T(T - T_0)\right) \tag{44}$$

with c and T the concentration and temperature in the steady state with heating and c_0 and T_0 the values in the bulk or the initial values. Since the spot in the cell is not diffusively connected to a bulk reservoir, the size and shape of the cell has to be taken into account (see the cell model section 13.4). In contrast, it is possible to take two points inside one cell and compare their concentrations in the steady state. Since the image of a real cell does not have the same intensity everywhere, we calculate for every pixel the change in intensity during the heating, normalized by the initial intensity right after the IR laser was turned on. The result can be seen in Fig. 31. It is interesting how the two cells in the image behave differently and the cellular structure emerges with the cell nucleus. The thermophoresis corresponds to the cell thickness at each point with thicker parts being brighter.

15.4 Size Dependence

In measurements with pure BCECF or Cy 5 in aqueous solutions we could not observe thermophoresis, because the molecules diffuse too fast and the temperature equilibration cannot be distinguished from the upward thermophoretic movement. So only the slower, lateral movement was seen and TIRF and LED illumination yielded the same result (see Fig. 32. Thus, we switched to larger molecules for our in vitro measurements: long double stranded DNA of several kilo base pairs (see section 14.3), or large polystyrene beads of 20 nm up to 2 µm diameter (see Fig. 33 and section 14.2). Fig. 33 also shows that the TIRF system was working when the BCECF measurements were taken, since we could detect axial thermophoresis for the beads.

Thus, we looked for a cell system with large fluorescent molecules diffusing in the cytoplasm. In Fig. 34 we show thermophoresis measurements of cells, which had a green fluorescent ribosomal protein. However, the diffusion constant for such big objects is greatly reduced in the cytoplasm (compare the measured diffusion constants in section 15.1), so even in the prolonged heating time of 3 min we could not detect thermophoresis. Additionally, bleaching was strong, since the dye concentration was smaller compared to the other cell experiments in Fig. 28. There we could load the cells with high dye concentrations, whereas the cells here only expressed the labeled protein at normal level.

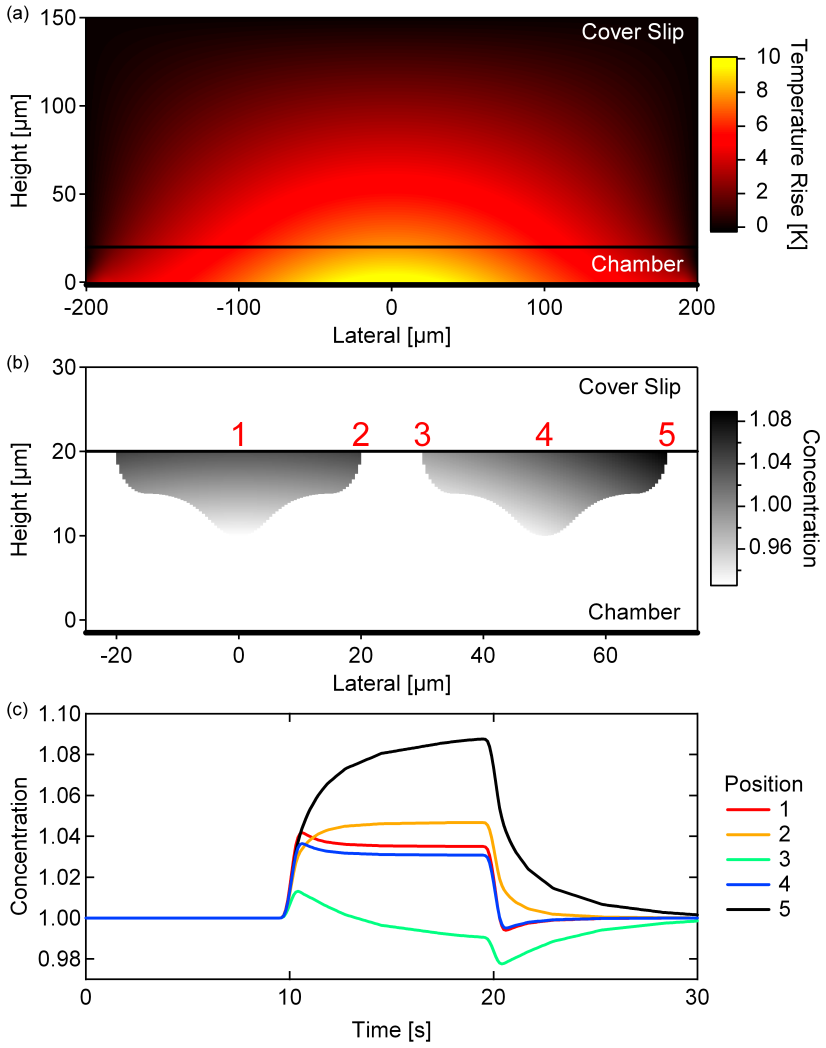

Figure 30: (a) Temperature simulation in a 10 µm high chamber, with a heating width of 150 µm for an only slightly angled temperature gradient. (b) Concentration simulation with one cell directly above the heating center and one cell 50 µm to the side. Positions where the time traces are shown are numbered. (c) Time traces at the different positions first show an increase for axial thermophoresis and later a further increase or a decrease according to lateral thermophoresis.

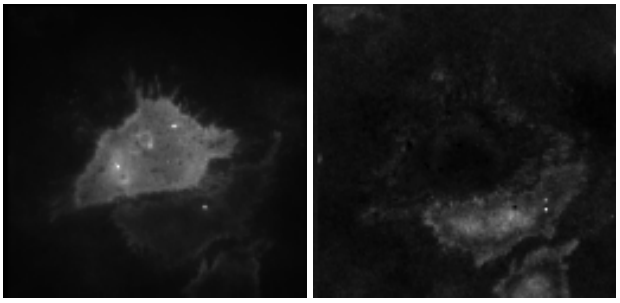

Figure 31: On the left the normal fluorescence image of the cells under TIRF illumination is shown, on the right the normalized change in fluorescence during the heating.

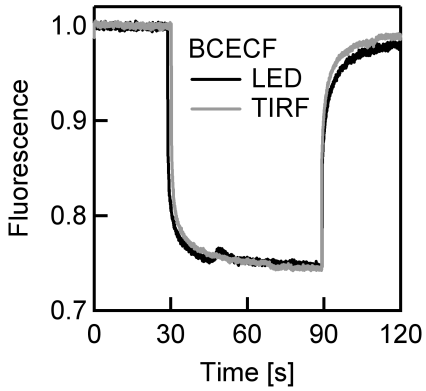

Figure 32: In diluted aqueous solutions the diffusion of the small fluorophore is too fast to resolve vertical thermophoresis before lateral thermophoresis sets in.

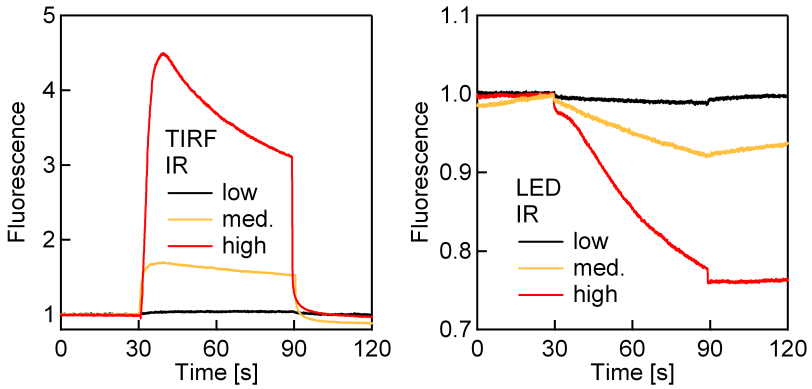

Figure 33: Axial thermophoresis is measured qualitatively in different IR laser powers, i.e. different temperature gradients.

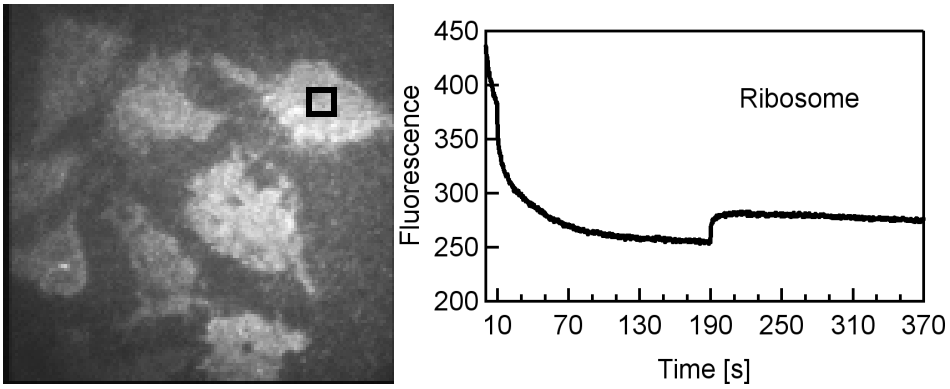

Figure 34: Measurements of green ribosomes only show bleaching, but no thermophoretic movement, since they are too big to diffuse in the crowded cell even during this prolonged measurement time of three minutes heating.

16 Conclusion

In this second part of the thesis a new geometry is proposed for thermophoresis measurements inside living cells. We have developed a TIRF-based measurement geometry, which allows to perform thermophoresis measurements with two-dimensional resolution on the micrometer scale. In this new geometry, we detect vertical thermophoresis, when the molecules are accumulated at the top cover slip. The results are compared with known epi-fluorescence measurements in the lateral geometry, which is known for example from the first part of this thesis. We measure different lengths of long double stranded DNA in different temperature gradients with TIRF and epi-LED illumination. We show that the physical processes involved in this new geometry can be quantitatively understood. Furthermore, we present for the first time thermophoresis measurements of fluorescent dyes and DNA inside living cells, acquired with the vertical thermophoresis setting. These measurements represent the first step towards *in vivo* binding studies. Biomolecular binding studies are already conducted in cell lysate [28] using Microscale Thermophoresis. This horizontal geometry of Microscale Thermophoresis [20, 28] had to be adapted to cell cultures in central parts. With the new method, binding measurements will soon also be possible in living cells.

Part III
Appendix

17 Abbreviations

17.1 Mathematical Symbols

α	temperature dependence of the fluorophore	%/K
c	concentration	M or mol/l
c_0	bulk concentration	M or mol/l
c_i	concentration of i-th ion species	M or mol/l
c_{PEG}	concentration of PEG molecule	M or mol/l
∇c	concentration gradient vector	M/m
D	mass diffusion coefficient	m²/s
D_T	thermo-diffusion coefficient	m²/sK
e	elementary charge	1.602 x10^{-19} As
end	time, when the IR laser is turned off	s
$\vec{E}$	electric field vector	V/m
ε	dielectric permittivity	As/Vm
ε_r	relative dielectric constant	As/Vm
ε_0	vacuum permittivity	8.854 x10^{-12} As/Vm
$flc2hs$	smoothed Heaviside function of FEMLAB	function
F	fluorescence	a.u.
F_{sed}	sedimentational force	
h	chamber height	m
H	heat equilibration time	s
g_0	gravitational acceleration	9.81 m/s²
$\vec{j}$	particle flux vector	mol/s
k	Boltzmann constant	1.381 x10^{-23} J/K
$k_{offTIRF}$	bleaching off-rate with TIRF illumination	%/s
k_{offLED}	bleaching off-rate with LED illumination	%/s
k_{off} or k_{bleach}	bleaching off-rate generally	%/s
L	length of the cylinder in the molecule	m
λ	penetration depth of TIRF field	m
λ_{DH}	Debye-Hückel screening length	m
μ	electric mobility	m²/Vs
N_A	Avogadro constant	6.022 x10^{23} 1/mol
η	dynamic viscosity	Pa s
Pe	Péclet number	number
Q	electric charge	e
$Q_{Zylinder}$	electric charge of the cylinder	e

Q_{Sphere}	electric charge of the sphere	e
$Q_{per\,Base}$	charge per base or per base pair for single stranded or double stranded DNA / RNA, respectively	e
r	radial coordinate	m
R	radius, or reaction rate to model bleaching (depending on context)	m or 1/s
R_{bead}	radius of the bead	m
R_{PEG}	radius of the crowding agend PEG	m
ρ	thermal expansivity of the water or fluid, or mass density of water (depending on context)	1/K or kg/m³
$\Delta\rho$	mass density difference of dye soaked beads to water	kg/m³
$start$	time, when the IR laser is turned on	s
S_T	Soret coefficient	1/K
S_T^{CM}	capacitor model contribution to the Soret coefficient	1/K
S_T^{NI}	non-ionic part of the Soret coefficient	1/K
S_T^{PEG}	Soret coefficient of the crowding agent PEG	1/K
S_T^{SE}	Seebeck contribution to the Soret coefficient	1/K
S_T^{∞}	fitting parameter - amplitude of the change in the Soret coefficient	1/K
ΔS_T	change in the Soret coefficient	1/K
$< S_T >$	average Soret coefficient of the two salt ions	1/K
t	time	s
T	absolute temperature	K
T_0	fitting parameter	K
T^*	fitting parameter - temperature, where S_T^{NI} changes sign	K
$T\,jump$	temperature sensitivity of the dye $= \alpha\Delta T$	K
ΔT	temperature difference or temperature increase	K
ΔT_{Cell}	temperature increase in the cell	K
ΔT_{max}	peak temperature	K
∇T	temperature gradient vector	K/m
$\nabla T^{'}$	temperature gradient modulated with the fact if the IR laser is turned on (vector)	K/m
$\vec{v}_{sed}$	sedimentation velocity vector	m/s
$\vec{v}_T$	thermophoretic velocity vector	m/s
$\vec{v}_T^{\prime}$	thermophoretic velocity modulated with the fact if the IR laser is turned on (vector)	m/s
w	HWHM width of the Lorentzian heating spot	m
W	electric work or energy stored in the capacitor	J

x or z	vertical coordinate	m
z_i	electric charge number of the i-th ion species in multiples of e	number
Z_{eff}	effective charge number of the molecule in multiples of e	number
$[\ldots]$	concentration of the molecule within	M or mol/l

17.2 Abbreviations

BCECF	2',7'-Bis-(2-carboxyethyl)-5-(and-6)-carboxyfluorescein
BCECF-AM	2',7'-Bis-(2-carboxyethyl)-5-(and-6)-carboxyfluorescein acetoxymethyl ester
bp or kbp	base pairs or kilo base pairs (unit)
BSA	bovine serum albumin
CCD	charge-coupled device
Cy 5	fluorescent cyanine dye 3H-Indolium
DNA	deoxyribonucleic acid
dsDNA	double stranded deoxyribonucleic acid
dsRNA	double stranded ribonucleic acid
ELISA	enzyme-linked immunosorbent assay
FCS	fetal calf serum
Hex or 6-Hex	6-carboxy-2 ,4,4 ,5 ,7,7 -hexachlorofluorescein
HWHM	half width half maximum of the heat Lorentzian spot is equal to the w
IR	infra-red
LED	light-emitting diode
MST	Microscale Thermophoresis
NA	numerical aperture
PBS	phosphate buffered saline
PEG	polyethylene glycol
pKa	acid dissociation constant
RNA	ribonucleic acid
SPR	surface plasmon resonance
ssDNA	single stranded deoxyribonucleic acid
ssRNA	single stranded ribonucleic acid
TIRF	total internal reflection fluorescence
TOTO-1	Quinolinium based fluorescent dye
TRIS	tris(hydroxymethyl)aminomethane or 2-Amino-2-hydroxymethyl-propane-1,3-diol
1D, 2D, 3D	one-, two-, or three-dimensional
...mer	oligomer (here DNA / RNA) with ... bases
40x 100x	magnification of the objective

18 References

[1] Funk M, et al. (2009) Constant power optical tweezers with controllable torque. *Optics Letters* 34:139–141.

[2] Tiselius A (1937) A new apparatus for electrophoretic analysis of colloidal mixtures. *Transactions of the Faraday Society* 33:524–531.

[3] Ludwig C (1856) Diffusion zwischen ungleich erwärmten Orten gleich zusammengesetzter Lösung. *Sitzungsberichte der mathematisch-naturwissenschaftlichen Classe der Kaiserlichen Akademie der Wissenschaften* p 539.

[4] Soret C (1879) Sur l'etat d'équilibre que prend au point de vue de sa concentration une dissolution saline primetevement homogène dont deux parties sont portées a des températures différentes. *Archives de Geneve* 3:48.

[5] Snowdon PN, Turner JCR (1960) The Soret effect in some 0.01 normal aqueous electrolytes. *Transactions of the Faraday Society* 56:1409.

[6] Chan J, Popov JJ, Kolisnek-Kehl S, Leaist DG (2003) Soret coefficients for aqueous polyethylene glycol solutions and some tests of the segmental model of polymer thermal diffusion. *Journal of Solution Chemistry* 32:197–214.

[7] Putnam SA, Cahill DG, Wong GCL (2007) Temperature dependence of thermodiffusion in aqueous suspensions of charged nanoparticles. *Langmuir* 23:9221–9228.

[8] Piazza R, Guarino A (2002) Soret effect in interacting micellar solutions. *Physical Review Letters* 88:208302.

[9] Braibanti M, Vigolo D, Piazza R (2008) Does thermophoretic mobility depend on particle size? *Physical Review Letters* 100:108303.

[10] Vigolo D, Buzzaccaro S, Piazza R (2010) Thermophoresis and thermoelectricity in surfactant solutions. *Langmuir* 26:7792–7801.

[11] Iacopini S, Rusconi R, Piazza R (2006) The macromolecular tourist: Universal temperature dependence of thermal diffusion in aqueous colloidal suspensions. *The European Physical Journal E* 19:59–67.

[12] Köhler W (1993) Thermodiffusion in polymer solutions as observed by forced Rayleigh scattering. *The Journal of Chemical Physics* 98:660.

[13] Kishikawa Y, et al. (2012) Temperature dependence of thermal diffusion for aqueous solutions of monosaccharides, oligosaccharides, and polysaccharides. *Physical Chemistry Chemical Physics* 14:10147.

[14] Jung H, Gusev VE, Baek H, Wang Y, Diebold GJ (2011) Ludwig–Soret effect in a linear temperature field: Theory and experiments for steady state distributions. *Physics Letters A* 375:1917–1920.

[15] Jerabek-Willemsen M, et al. (2014) Microscale thermophoresis: Interaction analysis and beyond. *Journal of Molecular Structure* In Press.

[16] Braun D, Libchaber A (2002) Trapping of DNA by thermophoretic depletion and convection. *Physical Review Letters* 89:188103.

[17] Duhr S, Braun D (2006) Why molecules move along a temperature gradient. *Proceedings of the National Academy of Sciences* 103:19678–19682.

[18] Guo X (2012) Surface plasmon resonance based biosensor technique: a review. *Journal of Biophotonics* 5:483–501.

[19] Engvall E, Perlmann P (1971) Enzyme-linked immunosorbent assay (ELISA). Quantitative assay of immunoglobulin G. *Immunochemistry* 8:871–874.

[20] Baaske P, Wienken CJ, Reineck P, Duhr S, Braun D (2010) Optical thermophoresis for quantifying the buffer dependence of aptamer binding. *Angewandte Chemie International Edition* 49:2238–2241.

[21] Wienken CJ, Baaske P, Rothbauer U, Braun D, Duhr S (2010) Protein-binding assays in biological liquids using microscale thermophoresis. *Nature Communications* 1:100.

[22] Pollack SJ, et al. (2011) A comparative study of fragment screening methods on the p38α kinase: new methods, new insights. *Journal of Computer-Aided Molecular Design* 25:677–687.

[23] Corin K, et al. (2011) A robust and rapid method of producing soluble, stable, and functional G-protein coupled receptors. *PloS one* 6:e23036.

[24] Bhogaraju S, et al. (2013) Molecular basis of tubulin transport within the cilium by IFT74 and IFT81. *Science* 341:1009–1012.

[25] Xiong X, et al. (2013) Receptor binding by a ferret-transmissible H5 avian influenza virus. *Nature* 497:392–396.

[26] Seidel SAI, et al. (2012) Label-free microscale thermophoresis discriminates sites and affinity of protein-ligand binding. *Angewandte Chemie International Edition* 51:10656–10659.

[27] Lippok S, et al. (2012) Direct detection of antibody concentration and affinity in human serum using microscale thermophoresis. *Analytical Chemistry* 84:3523–3530.

[28] Seidel SAI, et al. (2013) Microscale thermophoresis quantifies biomolecular interactions under previously challenging conditions. *Methods* 59:301–315.

[29] Dhont JKG, Wiegand S, Duhr S, Braun D (2007) Thermodiffusion of charged colloids: single-particle diffusion. *Langmuir* 23:1674–1683.

[30] Herzog M (2012) Ph.D. thesis (Systems Biophysics, Physik Department, Ludwig-Maximilians-Universität München).

[31] Sim AYL, Lipfert J, Herschlag D, Doniach S (2012) Salt dependence of the radius of gyration and flexibility of single-stranded DNA in solution probed by small-angle x-ray scattering. *Physical Review E* 86:021901.

[32] Lide DR (2001) *CRC Handbook of Chemistry and Physics* (CRC Press), 82nd edition.

[33] Duhr S, Braun D (2006) Thermophoretic depletion follows Boltzmann distribution. *Physical Review Letters* 96:168301.

[34] Lipfert J, Doniach S, Das R, Herschlag D (2014) Understanding nucleic acid-ion interactions. *Annual Review of Biochemistry* In Press.

[35] O'Brien RW, White LR (1978) Electrophoretic mobility of a spherical colloidal particle. *Journal of the Chemical Society, Faraday Transactions 2* 74:1607.

[36] Hickey OA, Shendruk TN, Harden JL, Slater GW (2012) Simulations of free-solution electrophoresis of polyelectrolytes with a finite Debye length using the Debye-Hückel approximation. *Physical Review Letters* 109:098302.

[37] Haugland RP, Spence MTZ, Johnson ID, Basey A (2005) *The handbook: A guide to fluorescent probes and labeling technologies* (Invitrogen Corp.), 10th edition.

[38] Stellwagen E, Stellwagen NC (2002) Determining the electrophoretic mobility and translational diffusion coefficients of DNA molecules in free solution. *Electrophoresis* 23:2794–2803.

[39] Wang Z, Kriegs H, Buitenhuis J, Dhont JKG, Wiegand S (2013) Thermophoresis of charged colloidal rods. *Soft Matter* 9:8697.

[40] Allison SA, Mazur S (1998) Modeling the free solution electrophoretic mobility of short DNA fragments. *Biopolymers* 46:359–373.

[41] Stellwagen E, Lu, Stellwagen NC (2003) Unified description of electrophoresis and diffusion for DNA and other polyions. *Biochemistry* 42:11745–11750.

[42] Putnam SA, Cahill DG (2005) Transport of nanoscale latex spheres in a temperature gradient. *Langmuir* 21:5317–5323.

[43] Guthrie G, Wilson JN, Schomaker V (1949) Theory of the thermal diffusion of electrolytes in a Clusius column. *The Journal of Chemical Physics* 17:310.

[44] Würger A (2008) Transport in charged colloids driven by thermoelectricity. *Physical Review Letters* 101:108302.

[45] Takeyama N, Nakashima K (1988) Proportionality of intrinsic heat of transport to standard entropy of hydration for aqueous ions. *Journal of Solution Chemistry* 17:305–325.

[46] Petit CJ, Hwang MH, Lin JL (1986) The Soret effect in dilute aqueous alkaline earth and nickel chloride solutions at 25°C. *International Journal of Thermophysics* 7:687–697.

[47] Einstein A (1905) Über die von der molekularkinetischen Theorie der Wärme geforderte Bewegung von in ruhenden Flüssigkeiten suspendierten Teilchen. *Annalen der Physik* 322:549–560.

[48] Götz A (2012) Bachelor thesis (Systems Biophysics, Physik Department, Ludwig-Maximilians-Universität München).

[49] Dong Q, Stellwagen E, Stellwagen NC (2009) Monovalent cation binding in the minor groove of DNA A-tracts. *Biochemistry* 48:1047–1055.

[50] Stellwagen E, Dong Q, Stellwagen NC (2005) Monovalent cations affect the free solution mobility of DNA by perturbing the hydrogen-bonded structure of water. *Biopolymers* 78:62–68.

[51] Sundararaman R, Letchworth-Weaver K, Arias TA (2014) A recipe for free-energy functionals of polarizable molecular fluids. *The Journal of Chemical Physics* 140:144504.

[52] Dhont JKG (2004) Thermodiffusion of interacting colloids. I. A statistical thermodynamics approach. *Journal of Chemical Physics* 120:1632–1641.

[53] Dhont JKG (2004) Thermodiffusion of interacting colloids. II. A microscopic approach. *Journal of Chemical Physics* 120:1642–1653.

[54] Chatterjee S, et al. (2006) The chemical nature of the 2'-substituent in the pentose-sugar dictates the pseudoaromatic character of the nucleobase (pKa) in DNA/RNA. *Organic & Biomolecular Chemistry* 4:1675.

[55] Jiang HR, Wada H, Yoshinaga N, Sano M (2009) Manipulation of colloids by a nonequilibrium depletion force in a temperature gradient. *Physical Review Letters* 102:208301.

[56] Würger A (2010) Thermal non-equilibrium transport in colloids. *Reports on Progress in Physics* 73:126601.

[57] Maeda YT, Tlusty T, Libchaber A (2012) Effects of long DNA folding and small RNA stem-loop in thermophoresis. *Proceedings of the National Academy of Sciences* 109:17972–17977.

[58] Reineck P, Wienken CJ, Braun D (2010) Thermophoresis of single stranded DNA. *Electrophoresis* 31:279–286.

[59] Parola A, Piazza R (2004) Particle thermophoresis in liquids. *The European Physical Journal E* 15:255–263.

[60] Xie XS, Yu J, Yang WY (2006) Living cells as test tubes. *Science* 312:228–230.

[61] Weinert FM, Braun D (2008) Observation of slip flow in thermophoresis. *Physical Review Letters* 101:168301.

[62] Kolber MA, Quinones RR, Gress RE, Henkert PA (1988) Measurement of cytotoxicity by target cell release and retention of the fluorescent dye bis-carboxyethyl-carboxyfluorescein (BCECF). *Journal of Immunological Methods* 108:255–264.

[63] Leeder J, Dosch HM, Harper P, Lam P, Spielberg S (1989) Fluorescence-based viability assay for studies of reactive drug intermediates. *Analytical Biochemistry* 177:364–372.

[64] Ellis R (2001) Macromolecular crowding: obvious but underappreciated. *Trends in Biochemical Sciences* 26:597–604.

[65] Passvogel S (2011) Bachelor thesis (Systems Biophysics, Physik Department, Ludwig-Maximilians-Universität München).

[66] Pluen A, Netti PA, Jain RK, Berk DA (1999) Diffusion of macromolecules in agarose gels: Comparison of linear and globular configurations. *Biophysical Journal* 77:542–552.

[67] Kao HP, Abney JR, Verkman A (1993) Determinants of the translational mobility of a small solute in cell cytoplasm. *The Journal of Cell Biology* 120:175–184.

[68] Dauty E, Verkman AS (2005) Actin cytoskeleton as the principal determinant of size-dependent DNA mobility in cytoplasm: A new barrier for non-viral gene delivery. *Journal of Biological Chemistry* 280:7823–7828.

[69] Lukacs GL, et al. (2000) Size-dependent DNA mobility in cytoplasm and nucleus. *Journal of Biological Chemistry* 275:1625–1629.

[70] Reichl M, Herzog M, Götz A, Braun D (2014) Why charged molecules move across a temperature gradient: The role of electric fields. *Physical Review Letters* 112:198101.

Acknowledgments

This work would not have been possible without the work, help, support and advice of supervisors, colleagues, friends, and family. All achievements described in this dissertation I owe to them, any errors and omissions are my own.

Dieter Braun: He taught me how to become a scientist. Thank you! Also thanks for being available just across the desk.

To my Bachelor students Alexandra Götz and Stefan Passvogel: Thank you for your work, help, and ten weeks of good collaboration each. It was a pleasure to work with you.

All Braunies (approximately in order of appearance): Christof Mast, who knows all about everything and shares it if he's not occupied by others; Mario Herzog, from whom I inherited many projects, some of them still unfinished... Hubert Krammer for the introduction to unCeNSiert and his view on things in life; Natan Osterman, your optimism helped me getting started; Manuel Wolff for discussions and working on related topics; Susanne Seidel, the chemist, biologist, insert what you need, and molecular medicine expert; Friederike Möller supporting the tea fraction; Simon Lanzmich for help with computer problems; Georg Urtel, Matthias Morasch and Lorenz Keil, with you the hours in the lab are never boring; Franziska Kriegl for your support. And thanks to all the others whom I forgot to mention. Thanks to the Gambies for the cell culture possibilities and the sophisticated chemistry lab.

Martin Benoit, Laura Kellermann, Hanna Engelke, Pablo Dominguez, Rainer Szalata, and all the others from unCeNSiert: Your music keeps me going!

Most of all to my family: Thank you for your help and for your belief that I can do this. Without you this thesis would never have started and it would never have finished.

19 Publications

[1] Reichl MR, Herzog M, Götz A, Braun D (2014) Why charged molecules move across a temperature gradient: The role of electric fields. *Physical Review Letters* 112:198101.

[2] Reichl MR, Braun D (submitted) Thermophoresis measurements in living cells using total internal reflection fluorescence microscopy. *Nature Physics*.

[3] Reichl MR, Herzog M, Braun D (submitted) Understanding the similar thermophoresis of single and double stranded DNA and RNA. *Nucleic Acids Research*.

Why Charged Molecules Move Across a Temperature Gradient: The Role of Electric Fields

Maren Reichl, Mario Herzog, Alexandra Götz, and Dieter Braun*
Systems Biophysics, Physics Department, Nanosystems Initiative Munich and Center for NanoScience Ludwig-Maximilians-Universität München, Amalienstrasse 54, 80799 München, Germany
(Received 6 February 2014; revised manuscript received 2 April 2014; published 13 May 2014)

Methods to move solvated molecules are rare. Apart from electric fields, only thermal gradients are effective enough to move molecules inside a fluid. This effect is termed thermophoresis, and the underlying mechanisms are still poorly understood. Nevertheless, it is successfully used to quantify biomolecule binding in complex liquids. Here we show experiments that reveal that thermophoresis in water is dominated by two electric fields, both established by the salt ions of the solution. A local field around the molecule drives molecules along an energy gradient, whereas a global field moves the molecules by a combined thermoelectrophoresis mechanism known as the Seebeck effect. Both mechanisms combined predict the thermophoresis of DNA and RNA polymers for a wide range of experimental parameters. For example, we correctly predict a complex, nonlinear size transition, a salt-species-dependent offset, a maximum of thermophoresis over temperature, and the dependence of thermophoresis on the molecule concentration.

DOI: 10.1103/PhysRevLett.112.198101 PACS numbers: 66.10.-x, 82.45.Gj, 82.60.Lf, 87.15.-v

Introduction.—Thermophoresis is the motion of molecules induced by a temperature gradient, often also referred to as the Soret effect, thermodiffusion, or thermal diffusion. Typically, the molecule concentration depletes at positions of locally enhanced temperature. The strength of depletion is parameterized by the Soret coefficient S_T [1,2] and given by $c = c_0 \exp[-S_T(T - T_0)]$ with the depleted concentration c at varying temperature T at a bulk concentration and temperature c_0 and T_0, respectively. Predictive models to calculate S_T based on molecule parameters are missing. Often, the nonequilibrium analogy between thermophoresis and electrophoresis is assumed while a local equilibrium considerations are not considered.

For the last 3 years, a growing number of biologists have used thermophoresis as a method [3,4] for quantifying biomolecule binding [5–10]. Also, central questions of molecular evolution were addressed by thermophoretic traps [11–13]. Despite the general interest in the topic, the above applications of thermophoresis are missing a solid theoretical foundation at the moment.

To approach the problem, systematic experiments over a large parameter space are required. Polymers in nonaqueous solutions show a clear scaling behavior with molecular weight [14] and isotope composition [15]. The mass dependence of thermophoresis in silica melts [16] suggested a quantum mechanical treatment [17,18]. Polystyrene beads and long double-stranded DNA of various size were studied [19,20], suggesting a plate capacitor model [21]. Size-dependent measurements of polystyrene beads at constant Debye length, however, disputed the results [22].

Here, single- and double-stranded DNA and RNA of different lengths were measured for various salt concentrations, salt species, and temperatures. The experiments test the size transition of the capacitor model, especially for Debye lengths larger than the molecule size. In addition, they probe a thermoelectric Seebeck contribution, suggested by experiments [23] and theoretical treatments [24,25]. Oligonucleotides offer a precise length definition, excellent purity, and fluorescence-based measurements at low concentrations. Many molecular parameters are known for oligonucleotides.

Theory.—In the following, thermophoresis is described with a combination of four molecular mechanisms, fully described in the Supplemental Material Sec. S1 [26]:

$$S_T = S_T^{CM} + S_T^{EL} + S_T^{NI} + 1/T \tag{1}$$

The capacitor model [21] described in Fig. 1(a) leads to

$$S_T^{CM}\frac{R}{Z_{\mathrm{eff}}^2} = \frac{e^2 R/\lambda_{DH}}{16\pi k_B T^2 \varepsilon_r \varepsilon_0 (1 + R/\lambda_{DH})^2} \times \left(1 - \frac{\partial \ln \rho(T)}{\partial \ln T} - \frac{\partial \ln \varepsilon_r(T)}{\partial \ln T}\left(1 + \frac{2\lambda_{DH}}{R}\right)\right). \tag{2}$$

As seen, the right-hand side only depends on constants and a rescaled Debye length λ_{DH}/R with the hydrodynamic molecule radius R. The Seebeck effect is visualized in Fig. 1(b) and is derived analogously to the monovalent salt cases [24,25]:

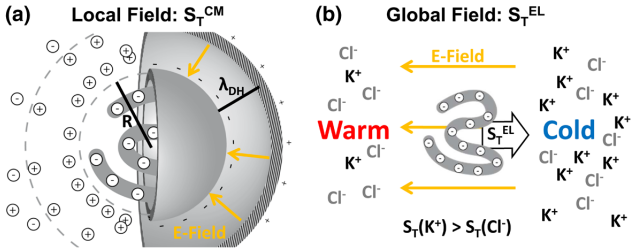

FIG. 1 (color online). Local and global electric fields move molecules along a temperature gradient. (a) Around a charged molecule, dissolved ions form a shielding capacitor with Debye length λ_{DH}. The energy stored in the capacitor decreases in the cold and leads to a positive Soret coefficient S_T^{CM}. For molecules with radius R smaller than the Debye length λ_{DH}, the radial capacitor can be approximated as a point charge; for larger molecules, it can be approximated as a plate capacitor. The result is a nonlinear size transition depending on λ_{DH}/R. (b) The differential Soret coefficients of ions in solution, here K^+ and Cl^-, create a global electric field. The resulting electrophoresis cannot be readily distinguished from thermophoresis. This Seebeck effect results in an ion-species-dependent offset S_T^{EL} that is independent of the Debye length for the used experimental conditions.

$$S_T^{EL} = -\frac{k_B T \mu_{DNA}}{e D_{DNA}} \frac{\sum_i z_i c_i S_{Ti}}{\sum_i z_i^2 c_i}. \tag{3}$$

Finally, the temperature dependence of nonionic contributions are fitted empirically [27] according to

$$S_T^{NI} = S_T^{\infty}\left[1 - \exp\left(\frac{T^* - T}{T_0}\right)\right] \tag{4}$$

The small contribution $1/T$ is based on the temperature dependence of the diffusion coefficient.

Results.—We first test the capacitor model contribution S_T^{CM}. Single-stranded DNA and RNA form a spherical coil due to their short persistence length. For elongated shapes, the dependence on λ_{DH} is expected to be very similar [28]. Inside the hydrodynamic radius R, adsorbed ions reduce the bare charge to the effective charge Z_{eff}. Toward the periphery, the molecule is shielded within the Debye length λ_{DH} created by the ions in solution [Fig. 1(a)]. Depending on the size ratio λ_{DH}/R, the capacitor can be approximated as a plate capacitor when $\lambda_{DH} \ll R$. This plate capacitor case was studied previously [29], and S_T^{CM} rises linearly with λ_{DH}. For the size regime $\lambda_{DH} \ll R$, the shielding capacitor becomes a point charge, and according Eq. (2), the Soret coefficient should saturate toward a constant value.

As shown in Fig. 2(a), the measurements confirm this nontrivial prediction of the capacitor model without the need to fit of the molecule or its effective charge. We measured single-stranded DNA with lengths of 2, 5, 10, 22, 50, and 80 bases. For short DNA, a transition of the measured Soret coefficients toward a constant value is

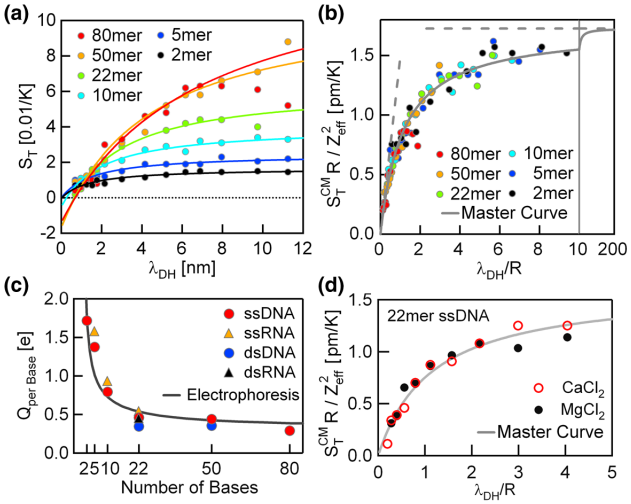

FIG. 2 (color online). Nonlinear size transition of capacitive thermophoresis. (a) The Soret coefficient S_T is measured for single-stranded DNA with lengths of 2, 5, 10, 22, 50, and 80 bases and plotted against Debye length λ_{DH} at 15°C. The radius R is measured from diffusion; the effective charge describes the amplitude, and a constant offset $S_T(\lambda_{DH} = 0) = S_T^{EL} + S_T^{NI} + 1/T$ is determined. (b) After rescaling the data according to Eq. (2), the measurements fall onto a single master curve and confirm in detail the size transition of the capacitor model. Broken lines denote the limiting cases for $\lambda_{DH} \ll R$ and $\lambda_{DH} \gg R$. (c) The effective charge per base fitted from the capacitor model decreases with increasing length. The number of bases is used as a measure of molecule length; thus, only half of the bases of the double stranded species is counted. It matches the effective charge known from electrophoresis shown as a solid line [32]. (d) Thermophoresis measurements using divalent salt ions equally follow the same capacitor model.

found at small λ_{DH}, whereas longer DNA first rises linearly and bends but does not fully saturate in the tested λ_{DH} regime. The data can be fitted by Eq. (2) with the hydrodynamic radius R measured through the diffusion coefficient (Supplemental Material S3 [26]). The amplitude of the curve is adjusted by the effective charge number Z_{eff} and later compared to the effective charge known from electrophoresis. Contributions from the capacitor model vanish for $\lambda_{DH} = 0$, and thermophoresis is given by $S_T^{EL} + S_T^{NI} + 1/T$, which does not depend on λ_{DH}. After subtracting this offset, the data are rescaled by Z_{eff}^2/R and plotted against a rescaled Debye-axis λ_{DH}/R with the measured radius R. All measurements fall onto the single master curve of the capacitor model Eq. (2) [Fig. 2(b)].

Initially, the effective charge number Z_{eff} is a fitting parameter of the capacitor model. To compare with electrophoresis, it is divided by the number of bases (or base pairs for the double stranded species) and plotted versus DNA length in Fig. 2(c). It decreases with DNA length. This effect is known for DNA from electrophoresis and attributed to Manning condensation [30–32]. A most recent model using multiparticle collision dynamics [33] is plotted

as a solid line. The effective charge from electrophoresis matches the effective charge determined from thermophoresis by the capacitor model remarkably well.

Very similar results are found for single-stranded RNA (Supplemental Material S3 [26]). As known from electrophoresis, the effective charge of double-stranded DNA or RNA does not differ much from their single-stranded versions [31]. The same is found for the charges determined from thermophoresis. The 80mer deviates for large λ_{DH}, marking the breakdown of the internal shielding approximation. To test the generality of the approach, we measured 22mer single-stranded DNA using the divalent salts $CaCl_2$ and $MgCl_2$ [Fig. 2(d)]. The Debye length includes now the different contributions from the used monovalent and divalent ion concentrations. As seen, the capacitor model equally describes the measurements for divalent ions. The effective charge per base is twofold smaller (0.2e per base), but a similar decrease of the electric mobility for higher valent salts is known [34]. Overall, the temperature dependence of the energy stored in the ionic shielding describes the salt-concentration-dependent contribution in thermophoresis remarkably well.

Since the pioneering salt-species-dependent measurement of Putnam and Cahill [23], a contribution to thermophoresis from the Seebeck effect was suspected but not demonstrated without fitting parameters. Salt ions follow a differential thermophoretic pattern, create an electric field, and move molecules by electrophoresis. Under our experimental conditions, we expect that this thermoelectric effect leads to a salt-species-dependent but salt-concentration-independent offset of the capacitor model (Supplemental Material S5 [26]). Neither the large Soret coefficient of OH^-, H_3O^+ nor the highly charged DNA itself contributes significantly as the millimolar salt concentrations dominate the sums in Eq. (3).

The measurement of negatively charged 2mer, 22mer, and 80mer single-stranded DNA and of positively charge rhodamine 6G for varying concentrations of KBr, KCl, KF, KI, NaBr, NaCl, NaF, NaI, LiBr, LiCl, and LiI is shown in the Supplement Material S5 [26]. The dependence of S_T on the Debye length can be fully described by the capacitor model, but an additional offset of the Soret coefficient is found that depends on the salt species. In Fig. 3(a), we compare the offset minus $1/T$ minus a constant S_T^{NI} to the Seebeck theory using published Soret coefficients of the salt species [36,37]. A very convincing match between the measured S_T^{EL} and the theoretical Seebeck effect is found.

We check the model internally by comparing the charge of the capacitor model [Fig. 2(c)] with the charge derived from the Seebeck effect. The electric mobility is fitted from the differential thermophoresis and reveals $\mu_{DNA} = -1.2 \pm 0.13$, -2.6 ± 0.24, and $-1.2 \pm 0.13 \times 10^{-8}$ m^2/Vs for the 2mer, 22mer, and 80mer, consistent with literature values (see the Supplemental Material S5 [26]). Note that the Seebeck effect depends on the sign

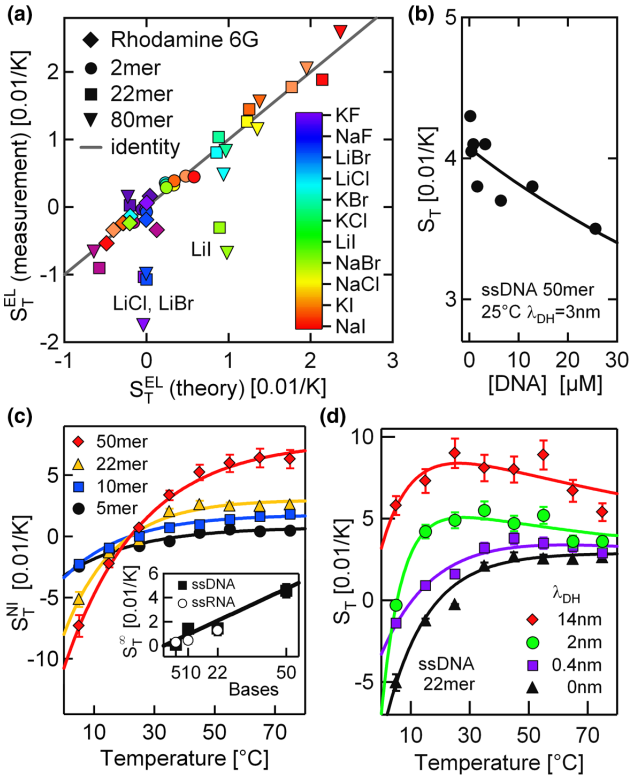

FIG. 3 (color online). Seebeck contribution and dependence on concentration and temperature. (a) The Seebeck contribution S_T^{EL} is extracted from salt-species-dependent measurements (Supplemental Material S5 [26]) by extrapolating to $\lambda_{DH} = 0$, subtracting $1/T$, and removing the nonionic, molecule-specific contribution S_T^{NI} according to Eq. (1). The theoretical Seebeck contribution [Eq. (3)] matches the experimental S_T^{EL} for positively charged rhodamine 6G and negatively charged 2mer, 22mer, and 80mer ssDNA, with small deviations of lithium salts for 22mer and 80mer. (b) The DNA concentration dependence of thermophoresis matches the prediction based on the Seebeck effect. (c) After subtracting S_T^{CM}, S_T^{EL}, and $1/T$ from the measurements, the remaining nonionic contribution S_T^{NI} matches the empirical Eq. (4) proposed by Piazza [35]. Its magnitude S_T^∞ scales linearly with DNA length (inset). (d) Ionic thermophoresis decreases with temperature [Eq. (2)] but increases with the nonionic contribution [Eq. (4)]. Their combination directly explains the nontrivial maximum of thermophoresis at intermediate temperatures.

of the charge, in contrast to S_T^{CM}. As predicted, measurements of the positively charged dye rhodamine 6G invert the order of the salt species.

Interestingly, the measured DNA concentration dependence of thermophoresis [Fig. 3(b)] can be fully explained by the Seebeck effect and the capacitor model (Supplemental Material S6 [26]). The oligonucleotide charge does not change between the two relevant pK_a values of oligonucleotides above 4.3 or below 8.7 [38]. In confirmation of the model, the Soret coefficient of DNA is constant within a pH of 5–9 (Supplemental Material S4 [26]). Outside this pH range, thermophoresis drops

as expected from the reduced nucleotide charge. This also supports the theoretically expected negligible contribution to the Seebeck effect from OH^- and H_3O^+ ions (Supplemental Material S5 [26]). While OH^- and H_3O^+ ions have large Soret coefficients, their micromolar concentration near neutral pH cannot compete against the millimolar salt concentrations in Eq. (3). These results do not contradict reports measuring without buffer at high pH [39]. On the same grounds, a possible constant Seebeck contribution from the unknown Soret coefficient of the TRIS buffer was neglected.

After subtracting the Seebeck effect S_T^{EL}, subtracting the ideal gas contribution $1/T$, and extrapolating the capacitor model S_T^{CM} toward $\lambda_{DH} \to 0$, we are left with the nonionic contribution S_T^{NI} [Eq. (1)]. As seen in Fig. 3(c), the measured S_T^{NI} rises characteristically over temperature and can be fitted with the empirical Eq. (4). As shown in the inset, the nonionic amplitude S_T^{∞} shows a linear dependence on DNA (or RNA) length as expected for a local, molecule-solvent interaction across the area of a thin tube around the polymer.

The temperature dependence of thermophoresis in Fig. 3(d) shows a maximum that is increasingly prominent for increasing Debye length. This nontrivial dependence is readily described by Eq. (1). Since the condensed charges do not depend significantly on temperature, S_T^{CM} decreases as the temperature increases according to Eq. (2). The nonionic contribution S_T^{NI} rises over the temperature [Eq. (4)]. The small Seebeck term S_T^{EL} is largely temperature independent. Without additional parameters, the measurements are fully described [Fig. 3(d), lines]. As shown in the Supplemental Material S7 [26], two-dimensional measurements over Debye length and temperature are fully predicted by Eq. (1).

Discussion.—Our analysis of the experiments suggests that a thermodynamic approach is valid for thermophoresis. The total energy of a molecule differs along a thermal gradient, in contrast to electrophoresis where the fully shielded molecule shows no potential energy difference in an electric field. Typical for thermophoresis and including our measurements, depleted concentrations never drop below 50% of the bulk concentration. The diffusion back into the heated region can be achieved by thermodynamic fluctuations over the time of the experiment. The Peclet number (Pe) of the molecules, also termed the Brenner number, is smaller than one even for the largest 80mer ssDNA used in this work, $Pe = RS_T\nabla T = 10\ \text{nm} \times 0.0001\ \text{K}^{-1} \times 5\ \text{K}/50\ \mu\text{m} = 10^{-4}$, documenting the diffusion-dominated molecule motion. All of the above substantiate a local equilibrium approach to thermophoresis. Fluorescence imaging allows us to measure at a 1-μM molecule concentration, more than 3 orders of magnitude smaller than the overlap concentration c^*. The average molecule distance is 120 nm, more than tenfold larger than the diameter of the largest measured molecule. Therefore, we do not include concentration-dependent effects in Eq. (1) [40,41].

Understanding thermophoresis on a molecular level is highly beneficial to use thermophoresis in biomolecular binding studies [3–10,42]. Using the successful model of thermophoresis, the changes of S_T upon molecule binding can be quantitatively predicted. Also, since the electrophoretic mobility is measured all optically by measuring thermophoresis for different salt species [Fig. 3(a)], direct inference on the sign and magnitude of a charged molecule becomes possible.

We thank Philipp Reineck, Christoph Wienken, and Christian Speck for initial measurements and Philipp Baaske, Lorenz Keil, Christof Mast, and Manuel Wolff for help with the measurement setup. For discussions, we appreciate comments from Jan Dhont, Simone Wiegand, Christof Mast, Shoichi Toyabe, Moritz Kreysing, Jan Lipfert, and Dean Astumian. Financial support from the Nanosystems Initiative Munich, the LMU Initiative Functional Nanosystems, and the ERC Starting Grant is gratefully acknowledged. All authors contributed extensively to the work presented in this paper.

*Corresponding author.
dieter.braun@lmu.de

[1] C. Ludwig, *Diffusion Zwischen Ungleich Erwärmten Orten Gleich Zusammengesetzter Lösung* (Akademie der Wissenschaften, Wien, 1856).
[2] C. Soret, Arch. Geneve 3 **48** (1879).
[3] P. Baaske, C. J. Wienken, P. Reineck, S. Duhr, and D. Braun, Angew. Chem., Int. Ed. Engl. **49**, 2238 (2010).
[4] C. J. Wienken, P. Baaske, U. Rothbauer, D. Braun, and S. Duhr, Nat. Commun. **1**, 100 (2010).
[5] S. Bhogaraju *et al.*, Science **341**, 1009 (2013).
[6] X. Xiong *et al.*, Nature (London) **497**, 392 (2013).
[7] X. Shang, F. Marchioni, C. R. Evelyn, N. Sipes, X. Zhou, W. Seibel, M. Wortman, and Y. Zheng, Proc. Natl. Acad. Sci. U.S.A. **110**, 3155 (2013).
[8] C. G. Alexander, M. C. Jurgens, D. A. Shepherd, S. M. V. Freund, A. E. Ashcroft, and N. Ferguson, Proc. Natl. Acad. Sci. U.S.A. **110**, E2782 (2013).
[9] M. Gertz, F. Fischer, G. T. T. Nguyen, M. Lakshminarasimhan, M. Schutkowski, M. Weyand, and C. Steegborn, Proc. Natl. Acad. Sci. U.S.A. **110**, E2772 (2013).
[10] T. Cherrier *et al.*, Proc. Natl. Acad. Sci. U.S.A. **110**, 12 655 (2013).
[11] P. Baaske, F. M. Weinert, S. Duhr, K. H. Lemke, M. J. Russell, and D. Braun, Proc. Natl. Acad. Sci. U.S.A. **104**, 9346 (2007).
[12] C. B. Mast and D. Braun, Phys. Rev. Lett. **104**, 188102 (2010).
[13] C. B. Mast, S. Schink, U. Gerland, and D. Braun, Proc. Natl. Acad. Sci. U.S.A. **110**, 8030 (2013).
[14] D. Stadelmaier and W. Köhler, Macromolecules **42**, 9147 (2009).

[15] G. Wittko and W. Köhler, J. Chem. Phys. **123**, 014506 (2005).
[16] F. Huang, P. Chakraborty, C. C. Lundstrom, C. Holmden, J. J. G. Glessner, S. W. Kieffer, and C. E. Lesher, Nature (London) **464**, 396 (2010).
[17] G. Dominguez, G. Wilkins, and M. H. Thiemens, Nature (London) **473**, 70 (2011).
[18] S. Hartmann, W. Köhler, and K. I. Morozov, Soft Matter **8**, 1355 (2012).
[19] S. Duhr and D. Braun, Proc. Natl. Acad. Sci. U.S.A. **103**, 19 678 (2006).
[20] P. Reineck, C. J. Wienken, and D. Braun, Electrophoresis **31**, 279 (2010).
[21] J. K. G. Dhont, S. Wiegand, S. Duhr, and D. Braun, Langmuir **23**, 1674 (2007).
[22] M. Braibanti, D. Vigolo, and R. Piazza, Phys. Rev. Lett. **100**, 108303 (2008).
[23] S. A. Putnam and D. G. Cahill, Langmuir **21**, 5317 (2005).
[24] G. Guthrie, J. N. Wilson, and V. Schomaker, J. Chem. Phys. **17**, 310 (1949).
[25] A. Würger, Phys. Rev. Lett. **101**, 108302 (2008).
[26] See Supplemental Material at http://link.aps.org/supplemental/10.1103/PhysRevLett.112.198101 for more information on calculations, simulations, measurements and discussion details.
[27] S. Iacopini, R. Rusconi, and R. Piazza, Eur. Phys. J. E **19**, 59 (2006).
[28] Z. Wang, H. Kriegs, J. Buitenhuis, J. K. G. Dhont, and S. Wiegand, Soft Matter **9**, 8697 (2013).
[29] S. Duhr and D. Braun, Phys. Rev. Lett. **96**, 168301 (2006).
[30] D. A. Hoagland, E. Arvanitidou, and C. Welch, Macromolecules **32**, 6180 (1999).
[31] E. Stellwagen, Y. Lu, and N. C. Stellwagen, Biochemistry **42**, 11 745 (2003).
[32] K. Grass, U. Böhme, U. Scheler, H. Cottet, and C. Holm, Phys. Rev. Lett. **100**, 096104 (2008).
[33] O. A. Hickey, T. N. Shendruk, J. L. Harden, and G. W. Slater, Phys. Rev. Lett. **109**, 098302 (2012).
[34] R. W. O'Brien and L. R. White, J. Chem. Soc., Faraday Trans. 2 **74**, 1607 (1978).
[35] S. Iacopini and R. Piazza, Europhys. Lett. **63**, 247 (2003).
[36] N. Takeyama and K. Nakashima, J. Solution Chem. **17**, 305 (1988).
[37] C. J. Petit, M.-H. Hwang, and J.-L. Lin, Int. J. Thermophys. **7**, 687 (1986).
[38] S. Chatterjee, W. Pathmasiri, O. Plashkevych, D. Honcharenko, O. P. Varghese, M. Maiti, and J. Chattopadhyaya, Org. Biomol. Chem. **4**, 1675 (2006).
[39] D. Vigolo, S. Buzzaccaro, and R. Piazza, Langmuir **26**, 7792 (2010).
[40] Y. T. Maeda, T. Tlusty, and A. Libchaber, Proc. Natl. Acad. Sci. U.S.A. **109**, 17 972 (2012).
[41] H.-R. Jiang, H. Wada, N. Yoshinaga, and M. Sano, Phys. Rev. Lett. **102**, 208301 (2009).
[42] S. Lippok, S. A. I. Seidel, S. Duhr, K. Uhland, H.-P. Holthoff, D. Jenne, and D. Braun, Anal. Chem. **84**, 3523 (2012).

Supporting Online Information

Why charged molecules move across a temperature gradient

Maren Reichl, Mario Herzog, Alexandra Götz and Dieter Braun

S1 Theory

Capacitor Model. In this model, the energy inside the Debye screening drives thermophoresis (*1, 2*). A spherically approximated molecule with effective charge number Z_{eff} is shielded by the ions of the solution. The shielding potential decays with the Debye length

$$\lambda_{DH} = \sqrt{\varepsilon(T) k_B T / \left(N_A e^2 \sum_i c_i z_i^2 \right)}$$

where N_A denotes the Avogadro constant, e the elementary charge, c_i the concentration, z_i the charge number of the i-th ion type, k_B the Boltzmann constant, T the absolute temperature, $\varepsilon(T) = \varepsilon_r(T)\, \varepsilon_0$, with $\varepsilon_r(T)$ the relative permittivity of the solvent and ε_0 the vacuum permittivity. The Debye length increases with decreasing salt concentration and decreases with temperature. The detailed theoretical argument (*2*) can be abbreviated as follows. Let us consider the diffusive shielding as a spherical capacitor with the hydrodynamic radius R of the molecule and the distance between the plates given by the temperature dependent Debye length $\lambda_{DH}(T)$ (Fig. 1a). Under low thermophoretic depletion and small Peclet numbers, we can use a local equilibrium approach and interpret the steady state thermophoretic depletion $c = c_0 \exp\left[-S_T (T - T_0)\right]$ as a Boltzmann distribution (*1–3*) with index *0* indicating the bulk properties. As described by (*2*) the capacitor model contribution to the Soret coefficient S_T^{CM} can be derived from the electric energy W stored in the spherical capacitor:

$$S_T^{CM} = \frac{1}{k_B T} \frac{\partial W}{\partial T}$$

$$W = \frac{{Q_{eff}}^2}{8\pi\varepsilon R\left(R/\lambda_{DH} + 1\right)}$$

In the case of DNA in an aqueous salt solutions, the effective charge $Q_{eff} = Z_{eff}\, e$ does not significantly depend on the temperature. Also to a good approximation, we found that the hydrodynamic radius R does not depend on temperature. However, the permittivity of water depends on the temperature (*4*). In addition to the equation of Dhont one could include the thermal expansion of water, which when heated dilutes the sample concentration c with the density of water ρ (*4*). The Debye length then requires to be differentiated with respect to the temperature:

$$\frac{\partial \lambda_{DH}}{\partial T} = \frac{\lambda_{DH}}{2}\left(\frac{1}{T} - \frac{1}{\sum_i c_i z_i^2} \frac{\partial \sum_i c_i z_i^2}{\partial T} + \frac{1}{\varepsilon}\frac{\partial \varepsilon}{\partial T} \right)$$

$$S_T^{CM} = \frac{Q^2}{k_B T^2 16\pi\varepsilon\lambda_{DH}\left(R/\lambda_{DH}+1\right)^2}\left[1 - \frac{T}{\sum_i c_i z_i^2}\frac{\partial \sum_i c_i z_i^2}{\partial T} + \frac{T}{\varepsilon}\frac{\partial \varepsilon}{\partial T} - \frac{T}{\varepsilon}\left(2 + \frac{2\lambda_{DH}}{R}\right)\frac{\partial \varepsilon}{\partial T} \right]$$

$$S_T^{CM} = \frac{\left(Z_{eff}\, e\right)^2}{k_B T^2 16\pi\varepsilon\lambda_{DH}\left(R/\lambda_{DH}+1\right)^2}\left[1 - \frac{\partial \ln \rho}{\partial \ln T} - \frac{\partial \ln \varepsilon}{\partial \ln T}\left(1 + \frac{2\lambda_{DH}}{R}\right) \right]$$

Here, Z_{eff} denotes the effective charge number of the probed molecule in units of e. The hydrodynamic radius R of the molecule is determined using the measured diffusion coefficient D. However, the temperature expansion of water can be omitted, since its influence on S_T^{CM} in our temperature range is small. At its maximum for $\lambda_{DH} = 0$ (infinitely high salt concentration) and 75 °C it contributes only 8.3% with $\frac{\partial \ln \rho}{\partial \ln T} = -0.21$ and $\frac{\partial \ln \varepsilon}{\partial \ln T} = -1.6$.

By rescaling the Debye length with particle radius R and the Soret coefficient with R and Z_{eff}^2, we obtain a molecule independent master curve of thermophoresis based on the capacitor model:

$$S_T^{CM}\,\frac{R}{Z_{eff}^2} = \frac{e^2 R/\lambda_{DH}}{16\pi k_B T^2 \varepsilon_r \varepsilon_0 \left(1 + R/\lambda_{DH}\right)^2}\left[1 - \frac{\partial ln\rho(T)}{\partial lnT} - \frac{\partial ln\varepsilon_r(T)}{\partial lnT}\left(1 + \frac{2\lambda_{DH}}{R}\right) \right]$$

To better understand the size transition, let us consider the cases $\lambda_{DH}/R \to 0$ and $\lambda_{DH}/R \to \infty$: For vanishing Debye length the spherical capacitor behaves like a parallel plate capacitor and the Soret coefficient increases linearly with the Debye length λ_{DH} (*5, 6*).

$$\lim_{\lambda_{DH}\to 0} S_T^{CM}\,\frac{R}{Z_{eff}^2} = \frac{e^2\,\lambda_{DH}/R}{16\pi k_B T^2 \varepsilon_r \varepsilon_0}\left(1 - \frac{\partial \ln \rho(T)}{\partial \ln T} - \frac{\partial \ln \varepsilon_r(T)}{\partial \ln T} \right)$$

For Debye lengths larger than the particle radius, we obtain a spatially isolated point charge and find a constant Soret coefficient

$$\lim_{\lambda_{DH}\to \infty} S_T^{CM}\,\frac{R}{Z_{eff}^2} = \frac{-e^2}{8\pi k_B T^2 \varepsilon_r \varepsilon_0} \cdot \frac{\partial \ln \varepsilon_r(T)}{\partial \ln T}$$

Seebeck Effect. The ions in solution also experience thermophoresis. Since their Soret coefficients differ for each ion species - something which is known from thermo-electric measurements - long ranging electric fields build up in a temperature gradient (Fig. 1b). What follows is common electrophoresis of all charged species in this electric field. The resulting movement is macroscopically indistinguishable from thermophoresis and leads to an additional contribution to the Soret coefficient.

In analogy to solid state physics, we call this effect the Seebeck effect. The theory for monovalent salts

was first described by Guthrie (*7*) and further discussed by Würger (*8*). The particle flux j for each species i consists of mass diffusion (diffusion coefficient D), thermophoresis (thermophoretic mobility D_T) and electrophoresis (electric mobility μ and electric field E). In the steady state, the particle flux for each species is zero:

$$0 = j_i = -D_i \nabla c_i - D_{Ti} c_i \nabla T + \mu_i c_i E$$

For the salt ions we use the approximation $\mu_i = \frac{Z_i \cdot e \cdot D_i}{k_B T}$ with charge number Z_i. After considering the neutrality condition $\sum_i Z_i \nabla c_i = 0$ and summing over all species i we find:

$$E = \frac{k_B T \cdot \nabla T}{e} \cdot \frac{\sum_i Z_i c_i S_{Ti}}{\sum_i Z_i^2 \cdot c_i}$$

Please note that the thermal conductivity of the molecule does not significantly differ from the surrounding water. Therefore there is no significant distortion of the thermally induced electric field by the Seebeck effect due to the presence of the macromolecule. For highly thermal conducting particles such as gold, this could be however different. Due to the low DNA concentration in our experiments of 1 µM, DNA does not significantly contribute to the concentration-weighed sum with dissolved ion concentrations larger than 0.5 mM. Likewise, due to the neutral pH, no significant contributions of the OH^- or H_3O^+ ions are found (supplementary material S4). The DNA therefore follows the electric fields with mobility μ_{DNA}. The result is an additional contribution to the Soret coefficient given by

$$S_T^{EL} = -\frac{k_B T \cdot \mu_{DNA}}{e \cdot D_{DNA}} \frac{\sum_i Z_i c_i S_{Ti}}{\sum_i Z_i^2 \cdot c_i}$$

Non-Ionic Contributions. Above terms describe the ionic contributions to thermophoresis. The remaining Soret coefficient S_T^{NI} does not depend on the ion compositions of the solution (except indirectly in the case when the folding of the protein depends on the ions) and is attributed to the molecule – water interaction. Its empirically described footprint (*9*) is a temperature dependence with fitting parameters T^*, T_0, and S_T^∞:

$$S_T^{\mathrm{NI}} = S_T^\infty \cdot \left[1 - \exp\left(\frac{T^* - T}{T_0} \right) \right]$$

Due to the local structure of water, its amplitude is expected to scale with the local surface structure of the molecule.

S2 Materials and Methods

Measurements were performed with an upright fluorescence microscope (Zeiss Vario Scope.A1) using an air objective (Partec 40x/0.80 NA), a CCD camera (Andor Luca DL-658M-TIL) and heating from an infrared laser (Fibotec, λ = 1480 nm absorbed in water, typical emission power 28 mW) (*5*, *18*), coupled into the optical path right above the objective. To keep convection artifacts below experimental error, measurements were performed in borosilicate capillaries with an inner rectangular cross section of 50 x 500 µm² (VitroCom Vitrotubes #5005-050). The thin sample, low numerical aperture and moderate concentration depletion (<50%) ensured that temperature and concentration profiles were equally averaged along the optical axis. For a sketch of the setup with its capillary, see Fig. S1.

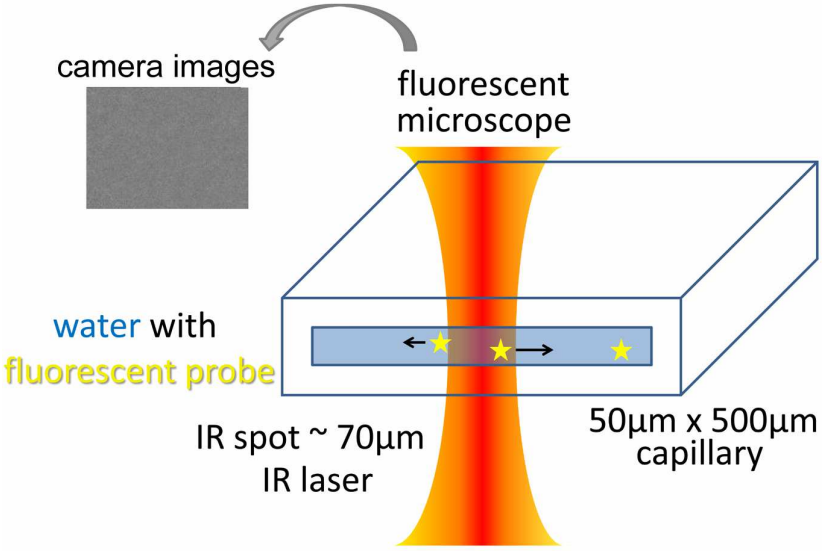

Figure S1. Experimental Setup and Capillary

Synthetic DNA and RNA labeled at the 5' end with the fluorescent dye HEX (6-carboxy-2',4,4',5',7,7'-hexachlorofluorescein) (Biomers, Germany) were diluted to 1 µM. Single stranded DNA (ssDNA) was measured in lengths of 2, 5, 10, 22, 50 and 80 bases, single stranded RNA (ssRNA) in lengths of 5, 10, 22 bases, double stranded DNA (dsDNA) in 22, 50 base pairs, and double stranded RNA (dsRNA) in 22 base pairs.

The following sequences were used in the experiments:

DNA
2mer: 5'–Hex–TA–3'
5mer: 5'–Hex–TAG GT–3'
10mer: 5'–Hex–TAG GTC TAA T–3'
22mer: 5'–Hex–ATT GAG ATA CAC ATT AGA ACT A–3'
50mer: 5'–Hex–ATA ATC TGT AGT ACT GCA GAA AAC TTG TGG GTT ACT GTT TAC TAT GGG GT–3'
80mer: 5'–Hex–CCT AAA GTC ATT GCT CCG AAT ATC TAC ACC GAA CCT AGA AAG TTG CTG ATA CCC GAT GTT TGT TTG ATT GTG AGT TGA GG–3'

RNA
5mer: 5'–Hex–UAG UU–3'
10mer: 5'–Hex–UAG UUC UAA U–3'
22mer: 5'–Hex–AUU GAG AUA CAC AUU AGA ACU A–3'
50mer: 5'–Hex–AUA AUC UGU AGU ACU GCA GAA AAC UUG UGG GUU ACU GUU UAC UAU GGG GU–3'

Double stranded probes contained an equal amount of complementary sequence. These probes were hybridized at stock concentrations prior to the experiment. The Debye length λ_{DH} was titrated using one of the following salts KBr, KCl, KF, KI, NaBr, NaCl, NaF, NaI, LiBr, LiCl, LiI, $CaCl_2$, $MgCl_2$, and monovalent 1 mM TRIS (2-amino-2-hydroxymethyl-propane-1,3-diol) at a pH of 7.8 at 25 °C. To keep sticking to the capillary walls in check, we added up to 0.1% vol. of Tween 20 in some experiments. Test measurements using 0.02%, 0.05% or 0.1% vol. of Tween 20 revealed no measurable difference in the Soret coefficient. The Debye length λ_{DH} = 13.8 nm was achieved by buffering with only 0.5 mM TRIS without additional salt. In measurements for the Seebeck effect, the concentration of TRIS was generally reduced to 0.5 mM and titrated to pH 7.5 at room temperature.

The profile of the intermittent local optical heating was measured using the temperature dependent fluorescence of the dye BCECF (acid form, Invitrogen B-1151) at a concentration of 50 µM in 10 mM TRIS, pH 7.8. The temperature profile was fitted in two dimensions with a Lorentzian $T(r) = T_0 + \Delta T\, w^2/(r^2+w^2)$. This revealed the heat center and the width. The width was varied between w = 30 and 70 ± 5 µm depending on the experiment with a temperature increase ΔT between 1.4 and 4.0 ± 0.1 K.

The chamber base temperature was controlled by Peltier elements (Telemeter Electronic GmbH, PC-128-10-05) and a heat bath. The chamber height of 50 µm and the moderate temperature rise of less than 4 K above base temperature kept thermal convection smaller than 0.6 µm/s, well below the error of the concentration measurement as confirmed by finite element simulations of the experiment. The measurement was automated and the LED, IR, motorized stage, temperature, and camera trigger were controlled with LabVIEW. The oligonucleotide concentration response in space and time was recorded at 5 Hz by fluorescence imaging of the covalently bound HEX label (*5, 6*). Five seconds of the equilibrated sample were imaged, followed by 120 seconds of thermophoretic depletion under optical heating and 120 seconds to monitor the back-diffusion after switching off the laser.

The dynamics of the whole experiment was modeled and analyzed to extract both the Soret coefficient S_T and the diffusion coefficient D. Including pipetting errors and camera noise, we estimate the systematic error for the Soret coefficient to 12%. Within error bars, the fitted diffusion coefficients did not depend on the Debye length (supplementary information S3). At 15°C, we found for single stranded DNA of length 2, 5, 10, 22, 50 and 80 bases a Debye-length-averaged diffusion coefficient $D(T)$ of 180, 153, 126, 107, 55, and 35 µm²/s. From these the hydrodynamic radii were calculated with the Einstein-Stokes formula (*19*) to 1.2, 1.4, 1.7, 2.0, 3.8, and 6.0 nm. Diffusion coefficients $D(T)$ changed with temperature in accordance to viscosity. No significant change of R over temperature had to be considered.
A LABVIEW program was used to trigger the fluorescence prediction of a radial symmetrical 1D FEMlab simulation, which can be obtained from the authors, and fit it to the optically detected fluorescence. The detection as well as simulation is determined for all times over the whole field of view of the camera, and circularly averaged around the heating spot. As result, the small concentration changes found for large radii are still detected since many pixels can be used for averaging including 8x8 binning of the camera head. The heating profile, determined by BCECF fluorescence, was fed into the FEMLAB simulation by a Lorentzian fit of the heating spot. The fitting parameters were the Soret coefficient S_T, the mass diffusion coefficient D, the temperature dependence of fluorescence and the bleaching time scale. Temperature, diffusion and bleaching equilibrated at time scales of typically 100ms, 10s and 1000s, allowing to fully separate them along the time axis. Fitting was only stopped when the complete radius-time images of the simulation reproduced the experimental radius-time fluorescence image in all details (Fig. S2, blue images on the right). This allowed to precisely fit above parameters and to check for experimental artifacts such as flow drift in the chamber, incomplete correction for bleaching or inhomogeneous illumination or a possible unstable heating profile. Most important were the measurement values of S_T and D which are extracted independently with this procedure.

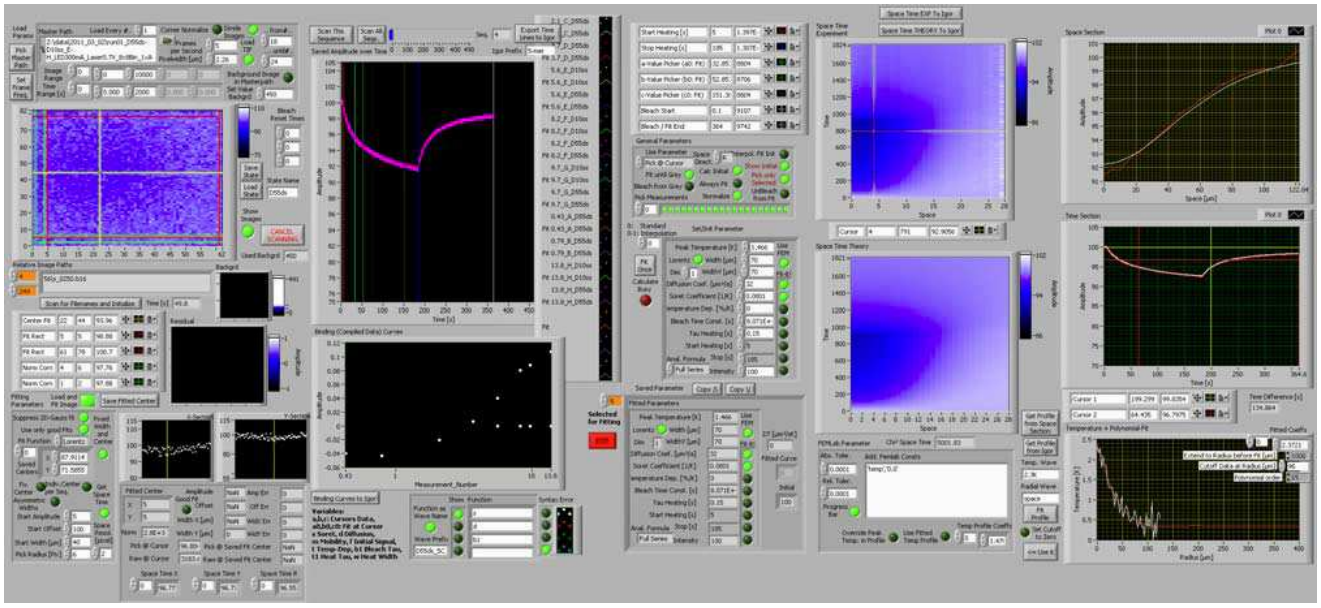

Figure S2. Front panel view of the LABVIEW analysis program.

S3 Data analysis for the Capacitor Model and determination of the hydrodynamic Radius

We deduced the diffusion coefficient D from the fluorescence change of the area around the laser spot and over a local heating and back-diffusion cycle. The measured diffusion coefficients D did not show a strong dependence on the salt concentration and therefore on the Debye shielding length λ_{DH}. The measurement of D becomes noisier when the thermophoretic depletion is low, i.e. at low temperatures and small Debye length λ_{DH}. The absence of clear trends in the measurements of the hydrodynamic radius R with respect to the Debye length motivated us to average R values over the Debye length. Also, within experimental error, the hydrodynamic radius R did not depend on the base temperature of the experiment (Fig. S3 and averages over λ_{DH} in table S1).

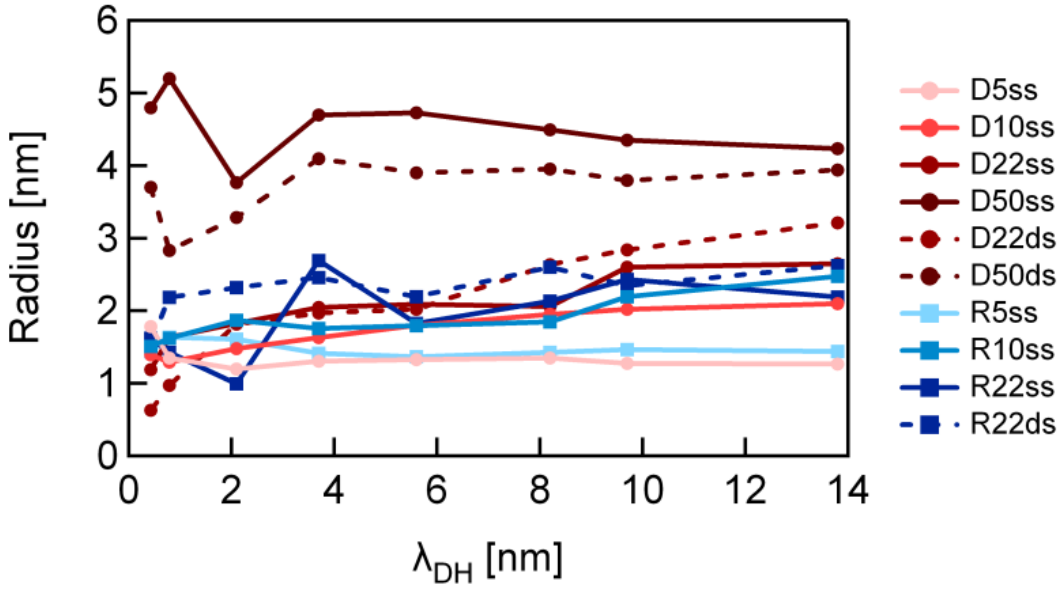

Figure S3. Hydrodynamic radius versus Debye length.

Table S1. Averaging over the Debye length yields the following hydrodynamic radii.

Sample	Radius [nm]	Sigma [nm]
5mer ssDNA	1.35	0.2
10mer ssDNA	1.71	0.3
22mer ssDNA	2.01	0.5
50mer ssDNA	4.53	0.4
5mer ssRNA	1.47	0.1
10mer ssRNA	1.88	0.3
22mer ssRNA	1.91	0.6
22mer dsDNA	2.01	0.9
50mer dsDNA	3.69	0.4
22mer dsRNA	2.28	0.3

For modeling the electrophoretic charge in Fig. 2c, and compare it to the results of the capacitor model, we added the two fixed charges from the 5' end-label HEX to the charge of the oligomer. The charge of the dye is included into the model as if it was a backbone charge. This means that the linker to the dye is assumed to be similar in terms of charge density as the phosphate backbone, leading to the same Manning condensation in the modeling. This is a reasonable approximation. As result, the attached dye was modeled as if two more bases were attached to the molecule.

Please note that we do not model the counter charges from Manning condensation to be temperature dependent and thus contributing to thermophoresis. We also measured single stranded RNA, double stranded DNA and double stranded RNA. In the case of double stranded species, only lengths above 22 base pairs were considered since shorter strands melt into single strands for elevated temperatures and low salt concentrations. While this melting transition can be measured with thermophoresis (*10*), it is not the aim of our systematic study. Therefore we considered the Debye length dependence of the double stranded species only below room temperature. Single stranded RNA was however measured for different lengths (5,10 and 22 bases) and also over temperature. We document the measurement at 35°C in Fig. S4a, the other measurements are included in Fig. S8 on the bottom right.

As seen, the capacitor model describes the measurements very well for single stranded RNA and reasonably well for the double stranded species where, due to the large persistence length the spherical assumption is rather a rough approximation that in itself depends on the Debye length. While double stranded RNA is described very well, double stranded DNA shows significant scatter (Fig. S4b). In all cases, we derived the effective charge per base from the measurements and included them in Fig. 2c for comparison with the electrophoresis data for single stranded DNA.

As expected due to their similar charge structure, single stranded RNA shows within experimental error the same effective charge than single stranded DNA (Fig. 2c and Fig. S4b). As already found for the plate capacitor limit (*10*), the Soret coefficient of double stranded DNA and RNA does not differ much from their single stranded versions, despite their nominal two-fold higher charge per base pair. Also in electrophoresis short double and single stranded DNA show very similar electrophoretic mobilities (*11*). Possibly, this points towards a stronger charge condensation from the higher charge density. For larger DNA lengths the charge per base pair drops to 0.3 *e* for double stranded DNA, converging well to the previously published value of 0.12 *e* for long DNA in the range of 50-50000 base pairs (*5*).

To test the generality of the approach, we measured 22mer single stranded DNA in $CaCl_2$ and $MgCl_2$ (Fig. 2d). As seen, the general capacitor model describes the measurements well with an effective charge number Z_{eff} and the offset $S_T(\lambda_{DH} = 0) = S_T^{EL} + S_T^{NI} + 1/T$ as fitting parameter. For both ions, we find a smaller charge per base ($Q_{per\ base}$) of 0.2 *e*, two fold smaller than the 0.4 *e* found for single stranded DNA in monovalent salts. A similar decrease of the electric mobility for higher valent salts, was documented before (*12*).

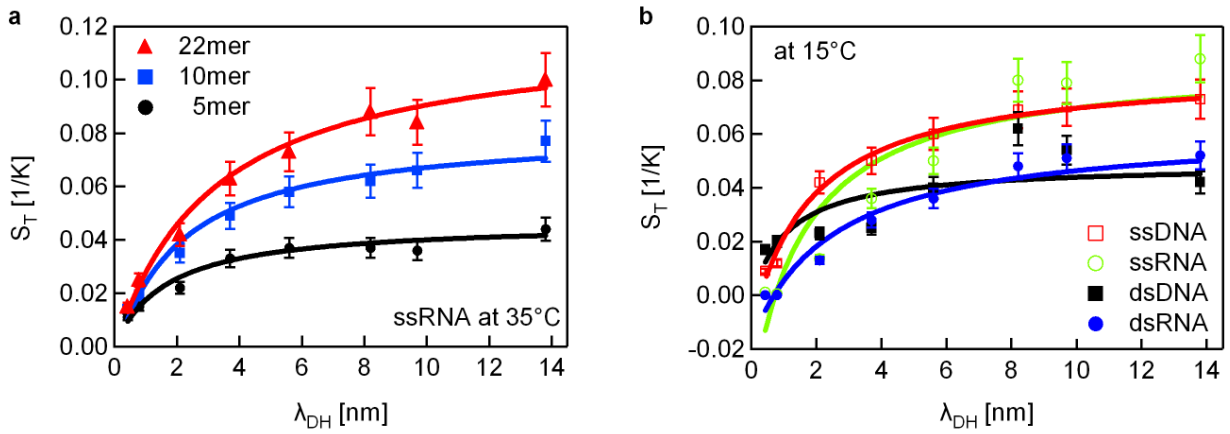

Figure S4. Size transition in S_T for single stranded RNA and double stranded RNA and DNA. (a) Highly similar to the findings for single stranded DNA in Fig. 2a, we confirm the size transition of the capacitor model also for single stranded RNA without fitting the radius *R* that was measured from the diffusion coefficient *D*. (b) The thermophoresis of single and double stranded DNA and RNA with a length of 22 bases is very similar at physiological salt concentrations (λ_{DH} = 0.8 nm). At lower salt concentration, single stranded molecules actually show a higher Soret coefficient than the double stranded versions at room temperature.

S4 pH Dependence

Table S2. Thermophoresis of DNA is insensitive to pH given that its charge remains constant.

Soret Coefficient [1/K]	pH	Buffer
-0.0270	13	no buffer
-0.0070	12	no buffer
0.0530	11	no buffer
0.0530	10	no buffer
0.0661	4	no buffer
0.0470	3	no buffer
-0.0081	13	1mM TRIS
-0.0051	12	1mM TRIS
0.0810	11	1mM TRIS
0.0781	10	1mM TRIS
0.0811	7	1mM TRIS
0.0851	4	1mM TRIS
0.0431	3	1mM TRIS

In all experiments, the buffer TRIS keeps the pH value between 8.4 (5 °C) and 6.5 (75 °C) (*27, 28*). TRIS has a temperature dependent dissociation constant, so the pH changes with -0.03 1/K in the heated region with negligible effects both on S_T^{CM} and S_T^{EL} (Fig. S6b). Buffering is required to ensure the pH value even for the small volume-to-surface ratio in the capillary setting. The pK_a value of the 6-Hex label is ~3 (*29*). The kinetics of pH equilibration are known to be much faster than the diffusive kinetics of thermophoresis.

As seen in the table S2, the Soret coefficient S_T of 50mer ssDNA was measured for buffered and unbuffered solutions at various pH values. Between pH 4 and 11 the buffered pH changes the Soret coefficient less than 10%, well within the error margins of the measurement. Outside the pH range, the thermophoresis drops sharply as expected from the reduced charge of the DNA. Measurements were performed at 25 °C and under the presence of 10mM KCl.

S5 Data analysis to detect the Seebeck Effect

We measured negatively charged 2mer, 22mer and 80mer single stranded DNA and positively charge Rhodamine in varying concentrations of KBr, KCl, KF, KI, NaBr, NaCl, NaF, NaI, LiBr, LiCl and LiI (see Fig. S5).

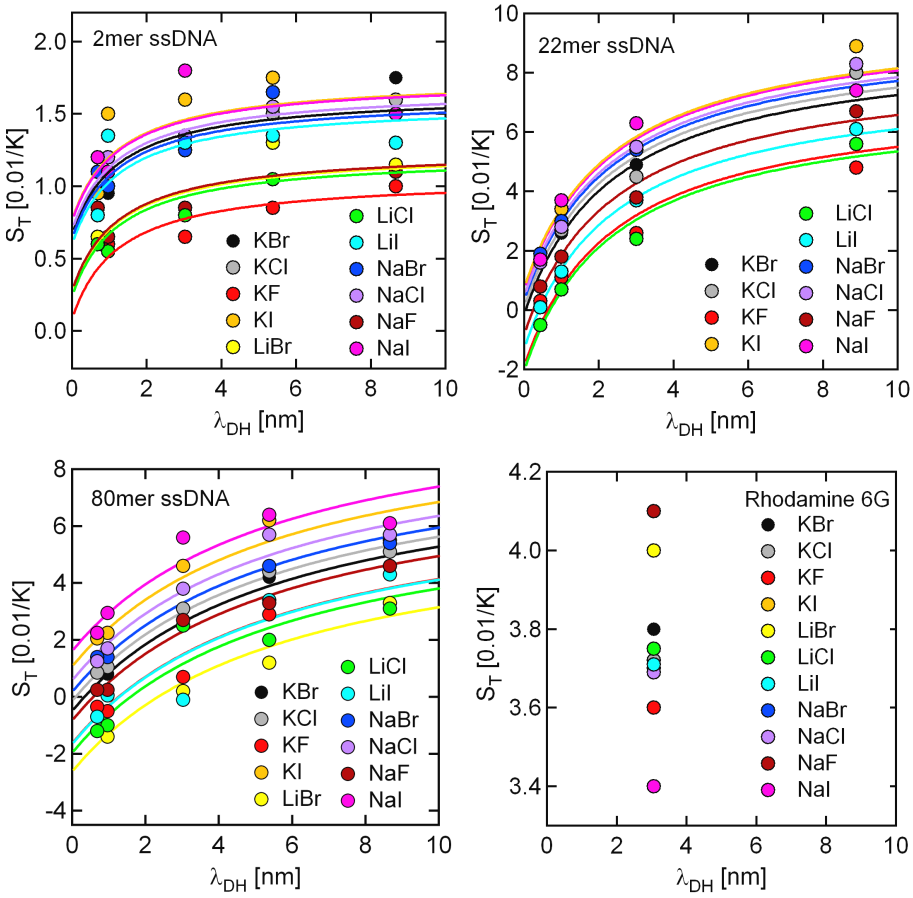

Figure S5. Measurements of Seebeck effect. The Soret coefficient of 2mer, 22mer and 80mer single stranded DNA (ssDNA) over λ_{DH} shows a salt species dependent offset in addition to the characteristic curve of the capacitor model. For zero Debye length, the capacitor contribution S_T^{CM} vanishes. For Rhodamine, measurements were not extrapolated, but taken at $\lambda_{DH} = 3$ nm for simplicity.

We fit the measurements as before with the capacitor model S_T^{CM} and attribute the salt-species dependent shift to S_T^{EL} according to eq. 1 for vanishing capacitor contribution at zero Debye length: $S_T(\lambda_{DH} = 0) = S_T^{EL} + S_T^{NI} + 1/T$. The measured S_T^{EL} is obtained by subtracting a salt independent constant $1/T + S_T^{NI}$ and is plotted over the theoretical Soret contribution S_T^{EL} which was calculated from eq. 3. The common non-ionic thermophoresis background S_T^{NI} was fitted to -0.00025 ± 0.00033, -0.016 ± 0.0011, and -0.013 ± 0.0015 1/K for the 2mer, 22mer, and 80mer, respectively.

We found μ_{DNA} = -1.2 ± 0.13, -2.6 ± 0.24, and -1.2 ± 0.13 x10^{-8} m^2/Vs for the 2mer, 22mer, and 80mer, consistent with literature values. In terms of absolute values, μ drops again for the 80mer, a phenomenon known from electrophoresis measurements (*11*, *12*). An effective charge can be computed with the

relation $Z_{eff} = \mu \frac{k_B T}{e \cdot D}$, which results in -1.7 ± 0.2 and -6.3 ± 0.6 for the 2mer and the 22mer, slightly smaller than the theoretical values -3.4 and -11.9 of Fig. 2c (*13*). On the other hand, the fit by the capacitor model resulted in effective charges Z_{eff} = -2.5 ± 0.5 and -11.0 ± 0.3 for the 2mer and 22mer, respectively. Considering the experimental errors, we find the match between the charge from the Seebeck effect and the charge from the capacitor model convincing.

In contrast to the capacitor model the Seebeck effect depends on the charge sign. The positively charged dye Rhodamine 6G indeed inverts the order of salt species in the thermophoretic shift (Fig. S5 lower right). With a positive mobility $\mu_{Rhodamine}$ = 2.2 ± 0.39 x10^{-8} m^2/Vs, the measurements again collapse on the theoretical expectations in Fig. 3a. The mobility is close to the literature value of 1.4 ± 0.06 x10^{-8} m^2/Vs (*14*). The effective charge derived by the Seebeck effect is 1.4 ± 0.3, close to the single charge expected for Rhodamine 6G.

Only measurements of longer DNA using lithium ions show an unexpected negative Seebeck shift. The Debye shielding theory does not account for size and coordination effects. Lithium is suspected to interact with DNA (*15*), possibly perturbing hydrogen bonds (*16*). As a result, it can change the prediction for S_T^{NI} through a salt species dependent change of the electrophoretic mobility. A good review on the ionic shielding of DNA and RNA can be found in (*17*). Thermophoretic and electrophoretic literature values in table S3 for the salt species were used to calculate the Seebeck effect.

Table S3. Soret coefficients and electrophoretic mobilities of ion species. Values of the hydrodynamic radius *R*, mass diffusion coefficient *D*, electric mobility μ, and Soret coefficient S_T used to calculate the Seebeck effect in Fig. 3a. The Soret coefficients S_T were taken from (*25*) and (*26*). The values of ion conductivities were taken from (*4*) and converted to mobilities μ. The diffusion coefficients *D* from (*4*) were converted to a hydrodynamic radius using the Einstein-Stokes relation (*19*).

Ion	D [µm²/s]	R [Å]	µ [m²/Vs]	S_T [1/K]
Ca^{2+}	792	2.76	6.16E-8	1.33E-2
K^+	1957	1.12	7.62E-8	3.51E-3
Li^+	1029	2.12	4.01E-8	7.18E-4
Mg^{2+}	706	3.09	5.49E-8	1.22E-2
Na^+	1334	1.64	5.19E-8	4.69E-3
Ni^{2+}	661	3.30	5.14E-8	1.26E-2
Br^-	2080	1.05	8.09E-8	8.13E-4
Cl^-	2032	1.07	7.91E-8	7.18E-4
F^-	1475	1.48	5.74E-8	5.32E-3
I^-	2045	1.07	7.96E-8	-2.10E-3
OH^-	5273	0.414	2.05E-7	2.33E-2
H_3O^+	9311	0.234	3.62E-7	1.80E-2

For better understanding of the molecular processes in thermo-electrophoresis, we simulated our measurements with a 1D radial finite element method FEMLAB 3.1 (COMSOL AB). The analysis of the data started from the eq. 3. We used the Nernst-Planck chemical engineering module, but substituted the

first differential equation with a Poisson equation. The simulation closely matched the analytical solution for S_T^{EL} of the different salt species. Additionally to mass diffusion and electrophoresis coming with the module, thermo diffusion was implemented for the salt cation and anion and the H_3O^+ and OH^- ions present, as determined by the pH. The electric field and thus S_T^{EL} is mainly independent of the salt concentration (Fig. S6a). When the pH is between 5 and 9 the charge of the DNA is constant (*20*). The contribution to the electric field of the H_3O^+ and OH^- ions (Fig. S6b) and the probe particle itself (Fig. S6c) is negligible as long as their concentration is small compared to the salt, although they have a large Soret coefficient and are highly charged, respectively.

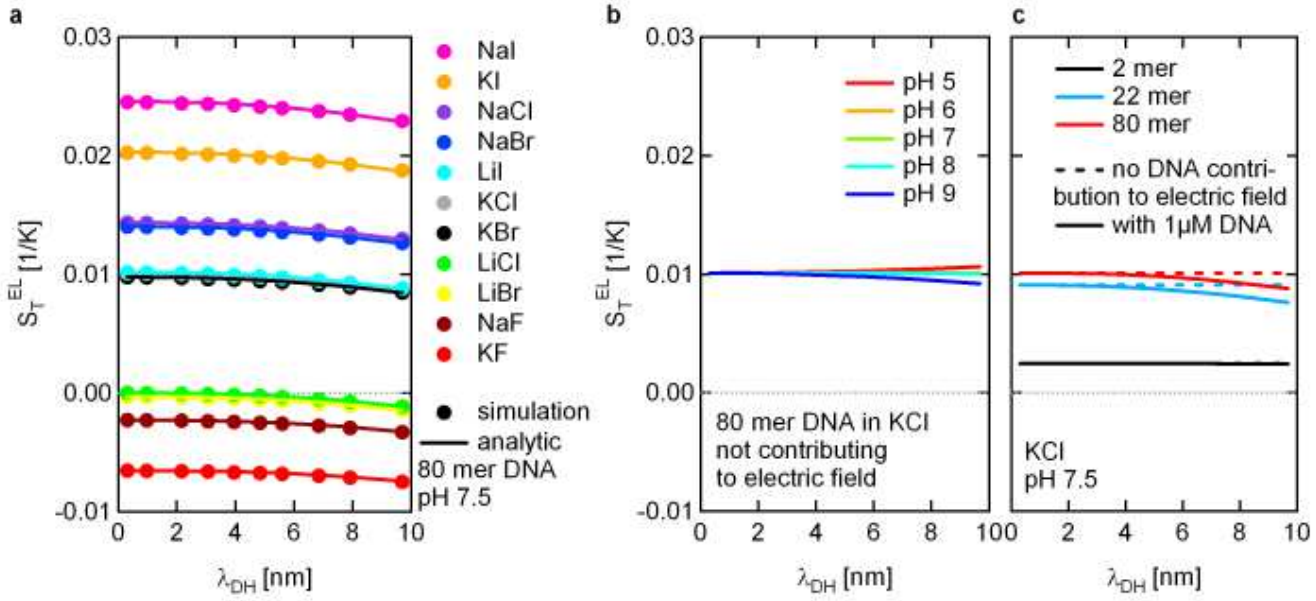

Figure S6. Checking the ion concentration dependence of the Seebeck-Effect. (a) In a finite element method simulation with FEMLAB we confirmed the analytical result of eq. 3 that S_T^{EL} is mainly independent of the Debye length, but changes with the salt species. (b) Close to pH 7 the influence of the H_3O^+ and OH^- ion concentration is negligible against the salt concentration in the mM range, despite their large Soret coefficients. (c) Also, the influence of 1µM DNA is minor although it is highly charged. Shown are the cases when the DNA does not contribute to the electric field (broken line) and when it contributes with its charge and $S_T^{NI} + 1/T + S_T^{CM}$, with the latter depending on the salt concentration.

The Seebeck effect is not affected by and does not require the container walls for accumulation or depletion of ions (Figure S7). In black, the finite element calculation includes also charge accumulation at the boundaries at x = -5 µm and x = +5 µm. At both locations, the thermal gradient ends at the container wall and within the Debye length of the simulation the electric field drops to zero at the container. Far from this Debye shielding, however, the analytical solution (red solid line) determines the electric field (Figure S7a). The same applies if the thermal gradient is changed within the solution without the interactions of a surface (Figure S7b). In conclusion, the analytical linearity between the electric field of the Seebeck effect and the thermal gradient *(7)* always holds, irrespective whether the thermal gradient is perpendicular to a boundary of the container or not. In our experiments, temperature is applied parallel to the container walls by infrared heating of water similar to Figure S7b.

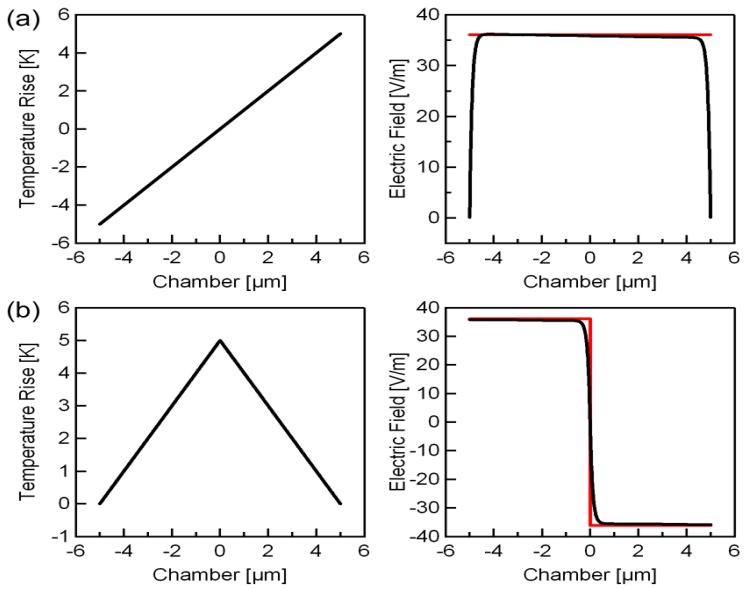

Figure S7. Boundary geometry of the container walls does not change the Seebeck effect. The electric field of the fully simulated Seebeck effect (black) follows the analytical solution (red) proportional to the thermal gradient according to *(7)*. This dependence is independent on the container boundaries. (a) The temperature gradient is applied at the container walls. Within the Debye length, the electric field changes as ions are attracted to the container walls. For a distance from the container walls that is larger than the Debye length, the electric field is constant and follows the analytical solution plotted in red. (b) The same is found if the temperature gradient makes a swift change within the fluid, independent from the container walls. The electric field of the Seebeck effect can only change within a length scale determined by the Debye length. After this length scale, the simulation follows the analytical solution in red. For this example simulation, we used a 1D nonradial geometry with a chamber length of 10µm. A concentration of 10µM KCl was used to tune the Debye length to 0.137 µm, well visible in the plots and easily converging with an average sized calculation grid. The temperature gradient was fixed to 1 K/µm. Other parameters such as were taken as documented before, i.e. the diffusion coefficients $D(K+)=1.957 \times 10^{-9}$ m²/s, $D(Cl-)=2.032 \times 10^{-9}$ m²/s, electrophoretic mobilities $\mu(K+)=7.62 \times 10^{-8}$ m²/Vs, $\mu(Cl-)=-7.91 \times 10^{-8}$ m²/Vs and Soret coefficients $S_T(K+)=3.51 \times 10^{-3}$ 1/K and $S_T(Cl-)=7.18 \times 10^{-3}$ 1/K. This resulted in the analytical electric field of $E = 8.617 \times 10^{-5}$ eV/K x 300K x 10^6 K/m/e x (3.51×10^{-3} 1/K - 7.18 1/K) / 2 = 36.1 V/m in accordance with the simulation.

S6 Dependence on DNA Concentration: Seebeck and Capacity Model contributions

Our experiments were conducted with 1 µM DNA/RNA concentration. Particle-particle interactions are not expected to contribute at this concentration level (*21,22*) and particle-particle interactions (*21–23*) were not considered. Typically non-fluorescent measurements of thermophoresis are performed in 100-1000 fold higher concentrations where an empiric concentration correction has to be applied (*23, 24*).

To evaluate the influence of the sample concentration, we measured the Soret coefficient from 0.2 to 26 µM of 50mer ssDNA in 10 mM KCl, 1mM TRIS pH 7.8, 0.05% vol. of Tween. The excitation light from an LED was adapted to reach the same fluorescence intensity for all sample concentrations. As in all experiments, differential bleaching was corrected particularly for the lower concentration samples.

As shown in Fig. 3b and Fig. S6c, concentration dependent contributions are explained by the concentration dependent change of the Debye length and a changed contribution to the Seebeck effect. Both effects are generally small for the used µM DNA concentrations in our experimental conditions. However, the effect can be measured.

To describe the concentration dependence analytically, we considered the influence of the DNA concentration and its K^+ counter ions on the Debye length in the capacitor model part S_T^{CM} of the Soret coefficient. In addition, the DNA contributes to the electric field (eq. 3) with $S_{T\,DNA} = 1/T + S_T^{NI} + S_T^{CM}$. To calculate the Seebeck contribution S_T^{EL}, we assumed the following constants for the 50mer interpolated from the measured values for the 22mer and the 80mer: the hydrodynamical radius R = 4 nm, the effective charge number for the capacitor model Z_{eff} = -16.5, the temperature T = 25°C, the electric mobility μ = 1.44x10^{-8} m^2/Vs, and the non ionic part of the Soret coefficient S_T^{NI} = -0.016 1/K.

S7 Non-ionic Contribution and 2D Fit.

The non-ionic contributions in Fig. 3c almost have a common intersection, suggesting a possible master curve. However small remaining shifts for the different DNA lengths make the fitting values of T_0 and T^* scatter with average values of $T_0 = 14 \pm 5$ °C and $T^* = 28 \pm 16$ °C (table S4). Notably, the value of T^* agrees with the previously determined $T^* = 18$ °C for long double stranded DNA (*5*). In contrast to the amplitude value S_T^∞ , which scales linearly with the length of the polymer (inset in Fig. 3c), no clear interpretation could be found for the fit parameters T_0 and T^* which we document in the table S4:

Table S4. Fit parameter values for T_0 and T^*.

Sample	T_0 [°C]	T_0 sigma	T* [°C]	T* sigma
5mer ssDNA	18	4.3	48	15
10mer ssDNA	19	2.7	23	2.5
22mer ssDNA	7.8	2.0	14	2.8
50mer ssDNA	14	2.7	15	2.0
5mer ssRNA	9.5	4.5	40	66
10mer ssRNA	13	3.2	31	8.5
22mer ssRNA	24	3.7	57	8.7
22mer dsDNA	12	2.8	9.5	1.8
50mer dsDNA	12	2.4	13	1.9
22mer dsRNA	15	1.8	31	3.4

In combination of all contributions of eq. 1, we expect that the microscopic model should predict the Soret coefficient for various molecule lengths over temperature and Debye length without additional fitting parameters. In Fig. S8 the Soret coefficient S_T is plotted two-dimensionally (thin lines) and fully described with the model (eq. 1, thick lines). To recapitulate previous discussions, the data of Fig. 2a is found from a horizontal cut through Fig. S8, Fig. 3d are vertical cuts at various Debye lengths and Fig. 3c is an extrapolated vertical cut at $\lambda_{DH} = 0$. As can be seen, all experimental data is well accounted for by eq. 1 over a large temperature and salt range for single and double stranded DNA and RNA with various lengths. This demonstrates the prediction power of our microscopic thermophoresis model in a multidimensional parameter space.

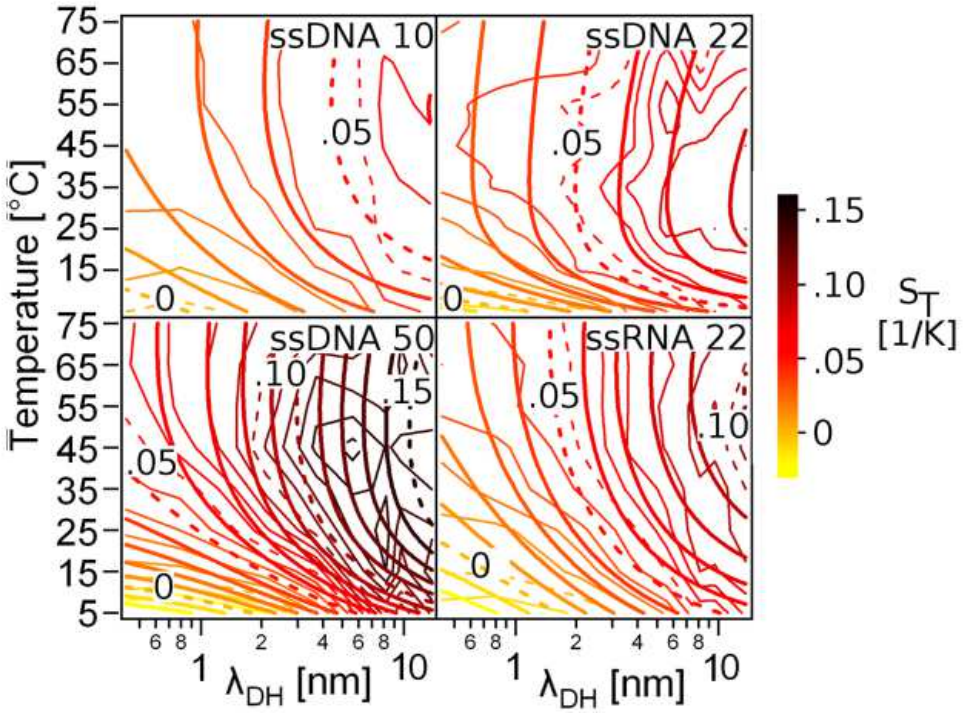

Figure S8. Two dimensional data set. The combination of ionic shielding, thermo-electrophoresis, and non-ionic predictions of the Soret coefficient by eq. 1 yields a robust description (broad lines) of the measurement set (thin lines) over temperature and Debye length. Here, the constant offset from $S_T^{EL} + S_T^{NI} + 1/T$, and the charge per base are fitted variables.

References for Supplementary Material

1. S. Duhr, D. Braun, *Phys. Rev. Lett.* **96** 168301 (2006).
2. J. K. G. Dhont, S. Wiegand, S. Duhr, D. Braun, *Langmuir* **23**, 1674 (2007).
3. R. D. Astumian, *Am. J. Phys.* **74**, 683 (2006).
4. D. R. Lide, *CRC handbook of chemistry and physics* (CRC Press, Boca Raton, ed. 82, 2001).
5. S. Duhr, D. Braun, *Proceedings of the National Academy of Sciences* **103**, 19678 (2006).
6. P. Reineck, C. J. Wienken, D. Braun, *Electrophoresis* **31**, 279 (2010).
7. G. Guthrie, J. N. Wilson, V. Schomaker, *J. Chem. Phys.* **17**, 310 (1949).
8. A. Würger, *Phys. Rev. Lett.* **101** 108302 (2008).
9. S. Iacopini, R. Rusconi, R. Piazza, *Eur. Phys. J. E* **19**, 59 (2006).
10. C. J. Wienken, P. Baaske, S. Duhr, D. Braun, *Nucleic Acids Research* **39**, e52 (2011).
11. E. Stellwagen, Y. Lu, N. C. Stellwagen, *Biochemistry* **42**, 11745 (2003).
12. R. W. O'Brien, L. R. White, *J. Chem. Soc., Faraday Trans. 2* **74**, 1607 (1978).
13. O. A. Hickey, T. N. Shendruk, J. L. Harden, G. W. Slater, *Phys. Rev. Lett.* **109** 098320 (2012).
14. D. Milanova, R. D. Chambers, S. S. Bahga, J. G. Santiago, *Electrophoresis* **32**, 3286 (2011).
15. Q. Dong, E. Stellwagen, N. C. Stellwagen, *Biochemistry* **48**, 1047 (2009).
16. E. Stellwagen, Q. Dong, N. C. Stellwagen, *Biopolymers* **78**, 62 (2005).
17. J. Lipfert, S. Doniach, R. Das and D. Herschlag, *Annual Review of Biochemistry* **83**, 19.1–19.29 (2014).
18. C. J. Wienken, P. Baaske, U. Rothbauer, D. Braun, S. Duhr, *Nat. Comms.* **1**, 100 (2010).
19. A. Einstein, *Ann. Phys.* **322**, 549 (1905).
20. S. Chatterjee *et al.*, *Org. Biomol. Chem.* **4**, 1675 (2006).
21. J. K. G. Dhont, *J. Chem. Phys.* **120**, 1632 (2004).
22. J. K. G. Dhont, *J. Chem. Phys.* **120**, 1642 (2004).
23. R. Piazza, A. Guarino, *Phys. Rev. Lett.* **88** (2002).
24. S. A. Putnam, D. G. Cahill, G. C. L. Wong, *Langmuir* **23**, 9221 (2007).
25. N. Takeyama, K. Nakashima, *J. Solution Chem.* **17**, 305 (1988).
26. C. J. Petit, M.-H. Hwang, J.-L. Lin, *Int J Thermophys* **7**, 687 (1986).
27. C. A. Vega, R. A. Butler, B. Perez, C. Torres, *J. Chem. Eng. Data* **30**, 376 (1985).
28. A. El-Harakany, F. Abdel Halim, A. Barakat, *Journal of Electroanalytical Chemistry and Interfacial Electrochemistry* **162**, 285 (1984).
29. R. P. Haugland, M. T. Z. Spence, I. D. Johnson, A. Basey, *The handbook, A guide to fluorescent probes and labeling technologies* (Molecular Probes, Eugene, OR, ed. 10, 2005).

Thermophoresis imaging inside living cells

Maren Reichl and Dieter Braun

Systems Biophysics, Physics Department, NanoSystems Initiative Munich and Center for Nanoscience, Ludwig-Maximilians-Universität München, Amalienstrasse 54, 80799 München, Germany

The complexity of biology requires that measurements of biomolecular interactions have to be performed inside the living cell. While electrophoresis is prohibited by the cell membrane inside cells, the movement of molecules along a temperature gradient appears feasible. This thermophoresis could recently quantify binding affinities *in vitro* at picomolar levels and perform pharmaceutical fragment screens. Here we changed the measurement paradigm to enable measurements inside living cells. The thermal gradient is now applied along the optical axis and measures thermophoretic properties for each pixel of the image. We verify the approach for polystyrene beads and DNA of various lengths using finite element modeling. Thermophoresis inside living cells is able to record thermophoretic mobilities and intracellular diffusion coefficients across the whole cytoplasm. Interestingly, we find a 30-fold reduced diffusion coefficient inside the cell, indicating that molecular movement across the cell cytoplasm is slowed down due to molecular crowding.

Introduction. Thermophoresis is the movement of molecules in a temperature gradient. Its strength is sensitive even to minute binding events, allowing Microscale Thermophoresis (MST) to measure binding affinities of DNA [1], proteins [2], pharmaceutical components [3], and even membrane receptors [4]. When the fluorescent amino acid tryptophan is present, additional labeling of the probe can be omitted [5]. Recently, protein binding at the picomolar level was reported [6]. In contrast to enzyme-linked immunosorbent assay (ELISA), thermophoresis measurements can be conducted without surface fixation in the molecule's natural environment, such as blood serum [7] or cell lysate [8]. The method was commercialized by Nanotemper and has lead to many insights into complex biological systems [9-12], including tubulin binding to transport proteins [13] and binding studies of avian influenza to cell surface receptors [14].

Besides above *in vitro* applications of thermophoresis, thermal gradients are unique since they transcend material boundaries and, similar to light fields, are therefore capable to probe molecules even inside living cells. For example, electrical fields are shielded by the cell membrane and electrophoresis inside cells cannot be achieved. In order to achieve thermophoresis in living cells, the previous horizontal geometry of Microscale Thermophoresis [1,8] had to be adapted to cell cultures. Here we explore a vertical gradient across a sandwich chamber. The adherent cells grow on a standard cover slip, and are then inserted into the measurement setup. With this approach, *in vivo* thermophoresis from molecules inside cells can be obtained. And when thermophoresis data from inside living cells is available, binding measurements *in vivo* become a realistic goal.

A variety of other methods to measure non-biological thermophoresis have been explored. In a parallel plate geometry measurements are save from convection, but can take hours to complete [15,16]. Experiments in a micron-sized interdigitated setup are much faster [17]. In the beam deflection method, a gradient of refractive index is measured [18,19,20]. Often, this requires

sample concentrations in the order of weight percent, typically hard to achieve with biological probes without aggregation artifacts. The same applies for the thermal lensing method [21] and thermal diffusion forced Rayleigh scattering [22,23]. In confocal microscope geometry short distances and fast measurements are achieved [24]. Matching the speed of axial thermophoresis was used to probe strong thermal gradients [25]. With a fluorescent label small molecule concentrations down to picomolar concentrations can be measured [6].

Results. We use a thin sheet of solution where we apply the temperature gradient with a cold top and a warm bottom. Fluorescence detection is restricted by using TIRF microscopy to the top side, imaging the upward thermophoretic movement towards the cold. In this geometry, every camera pixel can simultaneously and independently measure thermophoresis. For details on the setup see supplementary material. The temperature profile was measured using the fluorescence of BCECF (see supplemental material). Under LED illumination, the lateral temperature distribution is imaged, averaging across the thickness of the chamber. The images and the known geometry were used to fit a three dimensional finite element calculation (Fig. 1b, c).

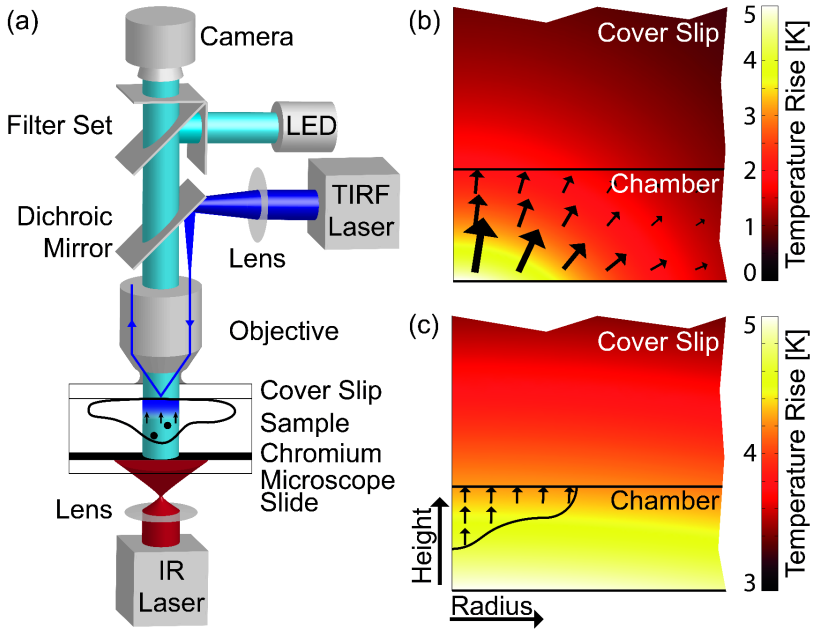

Figure 1. Setup *(a). Two illumination paths were integrated into an upright fluorescence microscope setup: normal epi-illumination with LED and TIRF illumination. Heating is provided from below by an IR laser that was absorbed by a chromium layer. The temperature simulations are shown for a 10 µm thick chamber with variable IR spot focus width: (b) 15 µm and (c) 150 µm. The molecules move along the temperature gradient, indicated by arrows.*

We first used polystyrene beads to confirm the thermal transport approach. In a 20 µm high chamber, comparably large beads with Radius $R = 1$ µm which are in the beginning sedimented to the bottom of the chamber are during the measurement transported to the top side where they are detected via fluorescence (Figure 2a). As shown for various times of the experiment, a one-dimensional finite element simulation was used to model the combined gravitational, diffusional and thermophoretic movement of the beads. At the top of the chamber, the thermophoresis enforces an inverted exponential sedimentation distribution.

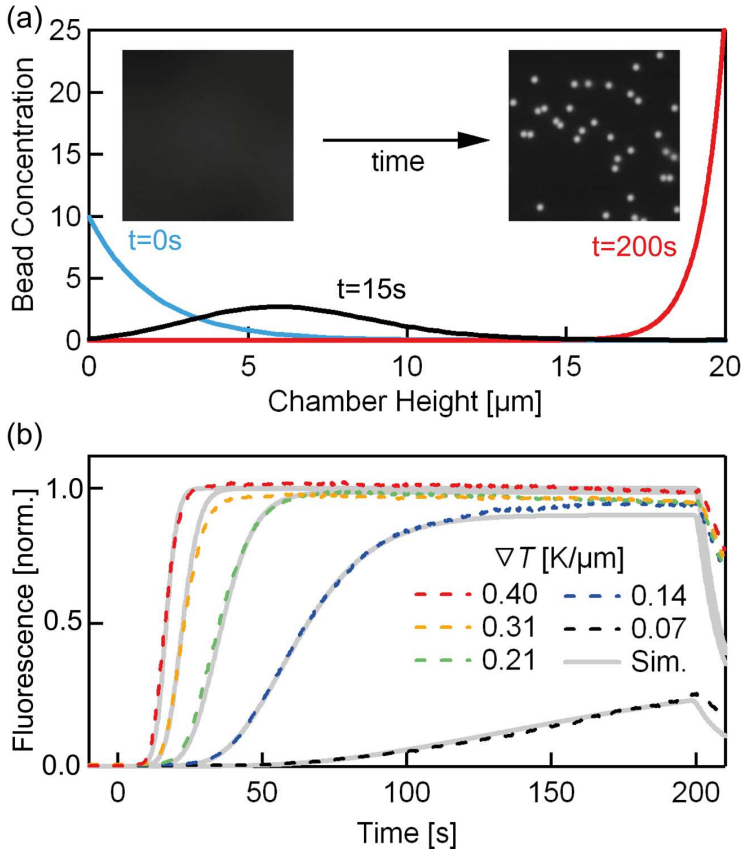

Figure 2. *Imaging thermophoresis with beads. (a) Polystyrene particles with radius R = 1 µm initially sediment and during the measurement move upwards to be imaged at the top the top of the chamber. Simulation shown for a gradient of* $\nabla T = 0.21\, K/\mu m$. *(b) Fluorescence is used to image the concentration of the beads at the top of the chamber. With increasing thermal gradient, the transit times of the beads become shorter. All measurements are described with a thermophoretic mobility of* D_T *= 2.8±0.5 µm²/sK and the mass diffusion coefficient D = 0.20 µm²/s known from the particle radius.*

The bead concentration at the top was detected by fluorescence. With increasing temperature gradient, the beads travel across the chamber with increasing speed $v_T = D_T \cdot \nabla T$, while for shallow thermal gradients, they can barely overcome sedimentation, which was calculated from the weight difference to water of $\Delta\rho = 60\, kg/m^3$ (Figure 2b). With the known mass diffusion coefficient of the beads (D = 0.20 µm²/s) interfered from their radius, the only fitting parameter is the thermophoretic mobility D_T which was fitted to a constant value of 2.8 ± 0.5 µm²/(sK) for all measured thermal gradients. The measurement setup allows to probe thermophoresis for Péclet numbers larger than unity [25]. At the highest gradient of 0.2 K/µm, the Péclet number reaches $Pe = (R\nabla T D_T / D) = 2.7$, indicating that the comparably large beads and the considerable thermal gradient allow for a ballistic, not a diffusional particle movement. For the high temperature gradients also clustering at the cover slip was observed [25].

Before performing measurements in cells, the imaging thermophoresis configuration using TIRF detection was first tested with DNA where sedimentation is not an issue (Fig. 3). We study the case where focused heating (Fig. 1b) combines vertical and lateral thermophoresis. With epi-illumination using an LED, detection averages across the chamber height and only the lateral outwards movement is detected. Under TIRF illumination, both the coaxial upward

and lateral outward component of thermophoresis is measured.

We used DNA of different length as a molecular test system due to their well-established parameters. Measurements were performed at different thermal gradients under both TIRF and LED detection (Fig. 3 dotted lines). Fluorescence at the heat spot center was recorded at 3 Hz. When heating is turned on (t = 0 s), fluorescence drops within < 1 s due to its inherent temperature dependence. Under TIRF illumination, this drop is superimposed with the fluorescence raises due to the upward molecule movement. This is later decreased by the lateral outward thermophoresis due to the focused heating spot. The thermophoretic amplitude increases for increasing temperature gradient (Fig. 3a). Under epifluorescent LED illumination, only the temperature dependence and the lateral outward depletion of the molecules is visible. Measurements with longer DNA strands show slower diffusion and the coaxial upward thermophoresis is detected since the lateral thermophoresis does not yet equilibrate within the heating time of 60 s (Fig. 3b). After switching off the temperature gradient (t = 60 s), back-diffusion equilibrates the thermophoretic perturbation of DNA concentration.

We quantified the DNA measurements with the known molecular parameters in a two dimensional, radial finite element simulation (supplementary information). We implemented heat conduction, diffusion, thermophoresis, bleaching under TIRF or LED illumination, temperature dependence of the fluorescent dye and a possible thermal convection flow. The resulting fluorescence traces fit the experimental measurements in detail over a wide range of temperature gradients and DNA lengths (Fig. 3). The mass diffusion coefficient D could be determined by the model to D = 14, 10, 6.0, or 2.5 µm²/s, for the lengths of 0.6, 1, 3, and 20 kbp, respectively, which agreed with literature values [26]. The only unknown parameter was the thermophoretic mobility D_T. For the measured DNA lengths of 0.6, 1, 3, and 20 kbp, we found D_T = 2.2, 2.8, 1.5, or 1.1 µm²/sK, confirming previous measurements of DNA

thermophoresis [27]. Interestingly, we could fit both the coaxial and lateral thermophoresis traces with the same value for the thermophoretic mobility D_T. For details on the fits, see the supplementary material.

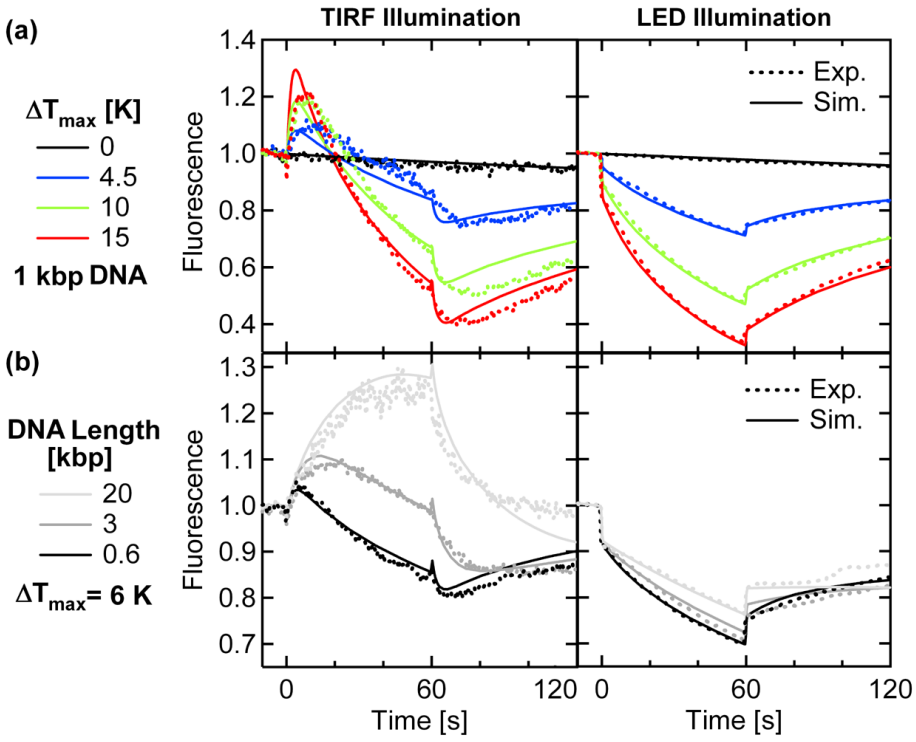

Figure 3. *The IR laser was focused to a small spot (HWHM = 65 µm) and moved the molecules upwards coaxially and outwards laterally. The fluorescence above the heat spot center was detected with TIRF. Epifluorescence LED illumination did not discriminate across the chamber height. Measurements (dotted line) were conducted with (a) 1 kbp DNA in different temperature gradients and (b) different DNA lengths in the same temperature profile. Finite element simulations described the thermophoretic molecule movement in detail (solid lines).*

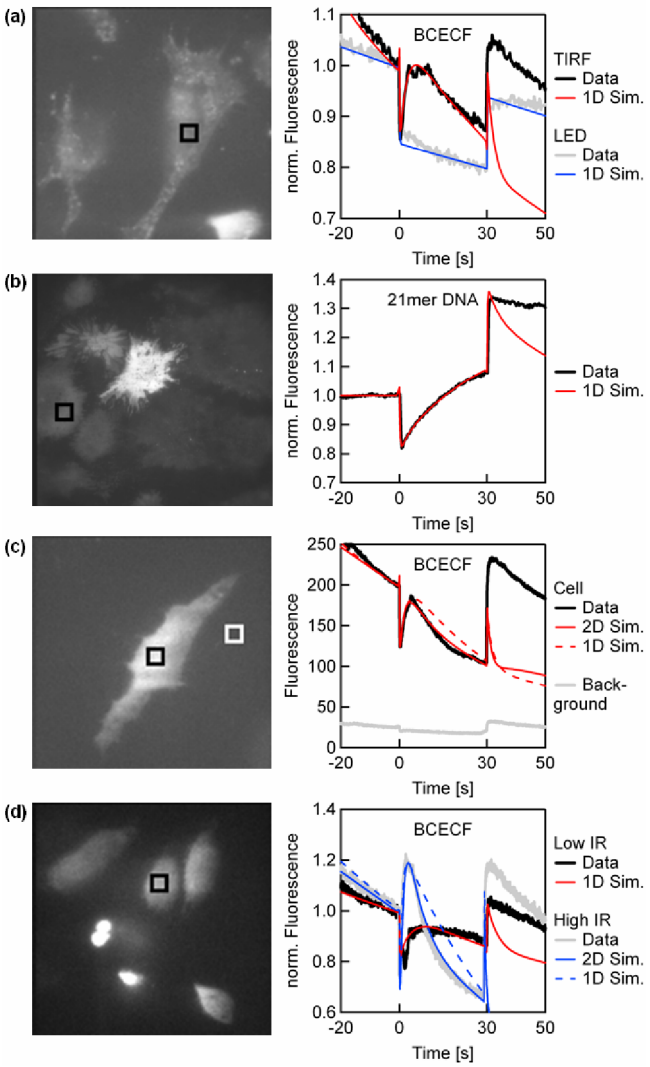

Figure 4. *Thermophoresis measurements of DNA and BCECF in the cytoplasm of living cells. Thermophoresis of molecules were detected by TIRF fluorescence imaging over time. (a) The dye molecule BCECF is moved to the cold side after a fast fluorescence decrease due to its temperature dependence. Control measurement under epi-illumination with LED demonstrate that the fluorescence increase stems only from the vertical movement of the fluorophore. (b) Double stranded DNA with 21 bases showed slower thermophoresis with a larger accumulation magnitude than BCECF. (c) The extracellular background trace is darker, does not show the thermophoresis signature and is not affecting the thermophoresis measurement significantly.*

The bending of the trace is understood by the cone-shaped cell geometry. (d) Measurements in higher temperature gradients show an expected increased in the thermophoretic amplitude.

We confirmed that the chromium layer absorbed all the infra-red (IR) light by measuring the transmission of the IR laser through the chromium coated glass slide with a power meter (PM100USB and S310C Thorlabs GmbH). As a result, the upward movement of the particles could not be influenced by photonic pressure. As additional check, we performed experiments under TIRF detection without chromium. The resulting lack of a vertical temperature gradient coincided with an undetectable vertical net movement of the molecules.

We imaged thermophoresis inside living cells after fully understanding thermophoresis traces under the TIRF detection and coaxial heating. The measured fluorescence traces of thermophoresis inside living HeLa cells are shown in Fig. 4. On the left sides, the fluorescence image of representative cells are shown. The fluorescence time traces on the right correspond to the intensities in the black squares in the cell image.

The IR heating laser was turned on between times 0 s and 30 s. As before, the temperature dependence of the fluorophore results in a sudden drop of the signal, after the IR is switched on and a reverted increase after heating is again switched off. As before, control measurements under epifluorescence LED illumination were conducted. Here, an axial, upward fluorophore motion cannot be resolved and only the temperature jump is visible (Fig. 4a). With LED illumination the temperature jump is slightly larger than under TIRF illumination, since the LED excites the fluorescence deeper in the chamber, where it is warmer (see Table I). Lateral thermophoresis is also not expected due to the more defocused heating in the cell measurements (see Figure 1c). Fig. 4b shows a measurement of 21 base pair DNA while the other measurements report the movement of the pH sensitive dye BCECF. As before, the measurements were fitted with finite element simulations as detailed

in the supplementary section. All parameters are listed in Table I.

Interestingly, the diffusion of BCECF was found to be $D = 3\ \mu m^2/s$, considerably slower than the free buffer values from the cytoplasm of 100 $\mu m^2/s$ reported using FRAP analysis of the mobile fraction [28]. For the measurements with 21mer double stranded DNA, we find a diffusion coefficient of 0.1 $\mu m^2/s$, also reduced compared to the reported 20 $\mu m^2/s$ [29]. Since this method actively moves the molecules, it measures the average over all fractions mobile and possibly immobile. The main contribution in slowing down diffusion is thought to be the collision with other macromolecules [29,30]. So a size dependent further reduction of these values is expected when thermophoresis of biomolecules bound to other molecules is considered. We also tried to measure larger molecules (ribosomes with GFP label), but the reduction of diffusion made it impossible to detect sufficient (thermophoretic) movement. Thermophoresis, in contrast to all other techniques, actively moves the molecules and therefore probes their mobility on a global scale. As a result, interactions with the cytoplasm at a larger scale can be probed by thermophoresis.

Interestingly for BCECF, the thermophoretic mobility is unaffected by the cell. The measured value of $D_T = 4.4 \pm 2\ \mu m^2/(sK)$ is well compatible with the reported *in vitro* value of $D_T = 7.5\ \mu m^2/(sK)$ [27]. In contrast, the DNA probe is reduced both in diffusion and thermophoretic mobility with a value of $D_T = 0.12\ \mu m^2/(sK)$ as compared to $D_T = 1\ \mu m^2/(sK)$ [31]. These measurements suggest that molecular interactions inside a cell can be differentiated between affecting thermophoretic mobility or diffusivity.

In Figure 4c and d, the thermophoresis traces show a curved fluorescence decrease during thermophoresis which could not be readily explained even with TIRF bleaching dynamics in the 1D simulations (broken line). We propose that this effect is due to the inhomogeneous thickness of the individual cell, leading to a temporarily build-up of lateral concentration inhomogeneities within the cells that subsequently equilibrate. We modeled such a cell in a

2D radial geometry, as a cone with height 10 µm and radius 20 µm the readout being above the center, but still with a purely vertical, constant temperature gradient. This 2D model could explain the curved cell traces (see supplementary material). Background fluorescence could be measured next to a cell (Fig. 4c, white box). Even for this example of high background levels compared to the non-cell measurements, its minor dynamics upon heating did not significantly affect the thermophoretic analysis.

The setup geometry is capable of simultaneously measuring vertical thermophoresis in cells at various positions in the field of view of the camera. For the used molecule systems, we did neither expect nor record significant deviations of D_T and D across the image of the cell. It is interesting to note that the reallocation of the molecules by thermophoresis resulted in a much reduced kinetics of the back-diffusion dynamics which could not be fully accounted for by the thermophoretic model for the cell measurements while they were perfectly understood for the measurements without the cells. This points to a yet to be understood cellular dynamics induced by the global application of a temperature field. One should note that the cells are located at the cold side of the chamber.

In Fig. 4d traces with different heating intensities are shown. At a 5-fold higher temperature gradient, larger thermophoretic amplitude is found after the also increased temperature jump. The diffusion coefficient is not affected and traces are well fitted by the thermophoretic model. Thermophoretic mobility raises slightly more than expected from temperature dependent in vitro data [27,31], indicating that intracellular binding inside the cell is reduced by the increased temperature.

Conclusion. In this paper thermophoresis was performed inside living cells for the first time. We have developed a TIRF-based measurement geometry which allows to perform thermophoresis measurements with two-dimensional resolution on the micrometer scale. We compare our results with known epi-fluorescence measurements of the thermophoresis of

DNA and show that the physical processes involved in this geometry can be quantitatively understood. Furthermore, we present data of thermophoresis measurements of fluorescent dyes and DNA inside living cells acquired with the vertical thermophoresis setting. Biomolecular binding studies are already conducted in cell lysate [8]. Comparable to electrophoresis in vitro, thermophoresis has the potential to perform in vivo measurements of various fluorescently labeled biomolecules inside the living cell. Since the shown method allows for parallel imaging with micrometer resolution and is able to resolve thermophoretic mobilities and diffusion coefficients, further developments bode well to allow the quantification of biomolecule affinities inside living cells.

Table I. *Parameters used for the simulations in Fig. 4. At various laser power, different temperature gradients ∇T were applied. The temperature dependence α of the used fluorophore was fitted, but not calibrated due to an unknown pH dependence upon temperature changes inside the cell. The thermophoretic mobility of BCECF and DNA could be determined from the thermophoretic velocity v_T used to fit the fluorescence transients. We implemented bleaching for TIRF and LED illumination in the simulation with a bleaching rate k_{bleach}. TIRF illumination only bleached the fluorophores close to the cover slip with a penetration depth of λ = 200 nm. The chamber height is denoted with h. Grey columns denote fitting parameters, others are measured or derived values.*

Fig. 4	Mole-cule	∇T [K/µm]	$\Delta T\,\alpha$ [%]	h [µm]	v_T [µm/s]	D_T [µm²/sK]	k_{bleach} [%/s]	D [µm²/s]
(a) TIRF	BCECF	0.076	20	8	0.24	3.2	15	3
(a) LED	BCECF	0.076	15	8	0.24	3.2	0.2	3
(c) 1D	BCECF	0.17	45	8	0.60	3.6	35	3
(c) 2D	BCECF	0.17	45	cone	0.66	4.0	15	3
(d) 1D	BCECF	0.034	21	10	0.15	4.4	13	3
(d) 2D, 5xIR	BCECF	0.17	47	cone	1.32	8.0	10	4
(b) 1D	DNA	0.17	22	5	0.02	0.12	0	0.1

Acknowledgements

We thank for the cell culture with Hermann Gaub and Angelika Kardinal. Funding from SFB 1032 Project A4 and the Nanosystems Initiative Munich is gratefully acknowledged.

Autor Contributions

Maren Reichl built the setup conducted the experiments, analyzed the data and wrote the paper. Dieter Braun designed the experiments, analyzes the data and wrote the paper.

References

1 P. Baaske, C.J. Wienken, P. Reineck, S. Duhr, and D. Braun, Angew. Chem. Int. Ed. **49**, 2238 (2010).

2 C.J. Wienken, P. Baaske, U. Rothbauer, D. Braun, and S. Duhr, Nat. Commun. **1**, 100 (2010).

3 S.J. Pollack, K.S. Beyer, C. Lock, I. Müller, D. Sheppard, M. Lipkin, D. Hardick, P. Blurton, P.M. Leonard, P.A. Hubbard, D. Todd, C.M. Richardson, T. Ahrens, M. Baader, D.O. Hafenbradl, K. Hilyard, and R.W. Bürli, J. Comput. Aided. Mol. Des. **25**, 677 (2011).

4 K. Corin, P. Baaske, D.B. Ravel, J. Song, E. Brown, X. Wang, S. Geissler, C.J. Wienken, M. Jerabek-Willemsen, S. Duhr, D. Braun, and S. Zhang, PLoS ONE **6**, e23036 (2011).

5 S.A.I. Seidel, C.J. Wienken, S. Geissler, M. Jerabek-Willemsen, S. Duhr, A. Reiter, D. Trauner, D. Braun, and P. Baaske, Angew. Chem. Int. Ed. **51**, 10656 (2012).

6 M. Jerabek-Willemsen, T. André, R. Wanner, H.M. Roth, S. Duhr, P. Baaske, and D. Breitsprecher, Journal of Molecular Structure (2014).

7 S. Lippok, S.A.I. Seidel, S. Duhr, K. Uhland, H.-P. Holthoff, D. Jenne, and D. Braun, Anal. Chem. **84**, 3523 (2012).

8 S.A.I. Seidel, P.M. Dijkman, W.A. Lea, G. van den Bogaart, M. Jerabek-Willemsen, A. Lazic, J.S. Joseph, P. Srinivasan, P. Baaske, A. Simeonov, I. Katritch, F.A. Melo, J.E. Ladbury, G. Schreiber, A. Watts, D. Braun, and S. Duhr, Methods **59**, 301 (2013).

9 x. Shang, F. Marchioni, C.R. Evelyn, N. Sipes, X. Zhou, W. Seibel, M. Wortman, and Y. Zheng, PNAS **110**, 3155 (2013).

10 C.G. Alexander, M.C. Jurgens, D.A. Shepherd, S.M.V. Freund, A.E. Ashcroft, and N. Ferguson, PNAS **110**, E2782 (2013).

11 M. Gertz, F. Fischer, G.T.T. Nguyen, M. Lakshminarasimhan, M. Schutkowski, M. Weyand, and C. Steegborn, PNAS **110**, E2772 (2013).

12 T. Cherrier, V. Le Douce, S. Eilebrecht, R. Riclet, C. Marban, F. Dequiedt, Y. Goumon, J.-C. Paillart, M. Mericskay, A. Parlakian, P. Bausero, W. Abbas, G. Herbein, S.K. Kurdistani, X. Grana, B. van Driessche, C. Schwartz, E. Candolfi, A.G. Benecke, C. van Lint, and O. Rohr, PNAS **110**, 12655 (2013).

13 S. Bhogaraju, L. Cajanek, C. Fort, T. Blisnick, K. Weber, M. Taschner, N. Mizuno, S. Lamla, P. Bastin, E.A. Nigg, and E. Lorentzen, Science **341**, 1009 (2013).

14 X. Xiong, P.J. Coombs, S.R. Martin, J. Liu, H. Xiao, J.W. McCauley, K. Locher, P.A. Walker, P.J. Collins, Y. Kawaoka, J.J. Skehel, and S.J. Gamblin, Nature **497**, 392 (2013).

15 P.N. Snowdon and J.C.R. Turner, Trans. Faraday Soc. **56**, 1409 (1960).

16 J. Chan, J.J. Popov, S. Kolisnek-Kehl, and D.G. Leaist, Journal of Solution Chemistry **32**, 197 (2003).

17 S.A. Putnam, D.G. Cahill, and G.C.L. Wong, Langmuir **23**, 9221 (2007).

18 R. Piazza and A. Guarino, Phys Rev Lett **88**, 208302 (2002).

19 M. Braibanti, D. Vigolo, and R. Piazza, Phys. Rev. Lett. **100** (2008).

20 D. Vigolo, S. Buzzaccaro, and R. Piazza, Langmuir **26**, 7792 (2010).

21 S. Iacopini, R. Rusconi, and R. Piazza, Eur. Phys. J. E **19**, 59 (2006).

22 W. Köhler, J. Chem. Phys. **98**, 660 (1993).

23 Y. Kishikawa, H. Shinohara, K. Maeda, Y. Nakamura, S. Wiegand, and R. Kita, Phys. Chem. Chem. Phys. **14**, 10147 (2012).

24 H. Jung, V.E. Gusev, H. Baek, Y. Wang, and G.J. Diebold, Physics Letters A **375**, 1917 (2011).

25 F.M. Weinert and D. Braun, Physical Review Letters **101**, 168301 (2008)

26 A. Pluen, P.A. Netti, R.K. Jain, and D.A. Berk, Biophysical Journal **77**, 542 (1999).

27 S. Duhr, and D. Braun, PNAS **103**, 19678 (2006).

28 H.P. Kao, J.R. Abney, and A.S. Verkman, The Journal of Cell Biology **120**, 175 (1993).

29 E. Dauty and A.S. Verkman, Journal of Biological Chemistry **280**, 7823 (2005).

30 G.L. Lukacs, P. Haggie, O. Seksek, D. Lerchardeur, N. Freedman, and A.S. Verkman, Journal of Biological Chemistry **275**, 1625 (2000).

31 M. Reichl, M. Herzog, A. Götz, and D. Braun, Phys. Rev. Lett. **112**, 198101 (2014).

Supplemental Material

Materials and Methods.

Setup. The experiments were conducted at the following setup: An upright fluorescence microscope (Zeiss Axiotech) was equipped with an IR laser (Fibotec, $\lambda = 1480$ nm, max. 300 mW) for heating, and a 488 nm laser (single mode coupled laser, < 50 mW, Visitron Systems GmbH) TIRF illumination (Fig. 1a). The TIRF laser was focused on the side of the back focal plane of the objective (Nikon, Apo Tirf 100x 1.49 NA oil) and coupled into the light path right above the objective with a dichroic beam splitter (dual line z491/561 or dual line notch 555/646, AHF Analysentechnik). The excitation filter had enough bandwidth (480/80 and 620/60) to allow the LED illumination light to pass the narrow dichroic beam splitter, with which the TIRF excitation was coupled into the light path. As a result, epi-illumination with the LED and TIRF illumination were both possible within the same setup.

Chamber. Listed from bottom to top, the sample chamber consisted of a 2 mm thick glass slide coated on the top side with 300 nm chromium and protective 60 nm silicon oxide to prevent a toxic influence on the cells. The aqueous solution was placed on top of the coated glass slide, supplemented with a paraffin oil ring to prevent evaporation. The top of the sandwich structure was formed by 130 µm thick borosilicate glass cover slip held in place with 12.5 µm thick mylar foil spacers. For cell measurements, the cover slip had cells adhering to it upside down. A spot at the lower interface to the sample was heated by absorbing IR light in the chromium layer. The spot size could be varied with the IR focus. The top cover slip, connected to the immersion oil, acts as heat sink. A camera (PCO sensicam uv) recorded the fluorescence images over time. The images were corrected by subtracting the dark noise of the camera and then normalized by the initial fluorescence in absence of IR heating, to correct for inhomogeneous fluorescence and illumination.

Optics. For DNA measurements in Figure 3, the IR laser was focused onto the chromium layer (HWHM = 65 µm). Here, both lateral and vertical thermophoresis could be imaged and compared (Fig. 1b). In the bead and cell measurements (Figure 2 and 4) the IR laser was defocused (HWHM ≈ 300 µm) to minimize lateral thermophoresis. Then the temperature gradient was mostly vertical and hardly varied over the field of view (Fig. 1c). The chamber height without cells was about 20 µm to suppress convection, and was measured optically by focusing the microscope to its boundaries and comparing to a similarly high reference step calibrated with an atomic force microscope. For TIRF illumination we focused on the upper cover slip-glass interface, for LED illumination (except in the bead measurements) to the middle of the chamber. A LabVIEW program automated the measurement. The camera recorded the fluorescence before, during and after IR

Understanding the similarity in thermophoresis between single and double stranded DNA or RNA

Maren Reichl[1], Mario Herzog[1], Ferdinand Greiss[1], and Dieter Braun[1,*]

[1] Systems Biophysics, Physics Department, Nanosystems Initiative Munich and Center for NanoScience, Ludwig-Maximilians-Universität München, Amalienstraße 54, 80799 München, Germany

* To whom correspondence should be addressed.
Tel: +49 89 2180 2317; Fax: +49 89 2180 16558; Email: dieter.braun@lmu.de

Abstract. Thermophoresis is the movement of molecules in a temperature gradient. We found that single and double stranded oligomers behave surprisingly similar although one would naively expect that the doubled charge should a show four times stronger thermophoresis according to the recently proposed capacitor model to describe thermophoresis. However, we find very similar thermophoretic depletion in all conditions. We extend the spherical capacitor model to rod shaped double stranded DNA and RNA. As shown by the analysis, the major reason is not the difference in geometry, but a similar value for the charge per base and charge per base pair, a behavior also inferred from electrophoresis data. Interestingly, we find above similarity in thermophoresis also under the addition of crowding agents such as polyethylene glycol, in contradiction to previously published data. Overall the analysis documents the continuous progress in the microscopic understanding of biomolecule thermophoresis.

INTRODUCTION

The molecular origin of thermophoresis of charged particles such as short DNA or RNA was recently elaborated for various sizes and Debye lengths (1). The main contribution is explained with a spherical capacitor model. Interestingly, double and single stranded oligomers show very similar thermophoresis although the persistence length of double stranded DNA (dsDNA) and RNA (dsRNA) is much longer than the sequences used, and the spherical shape of a random coil cannot be fully assumed. Here, we will explain in more detail, why such a spherical capacitor nevertheless can be used as a good approximation. Previously, the effect of molecule geometry in thermophoresis was studied for solid virus particles, with a contour length of 880 nm, a radius of 3.4 nm and a persistence length of 2.2 µm (2) assuming a constant surface charge density and using modified Bessel functions to describe the geometry. Such an approach is not matching the geometry of short double stranded DNA or RNA since these viruses are always larger than the Debye length and end effects are assumed to be negligible. Alternatively it was proposed to approximate the shape as a string of spheres (2). Here, we follow a direct analytical method with a full geometrical description, valid for all Debye lengths. We insert a cylindrical condensator into the previously studied spherical capacitor (1,3). All shielding capacitors are assuming that the condensators are in acting in parallel. A cylinder

capped with hemispheroids was also used in modelling of electrophoresis (4). There it was found that for a length-to-diameter ratio greater than about 3, the end caps of the cylinder have a negligible effect, provided the length is chosen to yield a structure with the same volume. The subsequent study will show in detail that the geometry of DNA does not significantly affect the thermophoresis under near physiological salt concentrations and a length below 50 bases.

In the second part of this study, we will discuss an additive contribution to the Soret coefficient, i.e. the strength of thermophoresis, originating in the depletion force. Maeda et al. (5) reported a fundamental difference between single stranded DNA (ssDNA) and dsDNA, claiming that crowding selects for double stranded DNA motives. We repeated their experiments, but now with identical fluorescence labels covalently attached to the DNA and not using intercalating dyes for the double stranded measurements. We could not confirm their results. Even under crowding, ssDNA and dsDNA behave very similar.

MATERIAL AND METHODS

The setup consisted of a modified fluorescent microscope with infra-red heating as described previously (1). The following sequences were used in the experiments, where the first strand was labelled at the 5’ end with the fluorescent dye Hex (6-carboxy-2',4,4',5',7,7'-hexachlorofluorescein) (labelled oligomers from Biomers, Germany). The sequences were designed to have minimal secondary structure also in the single stranded version to form a random coil.

DNA

22mer: 5'–Hex–ATT GAG ATA CAC ATT AGA ACT A–3'

50mer: 5'–Hex–ATA ATC TGT AGT ACT GCA GAA AAC TTG TGG GTT ACT GTT TAC TAT GGG GT–3'

RNA

22mer: 5'–Hex–AUU GAG AUA CAC AUU AGA ACU A–3'

50mer: 5'–Hex–AUA AUC UGU AGU ACU GCA GAA AAC UUG UGG GUU ACU GUU UAC UAU GGG GU–3'

Double stranded probes contained an equal amount of complementary sequence. DNA and RNA were used in a final concentration of 1 µM. The buffer for the first experiments in Fig. 3 contained 1 mM TRIS (2-amino-2-hydroxymethyl-propane-1,3-diol) with pH 7.8 at 25 °C and the Debye length was titrated with KCl. For the later experiments in Fig. 4 we used PEG Poly(ethylene glycol) 10000 (Fluka, Sigma Aldrich) as crowding agent. The buffer for the 22mer contained 10 mM TRIS pH 7.5 and for the 50mer it contained 1 mM TRIS pH 7.8. Here, the Debye length was titrated using NaCl. In all experiments, the monovalent TRIS buffer was accounted for when calculating the Debye length.

RESULTS AND DISCUSSION

Non-spherical Geometry

In previous studies short DNA was used as a model system to experimentally test the capacitor model of thermophoresis (1). Although the persistence length of single stranded DNA is 10 Å to 32 Å, i.e. 2 to 7 bases short (6), and a spherical form of the molecule is likely, the shape of double stranded oligomers might be better modelled as a rod, since their persistence length is about 170 base pairs (7). Wang et. al. (2) calculated the Soret coefficient for a long cylinder with neglected end effects and for a known surface charge density and they found that the rod could be approximated as a string of spheres. Here, we will adapt the spherical capacitor model, which was first proposed by Dhont (3), to elongated rods. The shape is modelled as a sphere, which is cut in halves, with an inserted cylinder of the same radius (see Fig. 1). Thus, also the end effects can be included in the model. For comparison we will calculate all three models: the sphere, the cylinder without end caps, and the combined structure, which we call rod.

Theory. The rod capacitor (capacitance C_{rod}) is composed of two capacitors in parallel: a spherical capacitor (C_{sphere}) and a cylindrical capacitor ($C_{cylinder}$ with the length L reduced by $2R$, i.e. the length of the end caps),

$$\begin{aligned} C_{sphere} &= 4\pi\varepsilon R\left(R/\lambda_{DH}+1\right) \\ C_{cylinder} &= \frac{2\pi\varepsilon L}{\ln\left(\lambda_{DH}/R+1\right)} \\ C_{rod} &= C_{sphere}+C_{cylinder} \end{aligned} \tag{1}$$

with ε being the dielectric constant of water, $\lambda_{DH}=\sqrt{\frac{\varepsilon kT}{N_A e^2\sum_i c_i z_i^2}}$ the Debye-Hückel screening length, or Debye length in short, k the Boltzmann constant, T the absolute temperature, N_A the Avogadro constant, e the elementary charge, c_i the concentration of the ion species i and z_i the charge number of the ion species i, R the radius of the sphere and of the cylinder, and L the overall length, see Fig. 1. The energy stored in a capacitor is $W=Q^2/(2C)$, with $Q=Z_{eff}\,e$ being the effective charge of the particle, and Z_{eff} the effective charge number in multiples of the elementary charge e.

$$\begin{aligned} W_{sphere} &= \frac{Q^2}{8\pi\varepsilon R\left(R/\lambda_{DH}+1\right)} \\ W_{cylinder} &= \frac{Q^2\ln\left(\lambda_{DH}/R+1\right)}{4\pi\varepsilon L} \\ W_{rod} &= \frac{Q^2}{4\pi\varepsilon\left[2\mathrm{R}\left(R/\lambda_{DH}+1\right)+\left(L-2\mathrm{R}\right)/\ln\left(\lambda_{DH}/R+1\right)\right]} \end{aligned} \tag{2}$$

Thus, the Soret coefficient of the sphere $S_{T\,sphere}$, the cylinder $S_{T\,cylinder}$, and the rod $S_{T\,rod}$ can be calculated as a temperature derivative of the electric energy as demonstrated in literature (3,1):

$$S_T = \frac{1}{kT}\frac{\partial W}{\partial T}$$

$$S_{Tsphere} = \frac{Q^2}{kT^2 16\pi\varepsilon\lambda_{DH}\left(R/\lambda_{DH}+1\right)^2}\left[1-\frac{\partial \ln\varepsilon}{\partial \ln T}\left(1+\frac{2\lambda_{DH}}{R}\right)\right]$$

$$S_{Tcylinder} = \frac{Q^2}{kT^2 4\pi\varepsilon L}\left[\frac{\lambda_{DH}\left(1+\frac{\partial \ln\varepsilon}{\partial \ln T}\right)}{2\mathrm{R}\left(\lambda_{DH}/R+1\right)}-\frac{\partial \ln\varepsilon}{\partial \ln T}\ln\left(\lambda_{DH}/R+1\right)\right]$$

$$S_{Trod} = \frac{Q^2}{kT^2 4\pi\varepsilon\left[2\mathrm{R}\left(R/\lambda_{DH}+1\right)+\left(L-2\mathrm{R}\right)/\ln\left(\lambda_{DH}/R+1\right)\right]^2}\left\{\frac{R^2}{\lambda_{DH}}+\frac{\left(L-2\mathrm{R}\right)\lambda_{DH}/R}{2\left(\lambda_{DH}/R+1\right)\ln^2\left(\lambda_{DH}/R+1\right)}\right.$$

$$\left.+\frac{\partial \ln\varepsilon}{\partial \ln T}\left[\frac{\left(L-2\mathrm{R}\right)\lambda_{DH}/R}{2\left(\lambda_{DH}/R+1\right)\ln^2\left(\lambda_{DH}/R+1\right)}-\frac{R^2}{\lambda_{DH}}-2\mathrm{R}-\frac{L-2\mathrm{R}}{\ln\left(\lambda_{DH}/R+1\right)}\right]\right\}$$

(3)

In case the length of the rod is exactly the diameter of the sphere ($L = 2R$), i.e. no cylinder is inserted, the equation for the rod does yield the spherical equation. The three equations are calculated in Fig. 2a resembling a 22mer. Single stranded DNA with no secondary structure is a random coil roughly in the shape of a sphere since the persistence length is about 2 to 7 bases (6). The hydrodynamic radius of the sphere depends on the DNA length, i.e. 2 nm and 3.7 nm for a 22mer and a 50mer, respectively. However, the radius of the rod or the cylinder is that of the DNA strand: 1 nm and the length of double stranded DNA is $L = base\ \ pairs \cdot 0.34\ \mathrm{nm}/\mathrm{base\ pair}$, i.e. 7.5 nm and 17 nm for the 22mer and the 50mer, respectively.

Low salt limit. For the limit of high Debye lengths or low salt concentrations, the change in geometry from a spherical to a rod structure should not affect the Soret coefficient. In the case of an infinite Debye length, a particle can be considered a point charge, regardless of its shape. Formally, $S_{T\,cylinder}$ goes to infinity for low salt concentrations, but for the rod the end effects become much more important, since the surface of the outer sphere (i.e. of the end caps) grows as $\lambda_{DH}{}^2$, whereas the surface of the outer cylinder only grows with λ_{DH}.

$$\lim_{\lambda_{DH}\to\infty} S_{Trod} = \lim_{\lambda_{DH}\to\infty} S_{Tsphere} = \frac{-Q^2\frac{\partial \ln\varepsilon}{\partial \ln T}}{kT^2 8\pi\varepsilon R} \qquad (4)$$

So the Soret coefficient becomes constant for very large λ_{DH}. For the rod the final value equal to a sphere with the same radius, is approached only for Debye lengths far too long to be achievable for real electrolytes. Thus, the Soret coefficient of an elongated particle is considerably lower than the

Soret coefficient of a sphere with same diameter and charge, and it is about as large as the Soret coefficient of a particle with the same surface.

High salt limit. For the limit of high salt concentrations, i.e. small Debye lengths, the capacitance changes with surface area similar to a plate capacitor, since the area of the two plates hardly differs. The Soret coefficient of a plate capacitor is linear in Debye length. Here, the spherical part and the cylindrical parts are separated, because the shielding of both parts does not overlap for such small screening lengths. The area for a spherical and a rod like molecule of the same radius will differ, and thus the slope of the Soret coefficient will differ. However, the capacitor part of the Soret coefficient will in both cases vanish for the limit of very high salt concentrations. The surface of the two capping half spheres at the end of the rod (together $4R^2\pi$) is exactly as large as the surface of the additional cylinder, if the cylinder was extended all the way to the end ($2\pi RL$ with $L=2R$). Thus, for the limit of high salt concentration the Soret coefficient of the rod is equal to the Soret coefficient of a cylinder with neglected end effects.

$$\begin{aligned}
\lim_{\lambda_{DH}\to 0} S_{T\,sphere} &= \frac{Q^2}{kT^2 16\pi\varepsilon R^2}\left(1-\frac{\partial \ln \varepsilon}{\partial \ln T}\right)\lambda_{DH} \\
\lim_{\lambda_{DH}\to 0} S_{T\,cylinder} &= \frac{Q^2}{kT^2 8\pi\varepsilon LR}\left(1-\frac{\partial \ln \varepsilon}{\partial \ln T}\right)\lambda_{DH} = \frac{2R}{L}\lim_{\lambda_{DH}/R\to 0} S_{T\,sphere} \\
\lim_{\lambda_{DH}/R\to 0} S_{T\,rod} &= \frac{Q^2}{kT^2 8\pi\varepsilon LR}\left(1-\frac{\partial \ln \varepsilon}{\partial \ln T}\right)\lambda_{DH} = \lim_{\lambda_{DH}/R\to 0} S_{T\,cylinder}
\end{aligned} \tag{5}$$

This agrees with the approximations by Wang et al. (2). They calculated and compared the Soret coefficient of a particle with constant surface charge. In contrast, we calculate and compare the Soret coefficient for a particle with constant charge, since in our experiments we know the effective charge of the molecule, given by a constant charge per length (1,3). And this charge is approximately the same for single and double stranded DNA (1,8). If a constant surface charge is maintained, then the charge *Q* scales with the aspect ratio *L*/(2*R*). Since the Soret coefficient is proportional to the square of the charge *Q*, our equation matches the one of Wang (2) for the limit of high salt concentrations.

The sphere in Fig. 2b again models a 22mer ssDNA. Additionally rods of different aspect ratios but with the same surface areas are shown. The aspect ratios for the 22mer and the 50mer are 3.75 and 8.5, respectively. Only for dsDNA longer than about 50 bases, i.e. an aspect ratio *L /(2R)* = 9 we start to see deviations from the spherical curve. For comparison, the persistence length of dsDNA is at about 170 bases (7). Considering this, the theoretical Soret coefficients are similar for single and double stranded oligomers in the range of experimentally accessible Debye lengths. The effects of the elongated shape and the smaller radius approximately cancel each other.

Experiments. Since the theoretical curves are alike, measurements of double stranded DNA can be fitted equally well with a spherical and a rod like model (Fig. 3). As free fitting parameters we choose the effective charge number and a molecule specific offset, which includes other contributions to the

Soret effect such as the ideal gas contribution 1/T, the non-ionic contribution or the Seebeck effect, which were all discussed previously (1). Also, the depletion contribution is included, which will be discussed in the second part of this paper. Both the spherical and the rod model yield very similar effective charge numbers as fitting parameter. Since the charge of a particle enters equation 3 quadratically, one could expect a factor 4 difference between single stranded and double stranded DNA and RNA. However, their Soret coefficients are quite similar (see Fig. 3) with a similar effective charge. According to the Manning theory (8) and electrophoresis measurements (9) single stranded and double stranded oligomers have approximately the same effective charge and electric mobility. As we discuss and see here, this similarity translates also to thermophoresis.

Crowding agent Polyethylenglycol

Theory. Here we shortly recapitulate the theoretical influence of a crowding agent on thermophoresis through depletion forces. As will be seen, also theoretically there is no difference between single and double stranded DNA, when their radii is alike. If the sample concentration is on the order of weight percent, or if a crowding agent e.g. PEG (Polyethylenglycol) is present in the solution, an additional excluded volume effect can be noticed in thermophoresis measurements and should be added. It can be calculated according to (10,11,5). The change in Soret coefficient for the molecule of interest, here DNA, is then:

$$\Delta S_T = -2\pi\left(S_T^{PEG} - 1/T\right) R_{DNA} R_{PEG}^2 c_{PEG} \tag{6}$$

with S_T^{PEG} the infinite dilution Soret coefficient of the crowding agent, e.g. PEG, and R_{PEG} its hydrodynamic radius, R_{DNA} the hydrodynamic radius of the particle of interest, e.g. DNA, and c_{PEG} the concentration of the crowding agent.

The Soret coefficient of the molecule of interest, which has a low concentration, depends on the Soret coefficient of the crowding agent which is added as well as on its concentration: If the Soret coefficient of the crowding agent has the same sign as the one of the probed molecule, the crowding agent will accumulate on the cold side and displace the molecule of interest. As an example, Jiang et al. measured the Soret coefficient of beads in a solution of the crowding agent PEG without salt (10).

Experiments. We conducted salt-dependent experiments of 22mer ssDNA and dsDNA and 50mer ssDNA in 3 %wt. and 6 %wt. We used PEG at a molecular weight of 10 000 Da, very similar to Maeda (5). Since pure PEG is a solid with a density of 1.2 g/cm³, we convert the reported 5 %vol. in solution to 6 %wt in our experiments.

They argue not to observe accumulation for single stranded molecules. We cannot confirm this and find accumulation for both single and double stranded DNA in PEG. In Fig. 4a both ssDNA and dsDNA of 22mer length show accumulation at 25 °C, in 3 % and 6 % wt. PEG. Accumulation is found when the Soret coefficient becomes negative, i.e. the molecules wander towards the hot side. As

expected from equation 6, we find a higher accumulation, i.e. lower Soret coefficients, for higher PEG concentrations.

The reduction in the Soret coefficient caused by PEG is stronger for larger molecules, since the DNA radius enters equation 6 (Fig. 4a and b). The difference is even larger, if we consider that without PEG the larger 50mer DNA has a higher Soret coefficient than the smaller 22mer (Fig. 3). As in Ref. (5), we do find higher accumulation for the 50mer than for the 22mer.

In contrast to their study we find an increase in the Soret coefficient toward small salt concentration (Fig. 4a,b). This most likely is a result of the capacitor model discussed earlier. For high salt concentrations we see an increase in the Soret coefficient, similar to Maeda et al. (5), which cannot easily be explained and could be the result of DNA-PEG interactions, or artifacts from sticking to the capillary walls. We marked these data points with a circle in Fig. 4 and only fit the spherical capacitor model to the data with longer Debye lengths (for fit parameters see table I). If we assume that the hydrodynamic radius does not depend significantly on the PEG and salt concentration, the fit yields about half of the effective charge which is found in aqueous solutions. This could mean that residual charge could enter the solution with PEG and thus lead in reality to a reduced Debye length. Alternatively, if we assume the DNA charge to be independent of PEG, a larger radius of the DNA would have to be assumed, in contradiction with the crowding effect. Probably the influence responsible for the strong increase of the Soret coefficient towards very small Debye lengths continues on to longer Debye lengths, but is weaker there. Thus the shape of this influence is contrary to the shape of the capacitor model and apparently decreases the amplitude from the capacitor model. In the capacitor model, a larger charge increases the amplitude with a higher plateau.

One should not discriminate too strictly between positive and negative Soret coefficients, as the sign is merely a result of which of the components of the Soret coefficient are stronger in the actual conditions. For example, the base temperature of the experiment is varied in Fig. 4c without varying the infra-red laser power and the temperature increase. This will cause a change in the sign, here shown for 50mer ssDNA in PEG, but a similar dependence was measured before in water (1). We fitted the empiric equation based on Ref (12)

$$S_T = S_T^{\infty}\left[1 - \exp\frac{T^* - T}{T_0}\right] \tag{7}$$

to the data which was shown to fit DNA for diluted solutions without a crowding agent. It yielded S_T^{∞} = 0.052 ± 0.013 and 0.024 ± 0.017; T^* = 32.4 ± 2.7 and 73.8 ± 6; T_0 = 35.4 ± 9.8 and 46.0 ± 15.2 for the 3% and 6% PEG solutions, respectively.

CONCLUSION

We have shown that single and double stranded DNA of the same length behave surprisingly similar in a temperature gradient. We derived an analytical capacitor model for elongated rods which with arbitrary Debye lengths. The cylindrical capacitor without end caps diverges for large Debye lengths, but the spherical and the rod shaped capacitor behave alike for all possible Debye lengths – theoretically as well as in the experiments. We reassessed the thermophoresis in the crowding agent PEG for single and double stranded DNA (5), but now with covalent markers and cannot confirm a sign change between single and double stranded DNA. Even for 3% and 6% PEG, we can fit the salt dependence of DNA thermophoresis with the capacitor model. With PEG, both single and double stranded DNA accumulate and deplete to comparable extends.

FUNDING

This work was supported by the Nanosystems Initiative Munich, the LMU Initiative for Functional Nanosystems, the SFB 1032 Nanoagents project A4 and the ERC Starting Grant AUTOEVO.

REFERENCES

1. Reichl, M.R., Herzog, M., Götz, A. and Braun, D. (2014) Why charged molecules move across a temperature gradient: the role of electric fields, *Physical Review Letters,* **112**, 198101.
2. Wang, Z., Kriegs, H., Buitenhuis, J., Dhont, J.K.G. and Wiegand, S. (2013) Thermophoresis of charged colloidal rods, *Soft Matter,* **9,** 8697.
3. Dhont, J.K.G., Wiegand, S., Duhr, S. and Braun, D. (2007) Thermodiffusion of charged colloids: single-particle diffusion, *Langmuir : the ACS journal of surfaces and colloids,* **23,** 1674–1683.
4. Allison, S.A. and Mazur, S. (1998) Modeling the free solution electrophoretic mobility of short DNA fragments, *Biopolymers,* **46,** 359–373.
5. Maeda, Y.T., Tlusty, T. and Libchaber, A. (2012) Effects of long DNA folding and small RNA stem-loop in thermophoresis, *Proceedings of the National Academy of Sciences of the United States of America,* **109,** 17972–17977.
6. Sim, A.Y.L., Lipfert, J., Herschlag, D. and Doniach, S. (2012) Salt dependence of the radius of gyration and flexibility of single-stranded DNA in solution probed by small-angle x-ray scattering, *Physical Review E,* **86,** 021901.
7. Stellwagen, E. and Stellwagen, N.C. (2002) Determining the electrophoretic mobility and translational diffusion coefficients of DNA molecules in free solution, *Electrophoresis,* **23,** 2794–2803.
8. Hickey, O.A., Shendruk, T.N., Harden, J.L. and Slater, G.W. (2012) Simulations of free-solution electrophoresis of polyelectrolytes with a finite Debye length using the Debye-Hückel approximation, *Physical Review Letters,* **109**.
9. Stellwagen, E., Lu and Stellwagen, N.C. (2003) Unified description of electrophoresis and diffusion for DNA and other polyions, *Biochemistry,* **42,** 11745–11750.
10. Jiang, H.-R., Wada, H., Yoshinaga, N. and Sano, M. (2009) Manipulation of colloids by a nonequilibrium depletion force in a temperature gradient, *Physical Review Letters,* **102,** 208301.
11. Würger, A. (2010) Thermal non-equilibrium transport in colloids, *Reports on Progress in Physics,* **73,** 126601.
12. Iacopini, S., Rusconi, R. and Piazza, R. (2006) The macromolecular tourist: Universal temperature dependence of thermal diffusion in aqueous colloidal suspensions, *The European Physical Journal E,* **19,** 59–67.

TABLE AND FIGURES LEGENDS

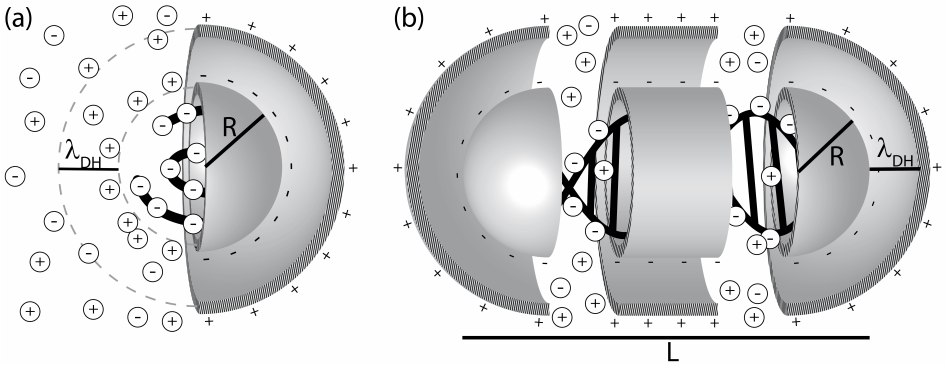

Figure 1. Molecular models to explain the Debye length dependence of thermophoresis. (a) A charged molecule, here DNA, is screened by the counter ions in solution. This can be modelled as a spherical capacitor with the molecule as the inner shell with radius *R* and the counter ions as the outer sphere. The charge of the molecule is screened within the Debye length λ_{DH}, thus two spheres are separated by the Debye screening length. (b) The spherical capacitor model can be extended to rod shaped molecules such as short double stranded DNA. The shape is modelled as a sphere, which is cut in halves with an inserted cylinder. The radius of the sphere and the cylinder is *R*, the overall length is *L*. The capacitor is also treated as a spherical and a cylindrical capacitor in parallel.

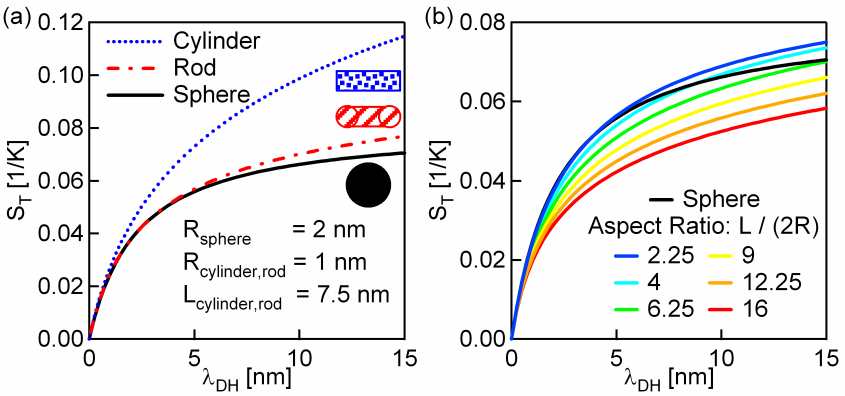

Figure 2. Calculation of the cylinder rod and sphere models for a 22mer DNA. (a) The single strand is modelled as a sphere with radius R = 2 nm and the double strand as a cylinder and a rod with R = 1 nm and length L = 7.5 nm. Between rod and sphere not much difference is found. (b) In comparison to the sphere of (a), we plot rods with different aspect ratios $L/(2R)$ but with the same surface area as the sphere. For experimentally accessible Debye lengths, the rods behave similar to the sphere up to about an aspect ratio of 9. A 22mer and a 50mer dsDNA have aspect ratios of 3.75 and 8.5, respectively. The Soret coefficients were calculated at temperature T = 25 °C with an effective charge of Q = -10 *e*.

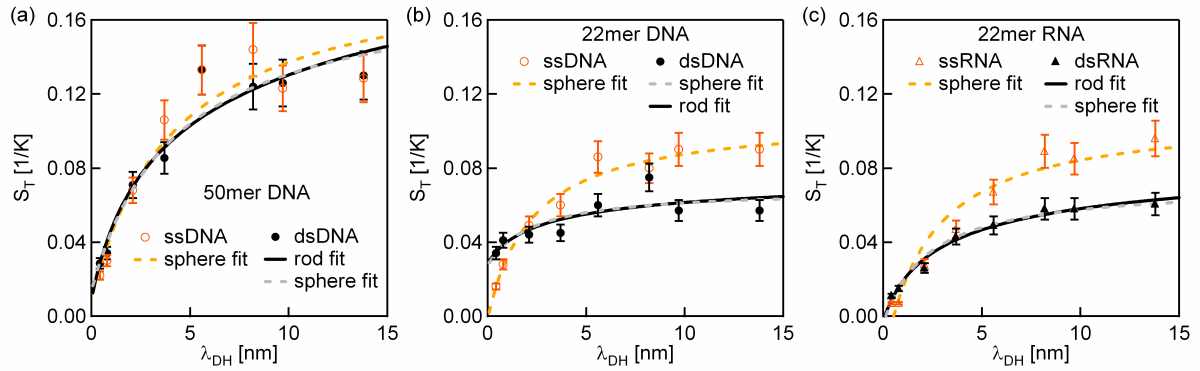

Figure 3. The thermophoresis of double stranded DNA and RNA can be fitted as a rod with radius R = 1 nm and a length of L = 7.5 nm and 17 nm for 22mer and 50mer, respectively. Single stranded oligonucleotides can be viewed as spheres with a hydrodynamic radius of 2 nm and 3.7 nm for the 22mer and the 50mer, respectively. However, the respectively other model geometry can be similarly fitted to the thermophoresis measurements. The sphere and the rod fit and yield very similar effective charges Z_{eff} for the double stranded measurement data (see Table I) The Debye length was titrated using KCl including the 1 mM TRIS buffer at pH 7.8. The measurements were conducted at 25 °C.

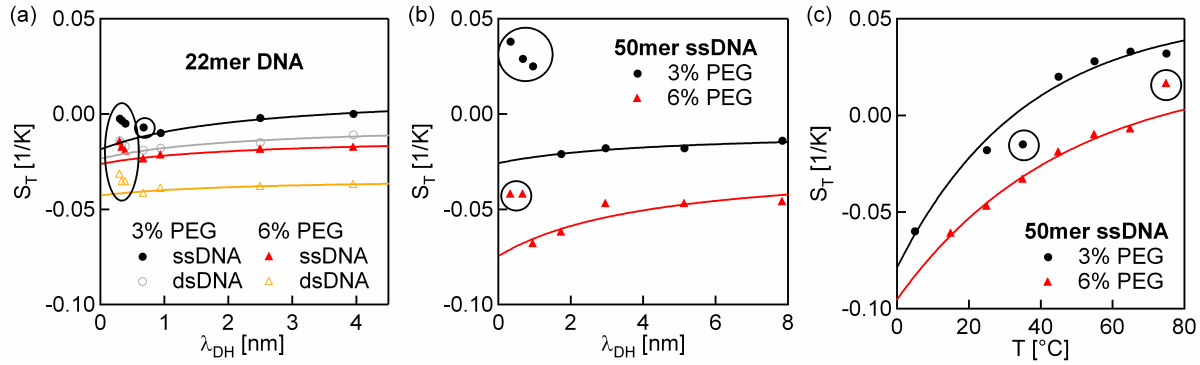

Figure 4. Thermophoresis measurement of ssDNA and dsDNA in aqueous NaCl solutions with PEG as a crowding agent. (a, b) Increased PEG concentration leads to more negative Soret coefficients. Circled data points were excluded from the fits. At low Debye length we suspect sticking interactions to the measurement chamber or to PEG. In contrast to the study of Maeda (5) we find negative Soret coefficients, i.e. accumulation also for ssDNA. Notably, we used covalently bound dyes for both dsDNA and ssDNA measurements, not intercalating dyes for the dsDNA measurements as in (5). The spherical capacitor model was fitted to the data with large Debye lengths. (c) The sign change is no fundamental difference between ssDNA and dsDNA, but merely the result of different contributions to the Soret coefficient as is shown by measurements under varied base temperature. The empiric temperature dependence of Ref (13) was fitted to the data. The 50mer was measured in 1 mM TRIS buffer pH 7.8, the 22mer in 10 mM TRIS pH 7.5. TRIS was accounted for when titrating with NaCl. Measurements were conducted at 25 °C (a, b) and 10 mM NaCl (c).

Table I. Parameters for the fits in Fig. 3 and Fig. 4. We fitted Z_{eff} and assumed the radius to be R = 2.0 nm and R = 3.7 nm based on PEG-free measurements of the diffusion coefficient. Temperature was 25 °C, relative permittivity of water ε_r = 78 and its temperature derivative $\partial \ln \varepsilon / \partial \ln T = -1.35$.

Fig. 3 without PEG	Z_{eff}
50mer ssDNA sphere	20.3 ± 1.3
50mer dsDNA sphere	19.5 ± 1.0
50mer dsDNA rod	18.6 ± 1.0
22mer ssDNA sphere	11.6 ± 0.4
22mer dsDNA sphere	7.1 ± 1.0
22mer dsDNA rod	6.9 ± 1.0
22mer ssRNA sphere	12.9 ± 0.6
22mer dsRNA sphere	9.7 ± 0.3
22mer dsRNA rod	9.3 ± 0.3

Fig. 4 with PEG	Z_{eff}
50mer ssDNA 3% PEG	6.2 ± 0.9
50mer ssDNA 6% PEG	10.6 ± 1.4
22mer ssDNA 3% PEG	6.1 ± 0.4
22mer ssDNA 6% PEG	4.2 ± 0.3
22mer dsDNA 3% PEG	4.7 ± 0.4
22mer dsDNA 6% PEG	3.4 ± 0.5